INSTITUTO DE PESQUISAS ENERGÉTICAS E NUCLEARES
Autarquia Associada à Universidade de São Paulo

45S5 Bioglass®-based compositions containing alumina and strontium

MARIANA SILVA DE ARAUJO

Tese apresentada como parte dos requisitos para obtenção do Grau de Doutor em Ciências na Área de Tecnologia Nuclear - Materiais

Orientadora:
Profa. Dra. Sonia Regina Homem de Mello Castanho

São Paulo
2021

INSTITUTO DE PESQUISAS ENERGÉTICAS E NUCLEARES
Autarquia Associada à Universidade de São Paulo

45S5 Bioglass®-based compositions containing alumina and strontium

Versão Corrigida
Versão Original disponível no IPEN

MARIANA SILVA DE ARAUJO

Tese apresentada como parte dos requisitos para obtenção do Grau de Doutor em Ciências na Área de Tecnologia Nuclear - Materiais

Orientadora:
Profa. Dra. Sonia Regina Homem de Mello Castanho

São Paulo
2021

Fonte de Financiamento: CNPq (PhD: 142172/2016-2) e CAPES (PDSE: 88881.189953/2018-01).

Como citar:

ARAUJO, M. S. ***45S5 Bioglass®-based compositions containing alumina and strontium***. 2021. 102 p. Tese (Doutorado em Tecnologia Nuclear), Instituto de Pesquisas Energéticas e Nucleares, IPEN-CNEN/SP, São Paulo.

Araujo, Mariana Silva
45S5 Bioglass®-based compositions containing alumina and strontium / Mariana Silva Araujo; orientadora Sonia Regina Homem de Mello-Castanho. -- São Paulo, 2021.
102 p.

Tese (Doutorado) - Programa de Pós-Graduação em Tecnologia Nuclear (Materiais) -- Instituto de Pesquisas Energéticas e Nucleares, São Paulo, 2021.

1. vidro bioativo. 2. óxido de estrôncio. 3. alumina. 4. biocerâmicas. I. Mello-Castanho, Sonia Regina Homem de, orient. II. Título.

ACKNOWLEDGEMENTS

Parafraseando Newton, *“Se vi mais longe, foi por estar sobre ombros de gigantes”.* Meu infindo agradecimento a todos os gigantes, que não foram poucos, os quais contribuíram para que esta tese se tornasse realidade.

À minha família, pelo amor e suporte incondicionais em todas as etapas deste trabalho, assim como por todos os valores que me ensinaram os quais me trouxeram até aqui. Ao meu amor, Vinicius pela cumplicidade e confiança.

Ao Instituto de Pesquisas Energéticas e Nucleares (IPEN) e ao Centro de Ciência e Tecnologia de Materiais (CECTM) pela insfraestrutura concedida em todos estes anos de pós-graduação.

À Profa. Dra. Sonia Homem de Mello Castanho pela dedicação e carinho em todos estes anos, por incentivar e participar do meu crescimento pessoal e acadêmico, e, sobretudo, por ouvir minhas opiniões.

Al Prof. Dr. José F. Bartolomé, por haberme recibido en el Instituto de Ciencia de Materiales de Madrid (ICMM). Gracias por los buenos momentos que pasé apriendiendo tantas cosas, por el tiempo que pasaste enseñándome. Tus esfuerzos se reflejaron mucho en el resultado de esta tesis. Todo mi cariño y gratitud.

Ao Prof. Dr. Antonio Carlos da Silva, por todas as conversas e por encorajar meus devaneios vítreos. Pela importante ajuda na realização deste trabalho e pelo companheirismo.

À todos os meus queridos amigos do IPEN, cada um tendo seu lugar especial nesta trajetória. Em especial ao pessoal da sala 5, Stefany, Gabriel, Danilo e Zé. À panelinha do almoço, à quinta de lei, Jorge, Mari, Paula, Jeffs,Talita. Ao Reinaldo, Rene e Edson por estarem sempre dispostos a ajudar. Ao Ulissses por compartilhar bons momentos.

Ao Eguiberto e à Marilene pelas conversas e constante preocupação com o meu bem estar desde sempre.

Ao Prof. Dr. Rodolfo Politano, pelos ensinamentos e amizade.

A Ludmila, Pedro, Sandra, Sonia, João, Isabel y Maria por hacerme reír y olvidarme del frío infinito de Madrid.

A minha eterna professora Dr. Vanessa, minha primeira orientadora, por sempre estar presente e partilhar seu carinho e atenção.

Ao CNPq pela bolsa de doutorado no Brasil e à CAPES por permitir o período sanduíche na Espanha, tão enriquecedor para esta tese.

Aos meus amigos e todos aqueles que de alguma forma contribuíram para que esta etapa fosse concluída.

“I’ve done my best, and I begin to understand what is meant by ‘the joy of strife’. Next to trying and winning, the best thing is trying and failing.”

Anne with an e

RESUMO

45S5 Bioglass®-based compositions containing alumina and strontium

Os vidros bioativos são um dos materiais pioneiros para aplicações biomédicas e têm sido amplamente utilizados em superfícies ortopédicas e de implantes dentários. No entanto, sua limitada resistência mecânica, baixa tenacidade e resistência ao desgaste, bem como alta tendência à cristalização, têm impedido seu uso como dispositivos de suporte de carga ou que necessitem de tratamento térmico durante sua produção. Visando reduzir suas desvantagens, a presente pesquisa expõe a influência de 2 mol% de Al_2O_3 e 2 mol% de SrO em composições derivadas do Biovidro® 45S5. Quatro composições foram produzidas para elucidar a diferença de como ambos os óxidos, separadamente e sua sinergia quando juntos, afetam a estrutura, o comportamento térmico e mecânico e, ainda, sua bioatividade. As alterações das estruturas de médio alcance foram caracterizadas pela distribuição Q^n obtidas por espectroscopia Raman e avaliação dos ambientes ^{31}P, ^{27}Al, ^{23}Na e ^{29}Si obtidos por ressonância magnética nuclear de estado sólido “Magic Angle” (MAS-NMR). Apesar da distribuição Q^n ser predominantemente Q^2 em todas as amostras, os critérios de composição usados permitiram melhoras condições de processamento e estabilidade térmica.A adição de Al_2O^3 e SrO promoveu maior parâmetro de sinterabilidade (Sc) o que indica melhor comportamento de sinterização, a estabilidade do vidro contra a cristalização dobrou (K_H) em comparação com 45S5 e a janela de processamento foi ampliada de 106 para 171. Análise de infravermelho por transformada de Fourier (FTIR) após em o teste de bioatividade in vitro indica que 480 min de imersão em solução simulada de fluido corporal (SBF) foi suficiente para reconfigurar as características pré-existentes favorecendo o aparecimento das fases fosfato e carbonatos. Imagens obtidas por microscopia eletrônica de varredura (SEM) e análises de raios-X por dispersão de energia (EDX) forneceram informações sobre as camadas formadas ricas em cálcio e fósforo e grupos silanol. As mudanças feitas na *composição não afetaram a reatividade, mas causaram uma diminuição nos máximos de pH. Após incubação durante uma noite, a concentração inibitória mínima (MIC) estava entre 4 e 8 e a concentração bactericida mínima (MBC) foi de 8 ppm para E. coli.. Os resultados sugeriram que os diferentes pH e taxa de degradação podem ser a razão para o diferente comportamento antibacteriano das amostras. Além disso, todas as composições estudadas foram consideradas não citotóxicas pela metodologia de captação de vermelho neutro. Considerando as mudanças no comportamento mecânico, a resistência à flexão aumentou 60% e a tenacidade dobrou. Por outro lado, a resistência ao desgaste obtida contra o aço foi três vezes maior que o 45S5. Pelos motivos expostos, a utilização desta nova composição de vidro bioativo pode ser uma solução promissora para a reconstrução de defeitos ósseos, bem como para o tratamento e erradicação de infecções ósseas.*

Palavras-chave: *Vidros Bioativos, Óxido de estrôncio, Alumina, Biocerâmicas, Estrutura vítrea, Espectroscopia infravermelho por transformada de Fourier, ressonância magnética nuclear de estado sólido, Espectroscopia Raman, Durabilidade, Dissolução, In vitro bioatividade, Hydroxyapatita.*

ABSTRACT

45S5 BIOGLASS®-BASED COMPOSITIONS CONTAINING ALUMINA AND STRONTIUM

Bioactive glasses are one of the pioneering material for biomedical applications and have been widely used for orthopedic and dental implant surfaces. However, their limited mechanical strength, low toughness, and wear resistance, as well as a high tendency to crystallize, have prevented their use as load bearing devices or that need to undergo thermal treatment during its production. In view of reduce its drawbacks the present research exposes the influence of 2 mol% of Al_2O_3 *and 2 mol% SrO in 45S5 Bioglass®-based compositions. Four compositions were produced to elucidate the difference in how both oxides, separately and their synergy when together, affected the structure, thermal, bioactivity and mechanical behavior. Changes of medium-range structures were characterized by* Q^n *distribution of Raman spectroscopy and evaluation of* ^{31}P, ^{27}Al, ^{23}Na *and* ^{29}Si *environment obtained by Magic angle spinning nuclear magnetic resonance (MAS-NMR). Despite* Q^n *distribution was predominantly* Q^2 *in all samples the composition criteria used enabled improved processing and stabilibity characteristics. The addition of* Al_2O_3 *and SrO promoted larger sinterability parameter* (S_c) *which indicates better sintering behavior, the glass stability against crystallization doubled* (K_H) *compared to 45S5 and the processing window enlarged from 106 to 171. Fourier transform infrared (FTIR) analysis after in vitro bioactivity test indicates that 480 min of soaking in simulated body fluid (SBF) solution was sufficient for reconfiguration of the pre-existent features favoring the appearance of phosphate and carbonate phases. Scanning electron microscope (SEM) images and energy-dispersive X-ray (EDX) provided information upon the layers formed rich in calcium and phosphorous and silanol groups. The changes made in composition did not affect the reactivity but caused a decrease in maxima of pH. After overnight incubation, the minimum inhibitory concentration (MIC) was between 4 and 8 and minimum bactericidal* *concentration (MBC) was 8 ppm. The results suggested that both the different pH and rate of degradation may be the reason for the different antibacterial behavior of the samples. Moreover, all the compositions studied were considered non-cytotoxic by the neutral red uptake methodology. Considering changes in mechanical behavior the bending strength increased by 60% and toughness doubled. On the other hand, the wear resistance obtained against steel was found to be three times higher than 45S5. For the aforementioned reasons, the use of these new bioactive glasses might be a promising solution for the reconstruction of bone defects, as well as for the treatment and eradication of bone infections.*

Palavras-chave: *Bioactive glasses, Strontium oxide, Alumina, Bioceramics, Glass structure, Fourier-transform infrared spectroscopy, Solid-state NMR spectroscopy, Raman spectroscopy, Glass durability, Glass dissolution, In vitro bioactivity testing, Hydroxyapatite.*

LIST OF PAPERS

This thesis is based on the following publications and in printing manuscripts:

PAPER I: M.S. Araujo, A.C. Silva, J.F. Bartolomé, S. Mello-Castanho, **Structural and thermal behavior of 45S5 Bioglass ® -based compositions containing alumina and strontium**, *J. Am. Ceram. Soc*. 103 (2020) 3620–3630. doi:10.1111/jace.17061.

PAPER II: M.S. Araujo, J.F. Bartolomé, S. Mello-Castanho, **Tribological and mechanical behaviour of 45S5 Bioglass®-based compositions containing alumina and strontium**, *Ceram. Int.* 46 (2020) 24347–24354. doi:10.1016/j.ceramint.2020.06.216.

PAPER III: M.S. Araujo, A.C. Silva, B. Cabal, J.F. Bartolomé, S. Mello-Castanho, **In vitro bioactivity and antibacterial capacity of 45S5 Bioglass®-based compositions containing alumina and strontium**, *J. Mater. Res. Technol.*, 13 (2021) 154-161.doi.org/10.1016/j.jmrt.2021.04.053.

PAPER IV: M.S. Araujo, A.C. Silva, J.F. Bartolomé, S. Mello-Castanho, **Glass dissolution mechanism in 45S5 derived compositions.**

Submitted in Ceramics International

CONFERENCE PRESENTATIONS

I: ARAUJO, M. S.; SILVA, A. C.; COSTA E SILVA, D. L.; MELLO-CASTANHO, S. R. H.. **Multifunctional bioactive glasses for tissue regeneration: Compositions modified with strontium oxide.** In: *13TH INTERNATIONAL CONFERENCE ON DIFFUSION IN SOLIDS AND LIQUIDS - DSL2017*, 2017, Viena. 13th International Conference on Diffusion in Solids and Liquids - DSL2017, 2017. v. 13. p. 315-315.

II: ARAUJO, M. S.; SILVA, A. C.; COSTA E SILVA, D. L.; MELLO-CASTANHO, S. R. H. . **Strontium oxide effects on modified bioactive glasses**. In: *THE 7TH LATIN AMERICAN CONFERENCE ON METASTABLE AND NANOSTRUCTURED MATERIALS*, 2017, Brotas. NANOMAT2017 Program & Book of Abstracts, 2017. v. 7. p. 1-136.

III: ARAUJO, M. S.; SILVA, A. C.; COSTA E SILVA, D. L.; MELLO-CASTANHO, S. R. H. **Vidros bioativos modificados com óxido de estrôncio**. In: *61° CONGRESSO BRASILEIRO DE CERÂMICA*, 2017, Gramado. 61º Congresso Brasileiro de Cerâmica, 2017. p. 1812-1813.

IV: M.S. ARAUJO, A.C. SILVA, D.L. COSTA E SILVA, S.R.H. MELLO-CASTANHO. **Variations of Qn distribution in bioactive glasses containing strontium oxide and alumina**. In: *7º CONGRESSO INTERNACIONAL DE CERÂMICA & 62º CONGRESSO BRASILEIRO DE CERÂMICA*, 2018, Foz do Iguaçu.

LIST OF TABLES

Chapter 1

Table 1.1. Nominal and measured (in parentheses) composition in mol%...... 24

Table 1.2. Glass properties: Temperatures (°C) of glass transition (T_g), onset of crystallization (T_x) obtained from DSC curves, first shrinkage (T_{FS}), maximum shrinkage (T_{MS1};T_{MS2}) and liquidus (T_l). Parameters of glass stability S_c, ΔT and K_H(°C) and thermal expansion coefficient at 500°C ($\alpha_{500°C}$).............................. 29

Table 1.3. ^{29}Si MAS-NMR parameters of the bioactive glasses: Qn distribution by peak deconvolution and % calculated from the fractional areas....................... 33

Chapter 2

none

Chapter 3

none

Chapter 4

Table 4.1. Mechanical properties of samples BioH, BioAl, BioSr and BioAlSr.. 84

Table 4.2. Statistical results for the measured indentation toughness of samples BioH, BioAl, BioSr and BioAlSr for indentation load of 50 g. 85

Table 4.3. Volume loss (ΔV), friction coefficient (μ) and wear rate (W) after wear tests under 3N load against stainless steel ball.. 89

LIST OF FIGURES

Chapter 1

Figure 1.1. Diffractograms of samples BioH, BioSr, BioAl and BioAlSr as obtained and b) heat treated at 800°C for 2 hours. 25
Figure 1.2. Diffractograms of samples BioH, BioSr, BioAl and BioAlSr heat treated at 800°C for 2 hours. 26
Figure 1.3. FTIR spectra of a) untreated powder samples and b) after crystallization treatment at 800 °C for 2 hours. 27
Figure 1.4. DSC curves of powder samples BioH, BioSr, BioAl and BioAlSr up to 800 °C. 29
Figure 1.5. Glass compositions area variations (A/A0) from HSM as function of temperature. TFS = temperature of first shrinkage and TMS = temperature of maximum shrinkage. 31
Figure 1.6. Deconvolution of ^{29}Si MAS-NMR spectra of the glasses. 33
Figure 1.7. MAS-NMR spectra of 31P for bioactive glasses. 34
Figure 1.8. MAS-NMR spectra of 23Na for bioactive glasses. 35
Figure 1.9. MAS-NMR spectra of 27Al for bioactive glasses. 36
Figure 1.10. Deconvolution of Raman spectra of the glasses. 37

Chapter 2

Figure 2.1. Schematic summary of the stages of glass alteration behavior. (I) Leaching. (T) Transitional. (II) Precipitation and (III) Corrosion. 47
Figure 2.2. a) Dissolution rate ([g/cm²×s] × 10^{-7}), cumulative weight loss, pH and salinity in function of time (days) during the dissolution test. 49
Figure 2.3. ^{29}Si MAS-NMR spectra for all glasses. 50
Figure 2.4. Appearance of glass surface after 14 days of static dissolution a) BioH; b) BioAl; c) BioSr; d) BioAlSr. 52
Figure 2.5. SEM/EDS micrographs of monolytic samples after 14 days of static dissolution test a) BioH; b) BioAl; c) BioSr; d) BioAlSr. 53
Figure 2.6. Raman spectra collected from a) BioH; b) BioAl; c) BioSr; d) BioAlSr after 14 days of static dissolution test. 54

Figure 2.7. Transmittance FT-IR spectra of samples before and after 1, 7 and 14 days of hidrolytic atack. 56
Figure 2.8. Appearance of glass particles before and after 1, 7 and 14 days of hidrolytic atack.. 57

Chapter 3

Figure 3.1. FT-IR of powder sample before SBF test. 65
Figure 3.2. FT-IR of powder sample after SBF test. 66
Figure 3.3. pH mesurements during SBF test. 67
Figure 3.4. SEM/EDS micrographs of powder samples after 8h-SBF test. 69
Figure 3.5. Cumulative weight loss (%) in function of time (days) during the dissolution test……………………………………………………………………..71
Figure 3.6. X-ray diffraction patterns after SBF test at 7 and 14 days of each sample. 71
Figure 3.7. SEM micrographs after SBF test at 7 days a) BioH; b) BioAl; c) BioSr; d) BioAlSr. 72
Figure 3.8. SEM micrographs after SBF test 14 days a) BioH; b) BioAl; c) BioSr; d) BioAlSr. 72
Figure 3.8. Colony forming units (CFU ml-1) of E. coli versus concentration (ppm) of powder samples. 73
Figure 3.10. Cell viability (%) of BioH, BioAl, BioSr and BioAlSr (dotted line: reference cell viability of IC50). 74

Chapter 4

Figure 4.1. Cumulative distribution function for normalised toughness of all the glasses. 87
Figure 4.2. Weibull plots for the indentation toughness of all glasses. 87
Figure 4.3. Friction coefficient as function of sliding distance for samples sliding at 0.02 m/s under a 3 N contact load against a stainless steel ball. 88
Figure 4.4. Representative 3D final wear track topographies corresponding to BioH (a), BioAl (b), BioSr (c) and BioAlSr (d) as a function of depth (colored scale) under contact load 3 N against steel ball... 89
Figure 4.5. Representative SEM micrographs of the worn surface of BioH (a), BioAl (b), BioSr (c) and BioAlSr (d) after sliding against steel ball under normal

load of 3 N. Dashed lines are added to indicate the borders of the wear track for a better view. 90

Figure 4.6. 3-point Raman spectra collected from BioH (a), BioAl (b), BioSr (c) and BioAlSr (d). 92

Figure 4.7. Schematic representation of glass structure modifications and its implications on surface of a) BioH, b) BioAl, c) BioSr and d) BioAlSr. 95

CONTENTS

INTRODUCTION 18
AIM OF THE THESIS 19
CHAPTER 1: Thermal behavior and medium-range structure 20
1.1 Background 20
1.2 Experimental procedure 22
1.3 Results and discussion 24
1.3.1 Glass compositions and phase formation 24
1.3.2 Glass transition temperature and sintering behavior 28
1.3.3 The structure of the glasses 32
1.4 Chapter 1 Conclusions 39
REFERENCES 39
CHAPTER 2: Glass dissolution mechanism 44
2.1 Background 44
2.2 Experimental procedure 45
2.2.1 Sample preparation 45
2.2.2 Static dissolution experiments 45
2.2.3 Dynamic dissolution experiments 46
2.3 Results and Discussions 46
2.3.1 Interaction mechanisms between aqueous media and glasses 46
2.3.2 Static dissolution 48
2.3.3 Dynamic dissolution 55
2.4 Chapter 2 Conclusions 58
REFERENCES 58
CHAPTER 3: In vitro bioactivity and antibacterial capacity 61
3.1 Background 61
3.2 Experimental procedure 62
3.2.1 Sample preparation 62
3.2.2 In vitro bioactivity analysis… 62
3.2.3 SEM-EDS 63
3.2.4 Dynamic dissolution 63
3.2.5 Minimum Inhibitory Concentration (MIC) Determination 63
3.2.6 Cytotoxicity assay 64
3.3 Results and Discussion 64
3.3.1 In vitro bioactivity: powder samples 64

3.3.2 In vitro bioactivity: monolithic samples.. 71
3.3.3 Antibacterial sensitivity to E. coli 73
3.3.4 Cytotoxicity 74
3.4 Chapter 3 Conclusions 75
REFERENCES.. 75
CHAPTER 4: Tribological and mechanical behavior 80
4.1 Background 80
4.2 Experimental procedure 81
4.2.1 Sample preparation 81
4.2.2 Flexural strength and elastic modulus 81
4.2.3 Vickers hardness (HV) and fracture toughness (K_{IC})............................... 82
4.2.4 Wear test det-Up and conditions 82
4.2.5 Raman Spectroscopy 83
4.3 Results and Discussions 83
4.3.1 Mechanical properties 83
4.3.2 Tribological behavior 88
4.3.3 Raman Spectroscopy 91
4.3.4 Chapter 4 Conclusions 96
REFERENCES.. 96
5. FINAL CONCLUSIONS 100
6. FINAL CONSIDERATIONS 101

INTRODUCTION

This thesis concerns the preparation and characterization of a novel composition of bioactive glass. The study was conducted assuming composition-structure interplay a key role to achieve more efficient materials with tailorable properties.

Bioactive glasses, in general, represents a complex system with 4 or more compounds. There is not a consensus about how it might behave in contact with surroundings and to predict it is still a matter of debate.

The composition proposed is a 45S5-based one, once the 45S5 is the bioactive glass with more use and largely investigated under several conditions.

The aim was to modifiy the glass network by desestabilyzing it with oxides additions. The purpose was to enhance known 45S5 drawbacks with small additions of Al_2O_3 and SrO. It is important to stand that this is not a study of progessive substitutions and evaluation of its effects in glass properties. On the contrary, this study take advantage of the susceptibility of the system to deviate from linearity in ionic transport dependent properties with small changes in composition.

Therefore, the addition of two different ions may trigger the reorganization of the network without compromise the percolation channels. As a matter of fact, that reorganization promote a more cohesive structure where two immiscible liquids surround each other.

In Chapter 1, thermal properties, crystallization tendency, and sintering behavior was evaluated by differential scanning calorimetry, hot stage microscopy and dilatometry. Changes of medium-range structures were characterized by Q^n distribution of Raman spectroscopy and evaluation of ^{31}P, ^{27}Al, ^{23}Na and ^{29}Si environment obtained.

Chapter 2 report the mechanistic insights of the alteration in aqueous media by the qualitative study and comparison of a novel composition to other glass compositions.

Chapter 3 aimed to evaluate the in vitro bioactivity and antibacterial capacity against *E. coli.* of the proposed composition. Special emphasis was put on evaluating the effects of each ion (Sr and Al) to better understand their combined effect.

Chapter 4 consistis in the study of the tribological and mechanical behavior. The wear resistance (W) against stainless steel ball was evaluated as well as density, biaxial flexural and bending strength, hardness and elastic modulus.

AIM OF THE THESIS

A major goal of this thesis is to idealize a new multifunctional glass composition, that is, a glass not only bioactive, but also osteoinductive and biocidal. Although many bioactive glasses have been investigated by far, none have presented remarkable feature of strontium and aluminum to achieve versatility. In this sense this thesis comprehends the study and evaluation of the contribution of 2 mol% additions of strontium and aluminum to the enhancing of the thermal properties, strengthening of the mechanical properties and biological performance of bioactive glass compositions based on Bioglass® 45S5. Prior to studying correlations between compositions and pysico-chemical properties, a careful characterization of structure in local and mid range will be focused.

CHAPTER 1: Thermal behavior and medium-range structure

1.1 Background

Bioactive glasses are in general way compositions made from the Na_2O-CaO-SiO_2-P_2O_5 system and in some cases, associated with other metal oxides, but all characterized by forming a strong mechanical bond with the bone. The first bioactive glass was developed by Prof. Larry Hench in 1969 and has been widely used since the 80s because of its high biocompatibility. However, due to its high crystallization tendency and consequently limitation in applications that require heat treatments, many other glasses with distinct compositions has been also largely investigated [1–4].

Glasses as a versatile material accept a large range of distinct cations in its structure and can be easily modified. Still, the complexity in designing brand-new compositions as Bioglass® 45S5 is mainly due to the fact the more components involved results in more difficult to control the relationship between composition, structure, and bioactivity [5]. Also, the properties of bioactive compositions reflect their ability to release a critical amount of carbonate apatite precursors ions in the surrounding host tissue to stimulate cellular processes [6]. Since these properties and processes of interaction are directly related to the glass network connectivity [7,8], which can be evaluated by Q^n distribution, i.e. concentration of bridging oxygens (BO) per silicon tetrahedron that determinate random glass arrangement.

Among many new models and compositions proposed during the past decades, the ion substitution in 45S5 composition was highlighted. The idea of incorporating therapeutically active ions such as strontium and/or aluminum can contribute to a material with additional beneficial effects by providing tissue regeneration capabilities, enhanced bioactivity, and extended working range [9,10]. Strontium-containing bioactive glasses have already been recognized to affect bone growth in appropriate quantities [11–14]. Strontium itself has been used for osteoporosis prevention as a ranelate form (Protelos®)[15]. The strontium addition in bioactive glasses combines the known regenerative properties of bioactive glasses with anabolic and anti-catabolic effects of strontium ions. Alumina addition in contrast, in quantities above 3 mol% can inhibit or diminishes the interaction between material and host, however, its addition in small (up to 2 mol%) contents can enhance bioactivity, mechanical and thermal properties [16,17].

Considering the modification of glass compositions the careful design is the key factor to result in a suitable material for medical applications. The 45S5 Bioglass® was calculated near an eutectic point of the ternary soda lime silicate diagram due to its low melting temperature and as a composition with a high content of alkali cations is prone to percolate into channels and to exhibit mixed alkali effect even with small changes network connectivity.

Based on this effect and the responsive equilibria of 45S5, the substitution of 2 mol% of silicon by alumina was proposed. That is because, usually alumina at low concentrations is associated with silicate network as AlO_6 octahedra playing the role of stabilizer oxide, such as SrO. However, when alumina is present as AlO_4 tetrahedra it will be at SiO_4 tetrahedral network acting as a former oxide. The advantage of AlO_4 in the network is that improves physico-mechanical properties despite amplifying processing window and increases bioactivity. The difficult to obtain AlO_4 units in a complex system is that at concentrations lower than <5 mol% secondary formers ions (such as alumina) interact with the glass network in a way similar to alkali metals and alkaline earth metals [18], i.e. at low concentrations the R_xO_y acts as a network modifier. Substituting alumina in silicon percent is expected that the lack of former oxide and for network maintenance the alumina will replace silicon tetrahedral and so incorporate in network as AlO_4 units. Nevertheless, this will impact phosphorous sub network as calcium will be required to charge balance AlO_4 units. Then, an addition of 2 mol% of strontium was considered to contribute to the enrichment of phosphorous environment and possibly provide stronger bonding among fragments of silicon network compensating feasible weakening of its network by the presence of alumina. Strontium oxide acts as a modifier oxide and is known to improve bone growth and regeneration while maintaining the general chemical and physical behavior of the base glass composition [19].

Hence, to study substituted bioactive glasses compositions is still relevant to better understand how a strict chemical composition design can open a new way to functionalize structures of the bioactive glasses. Therefore the aim of this study is to elucidate the influence of low content of strontium oxide and alumina in four 45S5-based compositions, and consequently how they affect the glass structure and crystallization separately and their synergy when together. Also, the interaction between Al^{3+} and Sr^{2+} upon Bioglass-based compositions found in this study overcomes expectations reducing drawback of processing and empowering its use in applications whose requires a thermal treatment.

1.2 Experimental procedure

Four glass compositions containing Al_2O_3 and SrO were calculated in a molar base as presented in Table 1. For a more comprehensive study of the role of each oxide was considered samples containing them separately and together. Also, a sample of Bioglass® 45S5 (BioH) composition was made for comparative purposes. The glasses were prepared from reagent-grade SiO_2 (99.0 wt%), CaO (99.0 wt%), Na_2CO_3 (95.0 wt%), Al_2O_3 (99.0 wt%), $Ca(H_2PO_4)\cdot 2H_2O$ (99.0%) and $Sr(NO_3)_2$ (99.0 wt%). Batches of 30g were obtained by homogenizing the raw materials in an agate mortar for 10min and subsequently melted into a Pt-5%Au crucible at 1500 °C for 1h in a vertical electric furnace. The glasses were cast into bar molds (30×10×10) mm, annealed at 470 °C for 2h and slowly cooled down to room temperature to remove thermal strain. The bulk samples were reserved, and part was crushed and the particle size was reduced using an agate milling ball and then sieved to a size below 50 μm. The amorphous state of the samples was confirmed by powder X-ray diffraction (XRD; Bruker D8 ADVANCE); using CuKα radiation with 2θ from 10 to 70° and step of 0.1°/s.

In order to verify the crystalline phases in the studied compositions, the powders were axially pressed into discs and then, a heat treatment was carried out in a tubular furnace at 800ºC for 2 hours under ambient atmosphere above a platinum plate. Phase identification of heat treated samples was carried out by comparing XRD pattern obtained in the same conditions mentioned above with the standard JCPDS files.

The thermal behavior of obtained samples was investigated by DSC (Netzsch, DSC 404F3 PEGASUS) recorded at constant heating rate of 10K·min^{-1} up to 800 °C to obtain glass transition (T_g), and onset crystallization temperatures (T_x). Dilatometry (Bähr Thermoanalyse DIL 802) was conducted by the heating rate 5 K·min^{-1} to obtain T_g and thermal expansion coefficient (TEC) determined at 500 °C using the dilatometry curves in the temperature range between 100 and 500 °C.

A side-view hot-stage microscope (HSM; EM 201) equipped with image analysis system and electrical furnace 1750/15 Leica was also used to obtain liquidus temperature and characteristic viscosity points (first shrinkage T_{FS}, maximum shrinkage T_M and flow T_l). The measurements were conducted in air with a heating rate of 10K min^{-1}. The samples, cylinder-shaped and placed on an alumina support, were prepared with cold-pressed glass powder. The temperature was measured with a Pt/Rh (6/30) thermocouple contacted under the alumina support.

Fourier Transform Infrared Spectroscopy (FTIR, Bruker IFS 66 VS) was performed by using a diffuse reflectance attachment within a range of 400 to 4000 cm^{-1} and a resolution of 2 cm^{-1}. The analysis provided an outlook of the evolution of the network connectivity according to changes in composition and also, after the crystallization heat treatment.

Magic angle spinning nuclear magnetic resonance (MAS-NMR; Bruker Advance 400) experiments were performed at room temperature for ^{29}Si (79.48 MHz) and ^{27}Al (104.26 MHz). ^{31}P (161.98 MHz) and ^{23}Na (105.80 MHz). Glass powders were packed into zirconia rotors. The samples were spun at 10 kHz, the number of scans 120 with a recycle delay time set to 10s to minimize saturation effects. Estimated errors for chemical shifts and relative area are 0.2 ppm and 2% respectively. The analysis of ^{29}Si NRM spectra was carried out with the Fityk software assuming Gaussian peak profile. From the fitting of experimental envelopes, relative intensities of different components were deduced.

Raman spectroscopy was analyzed by using a micro-Raman spectrometer (WITEC, Confocal Raman Microscope Alpha300 R). The samples were excited by the 532 nm line of an Ar^+ laser and recorded with microscope objective 50x/0.7 at 60s integration time with 45 mW power. The frequencies and number of Raman bands reported in this study were obtained by considering Q species and vibrational groups contained in the kind of glasses and assuming Gaussian peak profile.

1.3 Results and discussion

1.3.1 Glass compositions and phase formation

In view that 45S5 belongs to the system SiO_2:CaO:Na_2O:P_2O_5 of which typical composition is given by 45.0SiO_2:24.5Na_2O:24.5CaO:6.0P_2O_5 (in wt%), this research was conducted by modifying it through the charge balance destabilization of the vitreous network by previous addition of alumina and further, SrO in excess.

At 45S5 one third of the silicon tetrahedron atoms corresponds to bridging oxygens (BO). Its structure is dominating chain-like (most Q_{Si}^2 units) occasionally attracted to each other by calcium (Ca^{2+}) ions. The role of calcium in these compositions is very important because its mobility dictates the ion exchange when in contact with an aqueous media [20–22]. So, is directly connected to bioactivity. Either calcium, strontium or sodium ions have more affinity to bond with phosphorous than silicon. Also, by field strength, the preference of NBOs will be Ca > Sr > Na. Recent studies already stated that there is no sign of Si-O-P bonds in 45S5, confirming the phase separations in this composition. Assuming the presence of phosphorous only as orthophosphate (PO_4^{-3}) its charge will be compensated by Ca^{2+} and Na^+ will be rich [23].

Compositions, as calculated and obtained determined by X-ray fluorescence chemical analysis, are presented in Table 1.1 expressed in mol%. The XRD pattern of the glasses is plotted in Figure 1.1.

Table 1.1. Nominal and measured (in parentheses) composition in mol%.

Sample	SiO_2	P_2O_5	Na_2O	CaO	Al_2O_3	SrO
BioH(45S5)	46.1 (47.3)	2.6 (2.7)	24.4 (23.5)	26.9 (26.5)	-	-
BioAl	44.1 (46.5)	2.6 (3.3)	24.4 (21.0)	26.9 (26.8)	2.0 (2.4)	-
BioSr	45.2 (46.0)	2.5 (2.4)	23.9 (23.1)	26.4 (26.5)	-	2.0 (2.0)
BioAlSr	43.2 (43.7)	2.5 (2.3)	23.9 (23.3)	26,4 (26.2)	2.0 (2.3)	2.0 (2.2)

Figure 1.1. Diffractograms of samples BioH, BioSr, BioAl and BioAlSr as obtained and b) heat treated at 800°C for 2 hours.

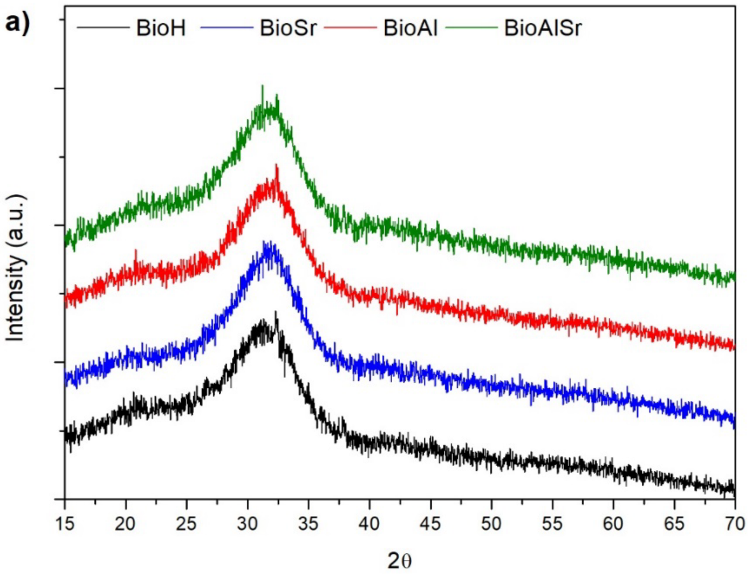

Source: the author.

The samples obtained were homogeneous and XRD confirmed their amorphous state. Still, despite of it, all samples showed a broad shoulder in smaller 2θ angles, indicating an overlap of halos. This particularity has already been reported by other authors [24,25] in 45S5 and similar bioactive glasses that contain more than one alkali metals and can be an indication of the glass-in-glass phase separation of the material, i.e., the segregation of two molten liquids before critical cooling. This is because each oxide plays a role in the glass structure formation acting as former, intermediaries or modifiers. The 45S5 composition although belonging to a system that contains silicon and phosphorus oxide both primary former only silicon oxide act like a former while phosphorous as orthophosphate (PO_4^{3-}) commonly segregates in clusters or subphase associated with Ca^{2+} [18].

The study of the effect of heat treatment of bioactive glasses and the nature of the phase produced is important because it is required for several technical applications besides helping explore changes in arrangement e tendency of phase formations as compositions are modified. In order to investigate the crystalline phases in the present compositions the heat treatment was taken in higher temperature - at 800 °C for 2 hours - that’s because by this temperature considering the existence of two different phases – one rich in silicon and other rich in phosphorous – both correspondent crystalline phases will be already developed [26]. The analysis of the XRD patterns after heat-treating is presented in Figure 1.2.

Figure 1.2. Diffractograms of samples BioH, BioSr, BioAl and BioAlSr heat treated at 800°C for 2 hours.

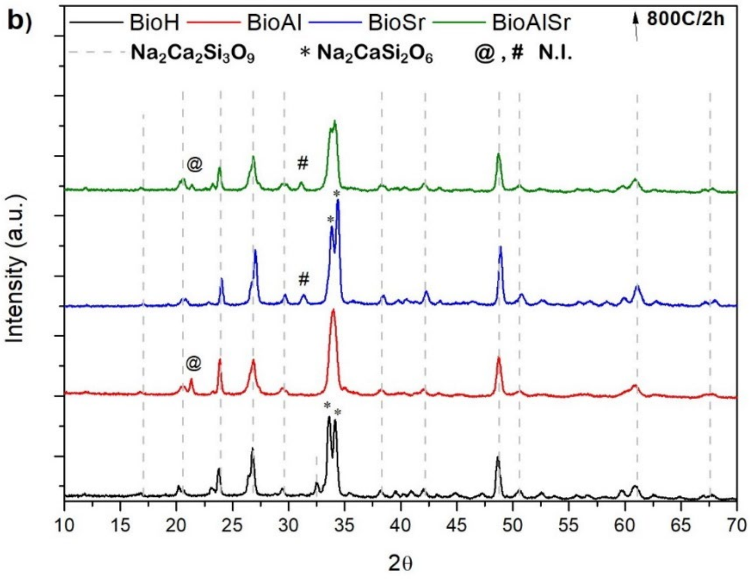

Source: the author.

All spectra showed the presence of sodium-calcium-silicate - which is supposed to be the main crystalline phase [27]. Although the known difficulty in identifying the exact sodium-calcium-silicates phases since they exhibit very similar reference patterns, 45S5 like compositions belong to combeite precipitation field. Still, Lefebvre et al. [28] reported that structural transformations during heat treatment should be noted. Considering both SearchMatch database and references the best fitting for all glasses spectra was to the patterns of combeite ($Na_2Ca_2Si_3O_9$; JCPDS 22-1455). However, taking in account peaks at 23.8°, 33.8° and 34° (2 theta) a significant difference was noticed. For BioH and BioSr the peak at 23.8° was more intense and the peak at 34.1°(exhibited in BioAl and BioAlSr) was decomposed into two at 33.8° and 34.1° (*) these patterns is usually attributed to high combeite ($Na_2CaSi_2O_6$; JCPDS 77-2189) kown to be isostructural to combeite itself. In general, high combeite is formed in higher temperatures (> 900 °C) however small changes in P2O5/NaO or prolonged heat treatment can accelerate its formation. The earlier formation of high combeite and other peaks less intense between 50° and 60° in BioH and BioSr could indicate a higher tendency to crystallization in comparison with BioAl and BioAlSr. Despite it not identified peaks placed on 21.4° (@) for alumina-containing glasses (BioAl and BioAlSr) and on 31.1° (#) for strontium-containing glasses (BioSr and BioAlSr) was observed. No phosphate-rich or strontium-containing phases were observed that is probably because they were below detectable levels.

The FT-IR spectra of untreated and crystallized glass powders are shown in Figure 1.3.

Figure 1.3. FTIR spectra of a) untreated powder samples and b) after crystallization treatment at 800 °C for 2 hours.

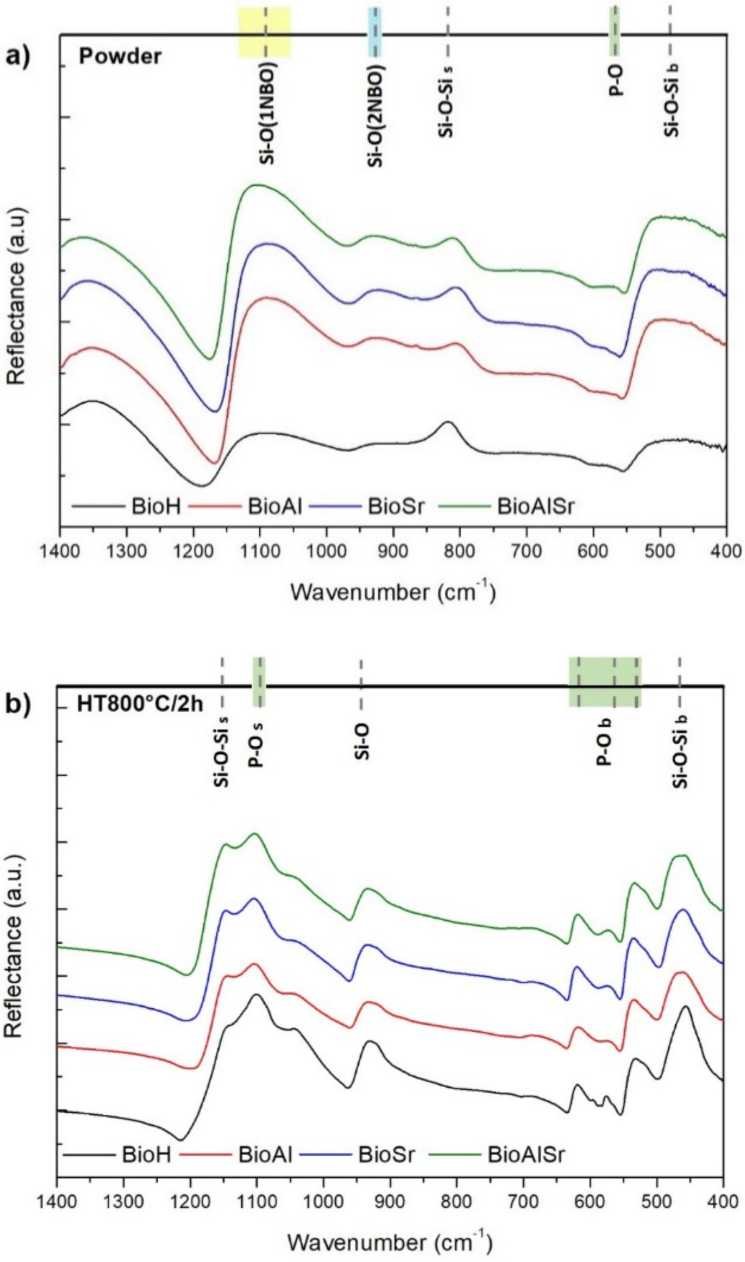

Source: the author.

The spectra of untreated samples exhibited three broad bands in the region of 400-1400 cm^{-1}. This lack of specific features is indicative of the disorder of silicate and phosphate networks, and especially of the wide distribution of Q^n units in these glasses [18,20]. The most intense bands are in the region of 800 to 1300 cm^{-1} and correspond to the stretching vibrations of the silica tetrahedron with a different number of BOs or NBOs. And in all glasses this region is divided into two transmission bands, one at 940 cm^{-1} assigned to the structure Q^2 (Si-O(2NBO)) and a second band in the range of 1000 to 1100 cm^{-1}, Si-O-Si always associated with Q^3 units. The third is the band less intense at 490 cm^{-1} assigned to Si-O-Si (bend). Peak development at 830 cm^{-1}, present in all samples, can be assigned to Si-O-Si s vibration between two neighboring SiO_4 tetrahedra [29,30]. A minor peak at 560 cm^{-1} attributed to amorphous P-O bend , in general increases as crystallization occurs.

The spectra of crystallized samples which were heat presented significant changes where the original broad bands are decomposed into several peaks and a new peak at 575 cm^{-1} emerges that could be related to the new crystalline phase. These changes are also highly connected to phosphorous content and occurrence in the glass network since vibrational modes of P linkages are mostly in the region between 472 and 602 cm^{-1} [29].

1.3.2 Glass transition temperature and sintering behavior

In order to evaluate the work temperatures and events that could affect the properties of the material after prepared, were performed DSC analysis (Figure 1.4), dilatometry and hot stage microscopy.

Figure 1.4. DSC curves of powder samples BioH, BioSr, BioAl and BioAlSr up to 800 °C.

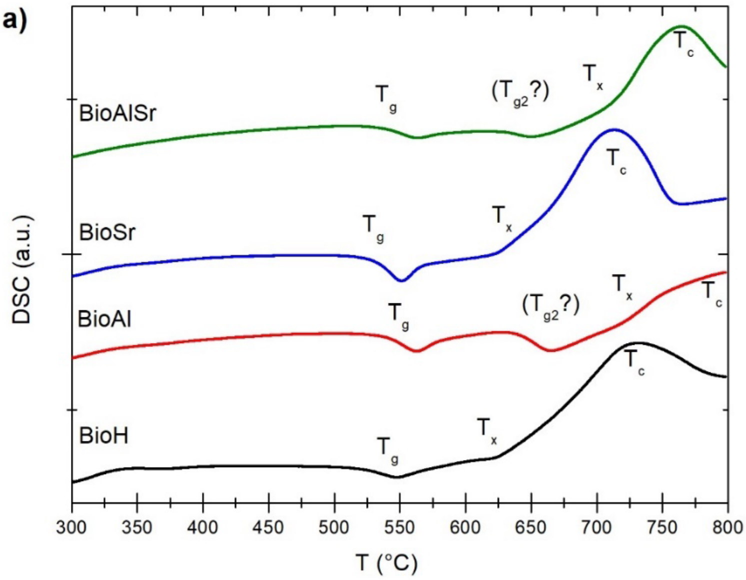

Source: the author.

From the obtained data, based on their thermal events, it was possible to determine the temperatures of glass transition (T_g), onset crystallization (T_x) and liquidus (T_l), and thermal expansion coefficient (TEC) at 500 °C ($\alpha_{500°C}$). All the determinate temperatures are given in Table 1.2 as well as stability parameters such as processing window ($\Delta T = T_x - T_g$), glass stability against crystallization (K_H) and sinterability (S_c) [31,32].

Table 1.2. Glass properties: Temperatures (°C) of glass transition (T_g), onset of crystallization (T_x) obtained from DSC curves, first shrinkage (T_{FS}), maximum shrinkage (T_{MS1};T_{MS2}) and liquidus (T_l). Parameters of glass stability S_c, ΔT and K_H(°C) and thermal expansion coefficient at 500°C ($\alpha_{500°C}$).

Technique	**DSC (±2 °C)**		**HSM (±5 °C)**				**Parameters**			**Dilatometry**
Sample	T_g	T_x	T_{FS}	T_{MS1}	T_{MS2}	T_l	S_c	ΔT	K_H	$\alpha_{500°C}$
BioH	520	626	569	609	927	1198	17	106	0.19	14.89×10^{-6}
BioAl	528	720	564	593	1089	1233	127	192	0.37	16.90×10^{-6}
BioSr	539	621	534	557	1110	1140	64	82	0.16	15.64×10^{-6}
BioAlSr	530	701	529	588	987	1151	113	171	0.38	15.69×10^{-6}

Considering the presence of two sub-network and so two Tg, from the DSC curves was possible to observe that all samples did not present substantial changes in Tg - corresponded to the silicate phase (majority phase due to its concentration) - occurring between 520 °C (BioH) and 539 °C (BioSr). In contrast, a significant displacement of the crystallization peak was observed in samples containing alumina (BioAl and BioAlSr) besides evidencing the presence of a second T_{g2} – event already observed in bioactive glasses containing more than one alkali [8,33–35] – suggesting the impact of both alumina and strontium mostly in the orthophosphate sub-network. The TEC obtained at 500 °C from dilatometry varied from 14.89 x 10^{-6} (BioH) to 16.90 x 10^{-6} (BioAl) and were very similar for BioSr and BioAlSr corresponding to 15.64 and 15.69 x 10^{-6} respectively. Both alumina and strontium oxide presence caused an increase in TEC. By far the effect of strontium addition in TEC of bioactive glasses was not investigated. In general, the presence of alumina in glasses affects the thermal expansion causing a decrease in TEC due to its octahedral (AlO_6) coordination in the structure. However, we have noticed an increase of TEC in BioAl that could be because of the change in coordination in this composition suggesting the presence of tetrahedral alumina (AlO_4) generating covalent bonds with silicon which can cause an expansion of the network [9,36]. For all samples, TEC obtained was close to BioH and so adequate for biotechnical applications such as coatings.

The sintering behavior of the glasses was studied by investigating fine-grained powder using HSM. Figure 1.5 shows the sintering curves given as to area variation (A/A_0) as function as temperature for all glasses.

Figure 1.5. Glass compositions area variations (A/A0) from HSM as function of temperature. TFS = temperature of first shrinkage and TMS = temperature of maximum shrinkage.

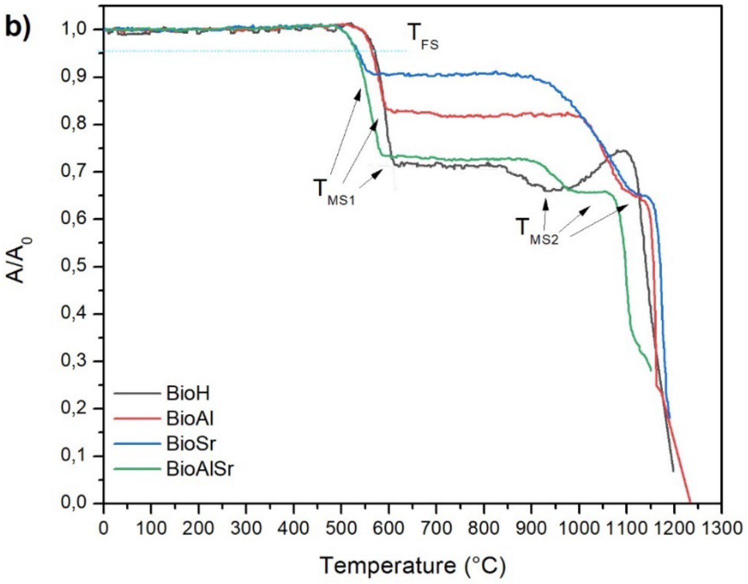

Source: the author.

The sintering temperature (T_{FS}) indicated in the image is defined by DIN51730 as the shrinkage of the initial sample height to 95%. The T_{MS} is the starting temperature of the plateau of constant sample height after the first shrinkage. Apparently, the addition of strontium has caused a decrease in T_{FS}. The samples exhibited two stage sintering behavior implicating in the presence of two T_{MS}. The conclusion of first shrinkage stage is identified as T_{MS1} while of the second is T_{MS2}. For all glasses, the T_{MS1} was lower than crystallization temperature onset ($T_{MS1} < T_x$) meaning sintering precedes crystallization and so appears as an independent process. Still, a great difference in shrinkage was notice indicating different compacting behavior. Whereas BioH and BioAlSr contract ~30% of the area at the T_{MS1}, BioAl shrinkage was about ~20% and BioSr only ~10%. Nevertheless, at T_{MS2} all samples presented a similar reduction in area about 35% resulting in good densification.

From temperatures obtained by both DSC curves and HSM (considering T_{MS1} as the predominant phase in all compositions) is possible to measure the glass stability against crystallization in two ways. One by the parameter proposed by Hruby, K_H which depends on temperatures of onset crystallization (T_x), glass transition temperature (T_g) and flow/liquidus temperature (T_l) where the larger the parameter calculated greater the stability against crystallization on heating. On the other hand by the sinterability parameter (S_c) proposed by C. Lara et al. [31] which is given by T_x - T_{MS} and estimates the competition between sintering and crystallization where the greater the difference the more independent is the kinetics of both processes [37]. These two parameters must also be in accordance with ΔT, known as the process window and given by T_x - T_g. Glass BioH already recognized for its poor processing window and high tendency to crystallization presented the smaller values of both parameters indicating how associated are the kinetics of sintering and crystallization. BioSr, as well as BioH, presented high dependency only with a larger ΔT. Otherwise, both glasses containing alumina, BioAl and BioAlSr presented larger Sc which indicates better sintering/crystallization behavior and twice K_H compared to BioH and amplified processing window.

1.3.3 The structure of the glasses

The bioactive glasses are usually formed by open silicate network i.e. interconnected in a combination of Q_{Si}^2 (chains and rings) and with a lower incidence of other Q_{Si}^3 species. In respect of glass network arrangement, both P^{5+} and Si^{4+} tend to occur in tetrahedral coordination in oxide glasses. However, when the two elements are present in suchlike 45S5 compositions and for bioactive purposes, silicon will always act as network-former dictating the network-polymerization and phosphorous predominantly as orthophosphate ions cooperating to ensure the ionic mobility in aqueous medium by an accessible structure [38–41].

Figures 1.6 shows ^{29}Si MAS-NMR spectra and Table 1.3 specifies the deconvolution components and their percentages calculated from fractional areas.

Figure 1.6. Deconvolution of ^{29}Si MAS-NMR spectra of the glasses.

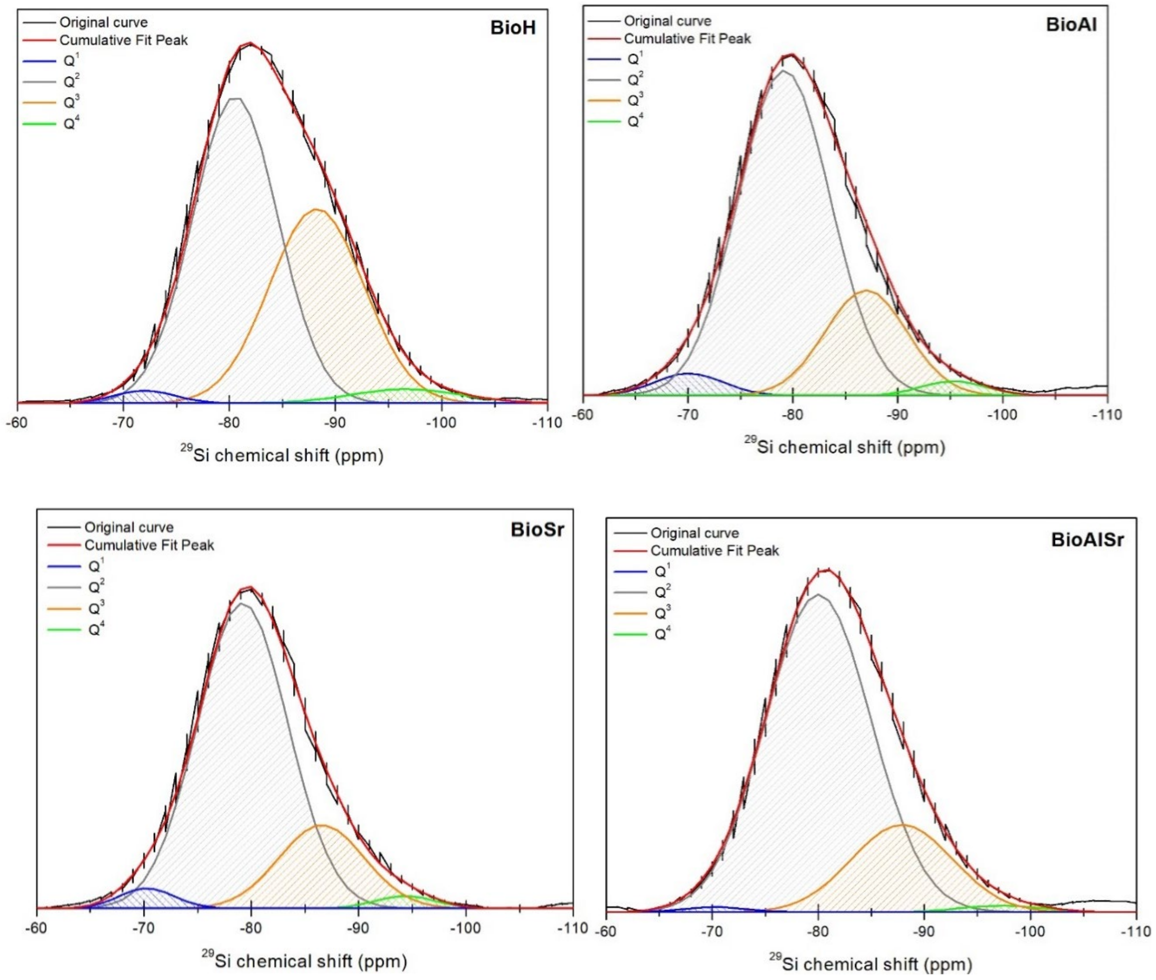

Source: the author.

Table 1.3. ^{29}Si MAS-NMR parameters of the bioactive glasses: Qn distribution by peak deconvolution and % calculated from the fractional areas.

Sample	Q^1		Q^2		Q^3		Q^4	
	Center (ppm)	%Area	Center (ppm)	%Area	Center (ppm)	%Area	Center (ppm)	%Area
BioH	-70.98	1.63	-80.55	55.85	-88.23	39.20	-96.64	3.31
BioAl	-70.07	3.65	-79.18	73.08	-87.98	21.05	-96.28	2.21
BioSr	-70.29	2.91	-80.01	76.53	-87.57	18.59	-96.34	1.97
BioAlSr	-70.22	0.75	-80.01	77.49	-87.90	20.50	-97.37	1.25

The spectra comprise four contributions: some residual Q_{Si}^1 and Q_{Si}^4 groups at -70 and -96 ppm respectively, Q_{Si}^2 at -80 ppm and QSi3 at -88 ppm. Even though all samples presented a similar spectrum and a chemical shift centered near -80 ppm indicating that Q_{Si}^2 units dominate the distributions, the center moved towards a higher resonance frequency. As a result, excluding BioH, all modified samples presented a gain in Q_{Si}^3 units in function of Q_{Si}^2. For instance, the fractional area of Q_{Si}^3 changed from 56 for BioH to 77% for BioAlSr.

Figure 1.7 shows the 31P MAS-NMR chemical shift for the glasses.

Figure 7. MAS-NMR spectra of 31P for bioactive glasses.

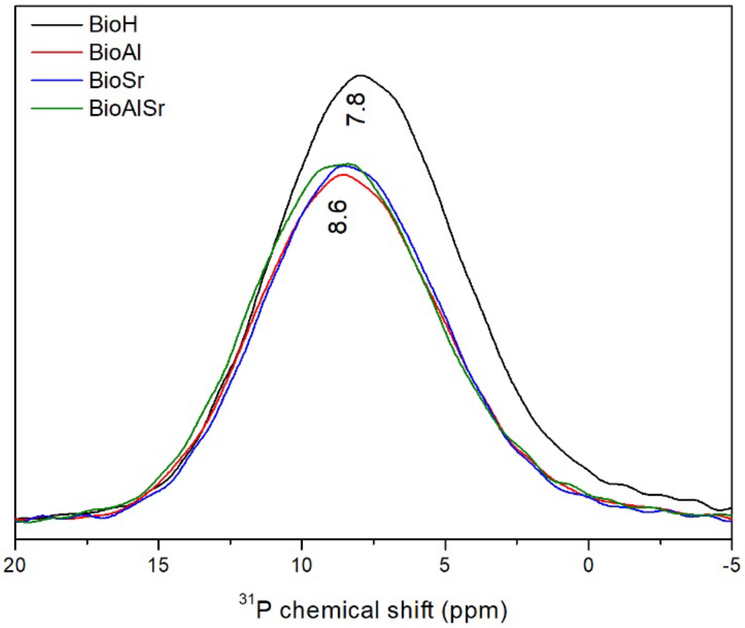

Source: the author.

All spectra obtained are in the range of orthophosphate environment (PO_4^{3-}) known for charge balance with a mixture of modifier cations. The spectra are centered at ≈8 ppm and located in the region between sodium (16 ppm) and calcium (3 ppm) orthophosphate. This reinforces that phosphorous in the extent compositions did not enter the glass network acting as a former oxide and so is not associate either with silicon or aluminum (in case of BioAl and BioAlSr). Also, the presence of alumina in 2 mol% did not affect the required charge compensation of orthophosphate species. Furthermore, comparing the samples with BioH, it can be noticed that their center presented a slight displacement towards higher ppm values, i.e. sodium orthophosphate environment. That throw could suggest a greater contribution of Q_{Si}^2 structure [38,42]. The ^{29}Si MAS-NMR chemical shift previously discussed evidence of this suggestion.

Figure 1.8 shows ^{23}Na MAS-NMR spectra of the glasses.

Figure 1.8. MAS-NMR spectra of 23Na for bioactive glasses.

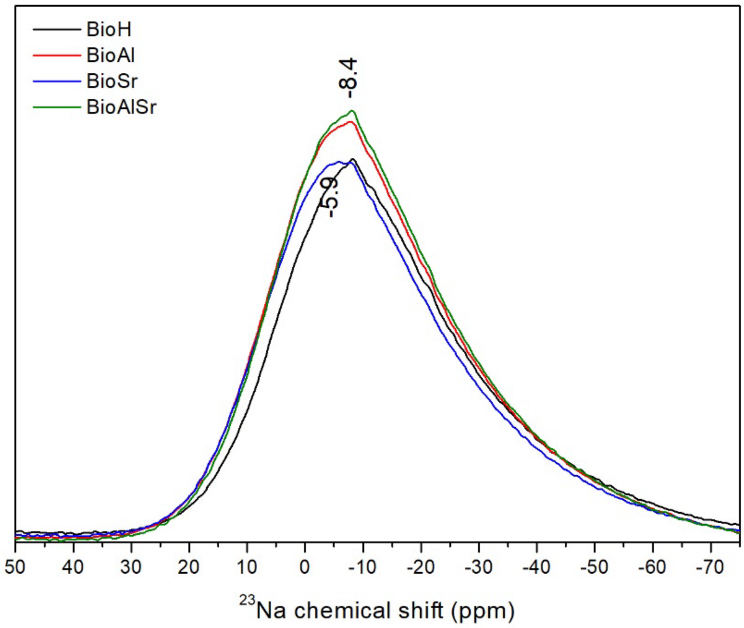

Source: the author.

BioH, BioAl and BioAlSr spectra were similar displaying one asymmetric broad component centered at -8.4 ppm. However, BioSr spectra presented a slight displacement towards positive values centered at -5.9 ppm. Despite this change, no significant differences were detected suggesting that most sodium ions occupy similar environments.

Figure 1.9 shows ^{27}Al MAS-NMR spectra of glasses BioAl and BioAlSr indicates that aluminum atoms were successfully integrated to silicate network by presenting a resonance centered at 59,5 ppm characteristic of the four-coordinated form ($Al(OSi)^{4-}$), whose negative charge is charge balanced by Ca^{2+} ions. The results are in accordance with the displacement found in ^{31}P NMR spectra where a favoring of sodium orthophosphate environment was observed in detriment of a smaller quantity of Ca^{2+} available.

Figure 1.9. MAS-NMR spectra of 27Al for bioactive glasses.

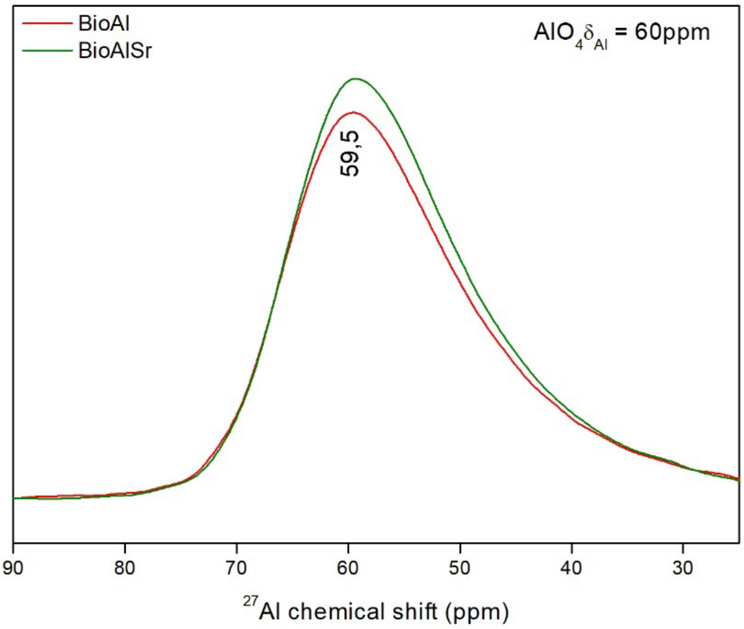

Source: the author.

Apart from NMR, Raman spectroscopy is a complementary tool to determine the structure, environment, and dynamics of glassy materials. Also, it was the only technique for this purpose performed in bulk instead of powder sample, i.e. on the surface of the obtained material. In silicate glasses, the bands of most interest associated with vibrations of asymmetric and symmetric stretching are in the region between 800 and 1200 cm^{-1}. For either spectroscopy and deconvolution set up was adopted method created by Mysen et al. and Brow [43,44]. For better fitting (the correlation coefficient $R^2 > 0.998$) was assumed the presence not only of Q_{Si}^2, Q_{Si}^3 but Q_{Si}^0 and Q_{Si}^1 as well. So, the attributions considered for the fitting were:

(I) 864 cm^{-1} of Q^0 units;

(II) 906 cm^{-1} of Q^1 units;

(III) 944 cm^{-1} of Q^2 units;

(IV) 974 cm^{-1} for P-O-P stretching;

(V) 1008 cm^{-1} 0O-P-O- stretching of P_2O_5 sheet unit;

(VI) 1044 cm^{-1} asymmetric stretching of bridge oxygen (BO) in all Q species;

(VII) 1086 cm^{-1} symmetric stretching of Q^3 units.

Figure 1.10. Deconvolution of Raman spectra of the glasses.

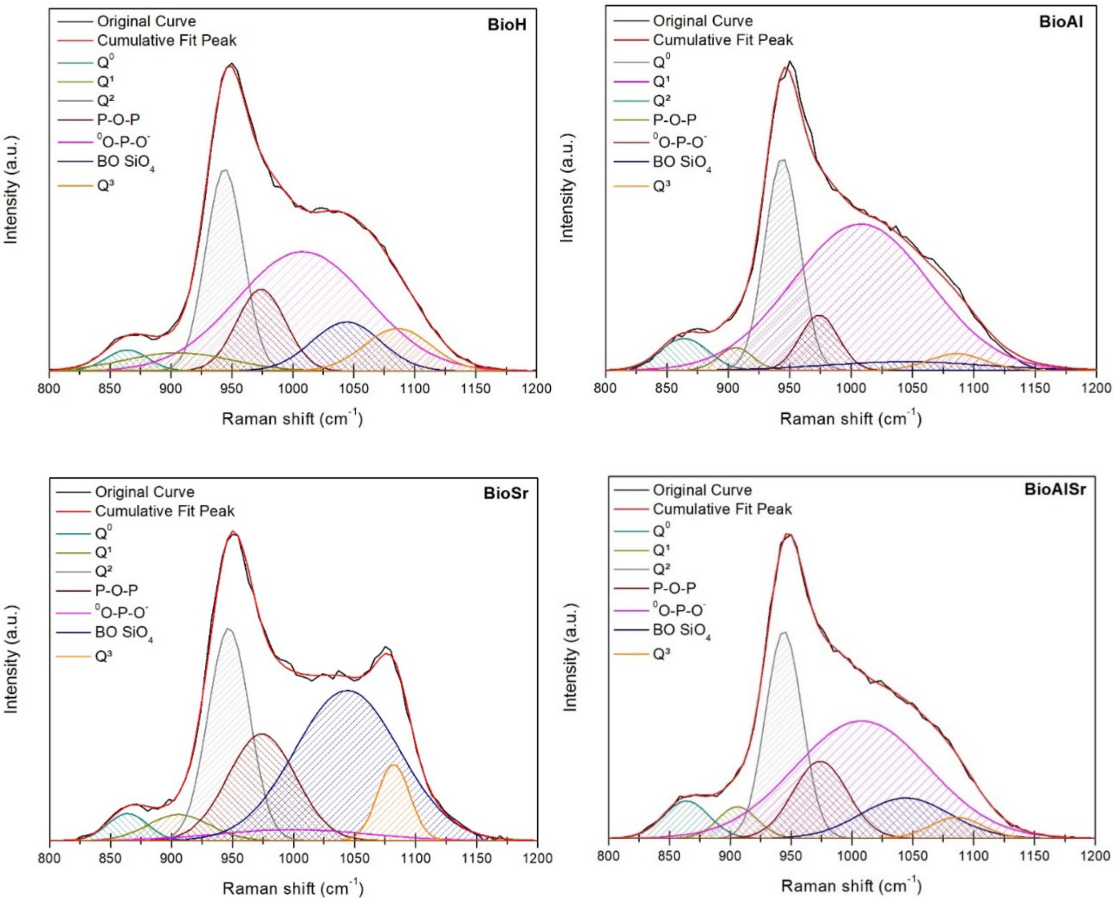

Source: the author.

Table 1.4. Frequencies and percentages for Raman bands of the bioactive glasses.

Sample	%Q^0, 864	%Q^1/ O-O, 906	%Q^2, 944	%P-O-P, 974	%^{0}O-P-O$^-$, 1008	%BO SiO$_4$, 1044	%Q^3, 1086
BioH	2.44	5.31	20.95	11.02	43.12	9.32	7.84
BioAl	4.48	2.28	21.67	6.21	58.70	3.95	2.72
BioSr	2.81	4.18	22.78	18.76	4.26	40.77	6.46
BioAlSr	4.83	3.55	21.65	11.96	44.73	10.16	3.14

Agreeing with NMR results all samples presented a high intensity for QSi^2 units. No significant changes were observed in respect of Q species however, P bands were very sensitive for this analysis. Although P units are present in the network as orthophosphate in BioSr was observed a bigger loss from the contribution at 1008 cm-^{1} corresponded to 0O-P-O- stretching of P_2O_5 sheet unit to a direct gain at 1044 cm^1 characteristic of asymmetric stretching of bridging oxygen in all Q species. It seems that the incorporation of strontium does not cause a considerable change at the local sphere but in a mid-range scale, its presence influences the arrangement of P in the glass network. It is known the role of P in the bioactive glasses and that its specific amount triggers the phase separation in this kind of multi component glass[45]. Also, many studies were taken in account the probability of network modifiers cluster, such as Na, Ca and Sr especially if there are small changes in the alkali ratio (Na:Ca/Sr) which do not alter network connectivity but changes will be reflected at most of the chemical and physical glass properties. Likewise, it was found that phosphorous and Ca/Sr ions are preferentially clustered [46,47]. It can be stated that the presence of an excess of strontium has favored glass in glass separation clustering with phosphorus instead of being in a linear sheet sub-network with phosphorus as expect and observed in the other samples. To be representative each sample was three times evaluated by changing the zone of measurement, in the samples BioH, BioAl and BioAlSr all spectra were similar, unlike BioSr which all spectra (not presented in this article) was distinct, supporting the clustering theory.

Finally, the increase in stretching asymmetric BO in silicon tetrahedral could be due to a change in the Q_{Si}^2 units. As previous mentioned Q_{Si}^2 in a suchlike composition can occur in chains and/or ring units and their occurrence is directly connected with their number and coordination of oxygens. Usually, there is no difference observed at a chemical shift in NMR analysis, but it can be evaluated from the crystalline phase raised from the thermal temperature at adequate temperatures. As observed from the diffractogram of treated samples a different phase of combeite was formed in BioSr. According to Volzone and Stábile [27] both high and low combeite would be formed by similar composition and depends on sodium and calcium content in phosphorous environment. Still, they observed that higher sodium content with phosphorous originated greater relative amount of high combeite ($Na_2CaSi_2O_6$).

1.4 Chapter 1 Conclusions

The use of small quantities of oxides in the novel composition presented is potentialized by the presence of a secondary vitreous former. The results revealed that the incorporation of Al_2O_3 as a four-coordinated form was essential for optimize the influence of SrO in the system. The tendency of 2 mol% of strontium oxide to trigger its segregation into clusters was inhibited with the presence of Al_2O_3. Despite Q^n distribution was predominantly Q^2 in all samples the composition criteria used caused a rearrangement of silica network impacting principally thermal properties enabling improved processing and stability characteristics. The addition of Al_2O_3 and SrO into BioAlSr promoted a larger sinterability parameter which indicates better sintering behavior, the glass stability against crystallization doubled compared to 45S5 (BioH) and the processing window enlarged from 106 to 171. Also, developed BioAlSr revealed to maintain the formation of combeite type of crystalline phase after heat treatment at 800 °C for 2 hours. The findings in this study outperform poor processing window and high tendency to crystallization of Bioglass® 45S5 apart from highlight important differences in ways of interaction of 2 mol% of strontium in 45S5 and in a composition where a small amount of alumina acts partially as former oxide.

REFERENCES

[1] A.R. Boccaccini, Q. Chen, L. Lefebvre, L. Gremillard, J. Chevalier, Sintering, crystallisation and biodegradation behaviour of Bioglass®-derived glass-ceramics, Faraday Discuss. 136 (2007) 27–44. doi:10.1039/b616539g.

[2] D. Groh, F. Döhler, D.S. Brauer, Bioactive glasses with improved processing. Part 1. Thermal properties, ion release and apatite formation, Acta Biomater. (2014). doi:10.1016/j.actbio.2014.05.019.

[3] S. Kargozar, M. Montazerian, E. Fiume, F. Baino, Multiple and Promising Applications of Strontium (Sr)-Containing Bioactive Glasses in Bone Tissue Engineering, Front. Bioeng. Biotechnol. 7 (2019). doi:10.3389/fbioe.2019.00161.

[4] G. Kaur, V. Kumar, F. Baino, J.C. Mauro, G. Pickrell, I. Evans, O. Bretcanu, Mechanical properties of bioactive glasses, ceramics, glass-ceramics and composites: State-of-the-art review and future challenges, Mater. Sci. Eng. C. (2019). doi:10.1016/j.msec.2019.109895.

[5] J.P. Hamilton, C.G. Pantano, Effects of glass structure on the corrosion behavior of sodium-aluminosilicate glasses, J. Non. Cryst. Solids. 222 (1997)

167–174. doi:10.1016/S0022-3093(97)90110-1.

[6] L.L. Hench, N. Roki, M.B. Fenn, Bioactive glasses: Importance of structure and properties in bone regeneration, J. Mol. Struct. 1073 (2014) 24–30. doi:10.1016/j.molstruc.2014.03.066.

[7] J. Massera, L. Hupa, Influence of SrO substitution for CaO on the properties of bioactive glass S53P4, J. Mater. Sci. Mater. Med. 25 (2014) 657–668. doi:10.1007/s10856-013-5120-1.

[8] R.G. Hill, D.S. Brauer, Predicting the glass transition temperature of bioactive glasses from their molecular chemical composition, Acta Biomater. 7 (2011) 3601–3605. doi:10.1016/j.actbio.2011.06.023.

[9] S.M. Rabiee, N. Nazparvar, M. Azizian, D. Vashaee, L. Tayebi, Effect of ion substitution on properties of bioactive glasses: A review, Ceram. Int. 41 (2015) 7241–7251. doi:10.1016/j.ceramint.2015.02.140.

[10] S. Kargozar, F. Baino, S. Hamzehlou, R.G. Hill, M. Mozafari, Bioactive glasses entering the mainstream, Drug Discov. Today. 23 (2018) 1700–1704. doi:10.1016/j.drudis.2018.05.027.

[11] A. Moghanian, S. Firoozi, M. Tahriri, A. Sedghi, A comparative study on the in vitro formation of hydroxyapatite, cytotoxicity and antibacterial activity of 58S bioactive glass substituted by Li and Sr, Mater. Sci. Eng. C. 91 (2018) 349–360. doi:10.1016/j.msec.2018.05.058.

[12] S.K. Arepalli, H. Tripathi, S.K. Hira, P.P. Manna, R. Pyare, S.P.Singh, Enhanced bioactivity, biocompatibility and mechanical behavior of strontium substituted bioactive glasses, Mater. Sci. Eng. C. 69 (2016) 108–116. doi:10.1016/j.msec.2016.06.070.

[13] J.K. Christie, N.H. de Leeuw, Effect of strontium inclusion on the bioactivity of phosphate-based glasses, J. Mater. Sci. 52 (2017) 9014–9022. doi:10.1007/s10853-017-1155-x.

[14] A. Oryan, M.B. Eslaminejad, A. Kamali, S. Hosseini, F.A. Sayahpour, H. Baharvand, Synergistic effect of strontium , bioactive glass and nano-hydroxyapatite promotes bone regeneration of critical-sized radial bone defects, (2018). doi:10.1002/jbm.b.34094.

[15] P.J. Marie, Strontium as therapy for osteoporosis, Curr. Opin. Pharmacol. 5 (2005) 633–636. doi:10.1016/j.coph.2005.05.005.

[16] H. Tripathi, C. Rath, A.S. Kumar, P.P. Manna, S.P. Singh, Structural, physico-mechanical and in-vitro bioactivity studies on SiO2–CaO–P2O5–SrO–Al2O3 bioactive glasses, Mater. Sci. Eng. C. 94 (2019) 279–290. doi:10.1016/j.msec.2018.09.041.

[17] H. Liu, R. Yang, Y. Wang, S. Liu, Influence of alumina additions on the physical and chemical properties of lithium-iron-phosphate glasses, Phys. Procedia. 48 (2013) 17–22. doi:10.1016/j.phpro.2013.07.004.

[18] A.C. Da Silva, Structure and percolation of bioglasses, in: Adv. Struct. Mater., Springer, Cham, 2016: pp. 49–84. doi:10.1007/978-3-319-44249-5_3.

[19] J. Du, Y. Xiang, Effect of strontium substitution on the structure , ionic diffusion and dynamic properties of 45S5 Bioactive glasses, 358 (2012) 1059–1071. doi:10.1016/j.jnoncrysol.2011.12.114.

[20] J.S. Moya, B. Cabal, J. Sanz, A.C. Da Silva, S.R. Mello-Castanho, R. Torrecillas, F. Rojo, Mechanism of calcium lixiviation in soda-lime glasses with a strong biocide activity, Mater. Lett. 70 (2012) 113–115. doi:10.1016/j.matlet.2011.11.104.

[21] L. Esteban-Tejeda, A.C. da Silva, S.R. Mello-Castanho, C. Pacharroman, J.S. Moya, Kinetics of dissolution of a biocide soda-lime glass powder containing silver nanoparticles, J. Nanoparticle Res. 15 (2013) 1447. doi:10.1007/s11051-013-1447-2.

[22] J.S. Moya, L. Esteban-Tejeda, C. Pecharromán, S.R.H. Mello-Castanho, A.C. da Silva, F. Malpartida, Glass Powders with a High Content of Calcium Oxide: A Step Towards a “Green” Universal Biocide, Adv. Eng. Mater. 13 (2011) B256–B260. doi:10.1002/adem.201080133.

[23] F. Baino, Bioactive glasses – When glass science and technology meet regenerative, Ceram. Int. 44 (2018) 14953–14966. doi:10.1016/j.ceramint.2018.05.180.

[24] D.S. Brauer, R. Brückner, M. Tylkowski, L. Hupa, Sodium-free mixed alkali bioactive glasses, in: Biomed. Glas., 2016: pp. 99–110. doi:10.1515/bglass-2016-0012.

[25] M. Tylkowski, D.S. Brauer, Mixed alkali effects in Bioglass ® 45S5, 376 (2013) 175–181. doi:10.1016/j.jnoncrysol.2013.05.039.

[26] D. Bellucci, V. Cannillo, A. Sola, An overview of the effects of thermal processing on bioactive glasses, Sci. Sinter. 42 (2010) 307–320. doi:10.2298/SOS1003307B.

[27] C. Volzone, F. Matías Stábile, Structural Changes by Thermal Treatment up to Glass Obtention of P 2 O 5-Na 2 O-CaO-SiO 2 Compounds with Bioglass Composition Types, New J. Glas. Ceram. 3 (2013) 53–57. doi:10.4236/njgc.2013.31009.

[28] L. Lefebvre, J. Chevalier, L. Gremillard, R. Zenati, G. Thollet, D. Bernache-Assolant, A. Govin, Structural transformations of bioactive glass 45S5 with thermal treatments, Acta Mater. 55 (2007) 3305–3313. doi:10.1016/j.actamat.2007.01.029.

[29] O. Peitl, E. Dutra Zanotto, L.L. Hench, Highly bioactive P2O5–Na2O–CaO–SiO2 glass-ceramics, J. Non. Cryst. Solids. 292 (2001) 115–126. doi:10.1016/s0022-3093(01)00822-5.

[30] J.K.M.F. Daguano, S.O. Rogero, M.C. Crovace, O. Peitl, K. Strecker, C. Dos Santos, Bioactivity and cytotoxicity of glass and glass-ceramics based on the 3CaO·P2O5-SiO2-MgO system, J. Mater. Sci. Mater. Med. 24 (2013) 2171–2180. doi:10.1007/s10856-013-4972-8.

[31] C. Lara, M.J. Pascual, A. Durán, Glass-forming ability, sinterability and thermal properties in the systems RO–BaO–SiO2 (R=Mg, Zn), J. Non. Cryst.

Solids. 348 (2004) 149–155. doi:10.1016/j.jnoncrysol.2004.08.140.

[32] S. Kapoor, D. Brazete, I.C. Pereira, G. Bhatia, M. Kaur, L.F. Santos, D. Banerjee, A. Goel, J.M.F. Ferreira, Impact of transition metal ions on the structure and bioactivity of alkali-free bioactive glasses, J. Non. Cryst. Solids. 506 (2019) 98–108. doi:10.1016/j.jnoncrysol.2018.12.003.

[33] X. Chen, X. Chen, D.S. Brauer, R.M. Wilson, R. V Law, R.G. Hill, N. Karpukhina, Sodium is not essential for high bioactivity of glasses, Int. J. Appl. Glas. Sci. 8 (2017) 428–437. doi:10.1111/ijag.12323.

[34] K. Fujikura, N. Karpukhina, T. Kasuga, D.S. Brauer, R.G. Hill, R. V. Law, Influence of strontium substitution on structure and crystallisation of Bioglass® 45S5, J. Mater. Chem. 22 (2012) 7395. doi:10.1039/c2jm14674f.

[35] D. Bellucci, V. Cannillo, A novel bioactive glass containing strontium and magnesium with ultra-high crystallization temperature, Mater. Lett. 213 (2018) 67–70. doi:10.1016/j.matlet.2017.11.020.

[36] R.K. Brow, Nature of Alumina in Phosphate Glass: I, Properties of Sodium Aluminophosphate Glass, J. Am. Ceram. Soc. 76 (1993) 913–918. doi:10.1111/j.1151-2916.1993.tb05315.x.

[37] S. Kapoor, Â. Semitela, A. Goel, Y. Xiang, J. Du, A.H. Lourenço, D.M. Sousa, P.L. Granja, J.M.F. Ferreira, Understanding the composition-structure-bioactivity relationships in diopside (CaO·MgO·2SiO2)-tricalcium phosphate (3CaO·P2O5) glass system, Acta Biomater. 15 (2015) 210–226. doi:10.1016/j.actbio.2015.01.001.

[38] H. Eckert, Structural characterization of bioactive glasses by solid state NMR, J. Sol-Gel Sci. Technol. 88 (2018) 263–295. doi:10.1007/s10971-018-4795-7.

[39] M. Edén, NMR studies of oxide-based glasses, Annu. Reports Sect. “C” (Physical Chem. 108 (2012) 177. doi:10.1039/c2pc90006h.

[40] R.A. Martin, H.L. Twyman, G.J. Rees, J.M. Smith, E.R. Barney, M.E. Smith, V. Hanna, R.J. Newport, A structural investigation of the alkali metal site distribution within bioactive glass using neutron diffraction and multinuclear solid state NMR, (2012) 12105–12113. doi:10.1039/c2cp41725a.

[41] R.K. Brow, R.J. Kirkpatrick, G.L. Turner, Nature of Alumina in Phosphate Glass: II, Structure of Sodium Alurninophosphate Glass, J. Am. Ceram. Soc. 76 (1993) 919–928. doi:10.1111/j.1151-2916.1993.tb05316.x.

[42] M.D. O ’donnell, S.J. Watts, R. V Law, R.G. Hill, Effect of P 2 O 5 content in two series of soda lime phosphosilicate glasses on structure and properties – Part II: Physical properties, (2008). doi:10.1016/j.jnoncrysol.2008.03.035.

[43] R.K. Brow, Review: the structure of simple phosphate glasses, J. Non. Cryst. Solids. 263–264 (2000) 1–28. doi:10.1016/S0022-3093(99)00620-1.

[44] B.O. Mysen, F.J. Ryerson, D. Virgo, The structural role of phosphorus in silicate melts, Am. Mineral. 66 (1981) 106–117.

[45] A. Tilocca, A.N. Cormack, Structural Effects of Phosphorus Inclusion in

Bioactive Silicate Glasses, (2007). doi:10.1021/jp075677o.

[46] Y. Xiang, J. Du, Effect of strontium substitution on the structure of 45S5 bioglasses, Chem. Mater. 23 (2011) 2703–2717. doi:10.1021/cm102889q.

[47] J.K. Christie, R.I. Ainsworth, N.H. de Leeuw, Investigating structural features which control the dissolution of bioactive phosphate glasses: Beyond the network connectivity, J. Non. Cryst. Solids. 432 (2016) 31–34. doi:10.1016/j.jnoncrysol.2015.01.016.

CHAPTER 2: Glass dissolution mechanism

2.1 Background

Much has been said about the interaction of bioactive glasses as the tissue of the host organism and the benefits in bone tissue growth resulting from this interaction [1–3]. However, this only runs because these glasses are susceptible to chemical reactions with body fluids, which results in dissolution originated in the implant surface, a process recognized for releasing species such as phosphate and calcium ions that lead to the formation of interfacial hydroxyapatite between the implant and the living host tissue [4].

It is a common mistake to easily consider that the way a bioactive glass is metabolized i.e., dissolved in the corporeal environment is directly a consequence of its composition, it would be more correct to consider that each composition induces a particular and restricted variation of the structural arrangement of the material. Thus, it can also vary within this package according to its thermal history during processing, and consequently the same composition can have different dissolution rates [5]. This is so true that the glass itself is a result of a thermal history where there is a super cooling, otherwise a non-glassy crystalline structure would form. So, it can be assumed that composition and durability are not a strict law [6].

The thermal historic is what will determine the arrangement of the structures of one or more precursor liquid of segregated or dissolved glass in each other, the arrangements between the chains and most importantly, the interfaces between liquids or spaces inside chains which ultimately will be the facilitators of the percolation phenomena in the vitreous network and govern the process of dissolution and formation of hydroxyapatite on the surface.

When we think of an implant, we immediately associate its interaction with the host and body fluids, which is true, however the mechanisms of dissolution of the glass chain and ionic transport involved are strictly similar to those that occur in simple aqueous media therefore one important step to understand glass behavior whether the application, is to understand interactions with water[4].

In this Chapter, we report the mechanistic insights of the alteration in aqueous media by the qualitative study and comparison of a novel composition to other glass compositions.

2.2 Experimental procedure

2.2.1 Sample preparation

The glasses were prepared from the stablished compositions and procedure presented in Chapter 1 (Section 1.2).

2.2.2 Static dissolution experiments

Dissolution experiments were conducted in Teflon reactors at 90 ° C for 14 days. Three specimens of each composition with dimensions of (1 × 10 × 10) mm^3 were tested [7]. A low solid-to-solution mass ration condition of 0.02 was maintained. All samples were evaluated at fixed times of 0, 1, 3, 7 and 14 days. At the end of each time the weight variations of the samples were measured by use of an analytical precision balance (±0.00005 g) as well as the pH and salinity (Oakton™, PC700) of the leached solution. The hydrolytic resistance of the obtained glasses was evaluated considering the weight loss of started bulk samples over time.

Raman spectroscopy was used to study the structural alterations of the glass surface over hydrolytic resistance test. The µ-Raman spectroscopy analysis was performed with a WITEC Confocal Raman Microscope Alpha300 R spectrometer. The samples were excited by the 532 nm line of an Ar^+ laser and recorded with microscope objective 50x/0.7 at 60s integration time with 45 mW power.

Scanning electron microscopy (SEM) was used to illustrate the surface of samples after the 14 days of static dissolution test. The images were obtained by using a Hitachi TM2300 at 15 kV of accelerating voltage was used for surface morphology evaluation of the samples after dissolution test and bioactivity. Their chemical composition was examined with an energy-dispersive X-ray spectrometer

(EDX: EMAX-7000, Horiba Ltd., Kyoto, Japan) by using 9 kV-K that penetrate approximately 1 μm in depth.

2.2.3 Dynamic dissolution experiments

Due to the difficult to collect powder samples during the test, a dynamic test were conducted based on the method adapted by Silva [8]. The samples were encapsulated within a microtube containing filter paper and four slots and were continually washed with distillated water in a cyclic distillation process at 90 ° C. After each fixed time of 0, 1, 3, 7 and 14 days Fourier Transform Infrared (FT-IR) spectroscopy was used to study the chemical alteration of the glass surface during the test. The analyses were performed by using a Bruker IFS 66 VS Spectrometer in transmission mode within a range of 400 to 4000 cm^{-1} and a resolution of 2 cm^{-1}. The samples were mixed with KBr.

2.3 Results and Discussions

2.3.1 Interaction mechanisms between aqueous media and glasses

The interaction mechanism of glasses and aqueous medium is a very complex process and is still a matter of debate. Notwithstanding, it is a consensus that among several simultaneous processes involved, the interaction between the media and the glass surface occasion three well-defined steps that is leaching, dissolution and precipitation [9]. Still, in a general way we can assume that glass alteration occurs as represented in Figure 2.1.

Figure 2.1. Schematic summary of the stages of glass alteration behavior. (I) Leaching. (T) Transitional. (II) Precipitation and (III) Corrosion.

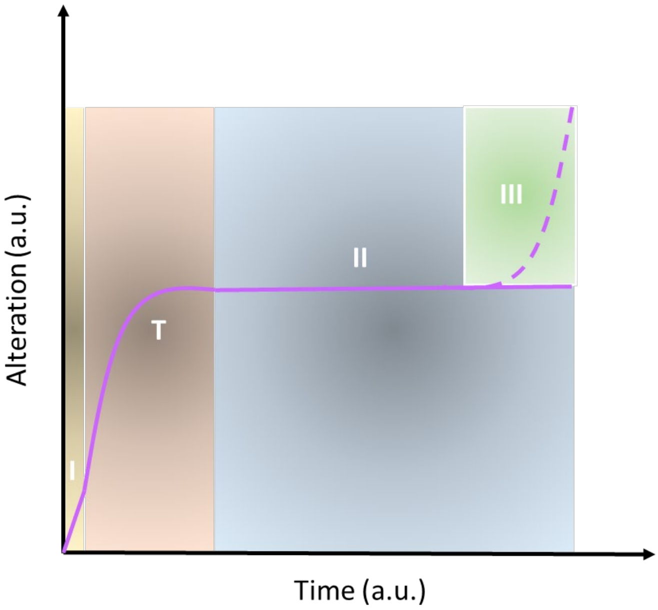

Source: the author.

The leaching stage identified as I in the figure is the first and quickly process which results in an outset alteration. After leaching there is a transitional stage T, when expressive changes can be noticed as a consequence of the dissolution of the glass and its interaction with a medium containing many ionic species. Stage II, the interaction with a supersaturated environment combine to result in a slow rate to layers formation by precipitation of leached species from the aqueous medium. Stage III is the occasionally observed tendency for accelerated aqueous corrosion after extensive time spent at low reaction (Stage II) and there is not the focus of this work [10].

Initially, the surface in contact with a fresh solution alters rapidly leaching out species by the exchange between the solution protons (H^+ and H_3O^+) and glass network terminal modifiers (alkali or Na^+ in this case) as shown by the following schematic reactions (1) and (2). This step is controlled by diffusion [10,11].

$$\equiv Si-O^-Na^+{}_{(glass)} + H_2O_{(aq)} \rightarrow \equiv Si-OH_{(hydrated\ glass)} + Na^+_{(aq)} + OH^-_{(aq)} \qquad (1)$$

$$\equiv Si-O-Si\equiv_{(glass)} + H_2O_{(aq)} \leftrightarrow 2\ \equiv Si-OH_{(hydrated\ glass)} \qquad (2)$$

The first reaction deeply affects pH and the second contributes to the break of Si-O bonds throughout the network, creating silanol groups (SiOH). By the action of hydroxyl (OH^-) ions the dissolution, i.e., disruption of the network starts. The dissolution occurs by the migration of soluble silica in the form of silicic acid [$Si(OH)_4$] as shown in the following schematic reaction (3). This process is dictated by interfacial reaction [12].

$$\equiv Si{-}O{-}Si(OH)_{3(\text{hydrated glass})} + OH^-_{(aq)} \rightarrow \equiv Si{-}O^-_{(\text{hydrated glass})} + Si(OH)_{4(aq)} \quad (3)$$

With increasing concentration of silicic acid in solution, silica repolymerizes, forming dimers and oligomers [13]. When the solution is already supersaturated, the dimers and oligomers condensates into a silica rich layer on the surface sites depleted in alkalis [14]. Silicate glasses can also repolymerize themselves and forming Si−O−Si bonds by the reverse of the schematic reaction (2). Alkaline solutions ($pH > 9.0$) and increasing salinity, can trigger formation of silica gel layer by the aggregation of silica particles [14]. In fact, pH has proved to be a more determinant factor for the glass dissolution process than composition itself. As the reaction proceeds, the dissolution continues to occur but in a slower rate due to the transport-limiting gel layer formed at the surface. Between the gel layer and the unreacted glass surface there is a leached layer which contributes to a path of percolation transport of solute species such as Ca^{2+} and PO_4^{3-}.

2.3.2 Static dissolution

The dissolution rate, cumulative weight loss, pH and salinity are shown in Figure 2.2.

Figure 2.2. a) Dissolution rate ($[g/cm^2 \times s] \times 10^{-7}$), cumulative weight loss, pH and salinity in function of time (days) during the dissolution test.

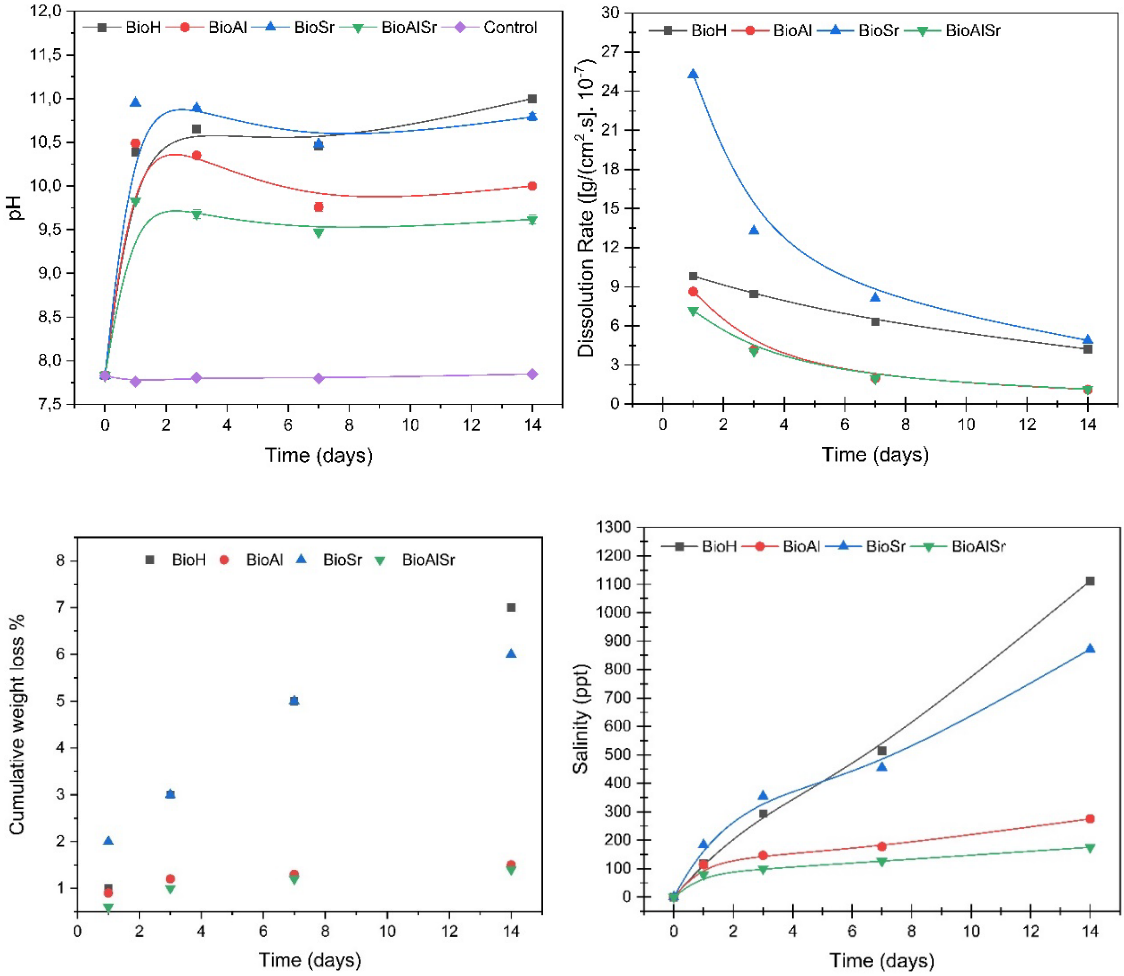

Source: the author.

In Figure 2.2a it can be observed that after one day of immersion all glasses showed the typical pH rise as a result of the initial stage (leaching), when there are exchanging of the alkali ions by hydrogen (H_3O^+). However, difference in maxima can be noticed. BioSr presented the highest pH ~11, in agreement with works which have reported an increase of pH values in SBF and TRIS solutions when in contact with strontium-cointaining glasses [15]. BioAlSr in contrast exhibited a decrease in maxima ~ 9.75 and BioH and BioAl presented similar pH ~10.5.

Figure 2.3 shows the ^{29}Si MAS-NMR spectra of all four samples before immersion in aqueous media.

Figure 2.3. ^{29}Si MAS-NMR spectra for all glasses.

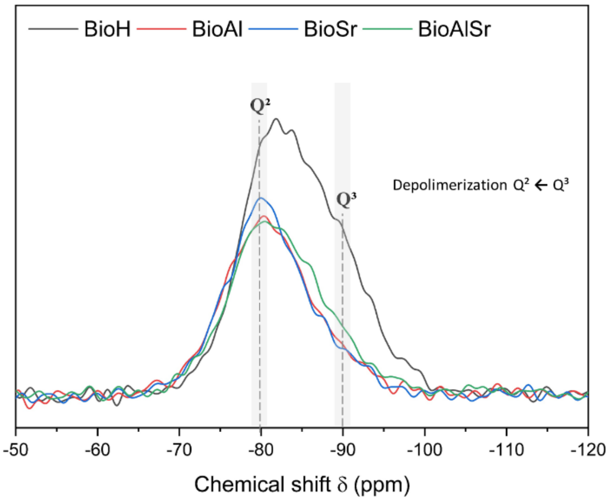

Source: the author.

The spectra indicated that all substituted glasses (BioAl, BioSr and BioAlSr) undergo a network depolymerization, i.e. a significant contribution of Q_{Si}^3 units present at BioH (45S5) was converted in Q_{Si}^2 units resulting in less complex structures. So, it was expected that an open glass network would impart in an easier exchanging of the alkali with the media but under the conditions tested (90 °C) that did not take place. It seems that this exchange was slower for BioAlSr even with similar Q_{Si}^n distribution. After 3 days of immersion all samples showed a similar behavior with a slight decrease in pH. After the 7th day the same behavior was observed. However, after the 14th day the upward trend occurs for all compositions and remarkably for BioH samples, which ranged from 10.46 to 11.00. The results founded contributes to the speculation that dissolution is not necessarily compositional and structural dependent.

The dissolution rate is given by mass loss as a function of the surface area of the bulk samples. The hydrolytic resistance obtained and presented in Figure 2.2b indicates a monotonic decrease as a function of time for all samples. Also, BioSr presented the highest dissolution rate since the beginning of the test.

Although all glasses presented the same trend reducing the dissolution rate over time, the cumulative weight loss in function of time, in Figure 2.2c, pointed out a different behavior.

As the test proceeds BioAl and BioAlSr have maintained their weight loss stabilized but BioH and BioSr both presented similar and constant weight loss over the time. In addition, it can be observed in Figure 2.2d where it is presented the salinity measurement in function of time that salinity values have increased practically linear for BioH and BioSr and was constant for BioAl and BioAlSr. As already mentioned above, alkaline medium and increasing salinity is a key factor to trigger silica gel layer formation and depolymerization of silica network. It seems that the higher the pH the superior the alteration and/or attack of the surface [16]. With great alterations and intense reactions through the percolation channels, it is likely that the leached layer be weakened and that the silica layer could detach completely from the surface. Resulting in an exposure of a fresh surface to restart the dissolution process. However, this process will not restart from the beginning once the solution is already supersaturated and the surface exposed is the leached surface; we cannot currently confirm it, however, this phenomenon was observed with the naked eye.

The SEM images captured after 14 days of static dissolution test are presented in figure 2.4.

Figure 2.4. Appearance of glass surface after 14 days of static dissolution a) BioH; b) BioAl; c) BioSr; d) BioAlSr.

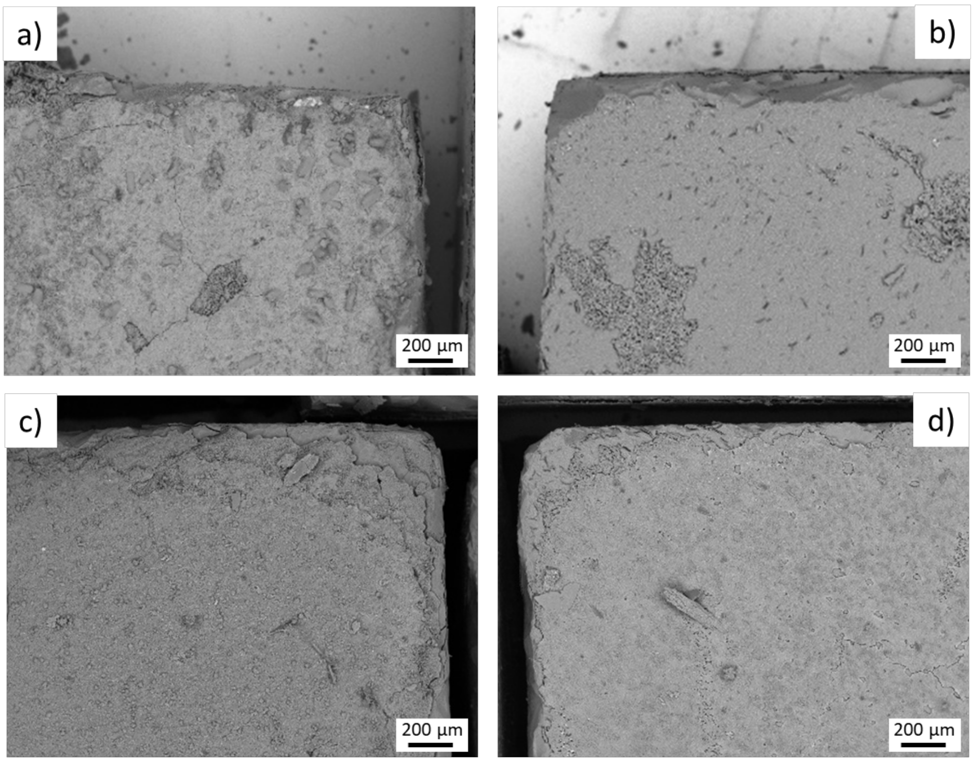

Source: the author.

As expected the samples with the lowest dissolution rates, BioAl and BioAlSr, presented less damaged surface. In BioH and BioSr images in contrast the result of an intense dissolution can be noticed by the different depth of the alteration layers near the edges. Even tough there is indication of dissolution in BioAl and BioAlSr the obtained results gave a clear difference between the samples indicating their better stability.

Local surface differences were found and observed by SEM and EDS analysis, the intensity was set at 1 cps/eV for comparative purpose, the images are presented in figure 2.5.

Figure 2.5. SEM/EDS micrographs of monolytic samples after 14 days of static dissolution test a) BioH; b) BioAl; c) BioSr; d) BioAlSr.

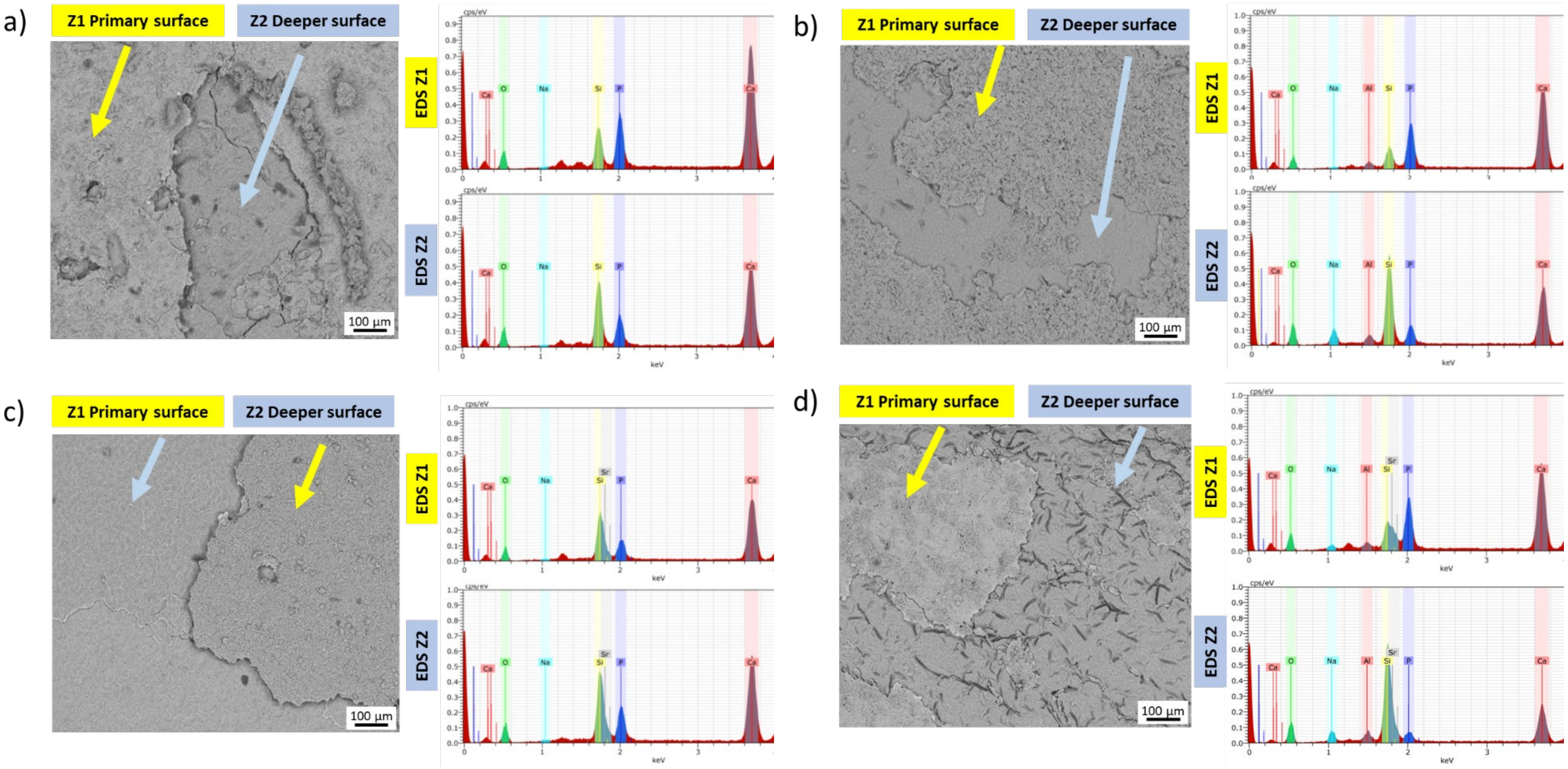

Source: the author.

In a general way was identified a pattern, a primary calcium-phosphorous-rich surface and a deeper silicon-rich layer. Still some differences can be observed and pointed as follows. The sodium presence in BioH and BioSr for both primary and deeper surface was practically null. In BioAl and BioAlSr instead a little intensity was observed in the deeper surface. This is in agreement with dissolution parameters founded, as BioAl and BioAlSr have significant lower rates so the deeper surface is still under leaching process, BioSr and BioH in contrast, with higher rates even the deeper surface has been leached.

An interesting aspect can be seen in BioSr spectra. The presence of phosphate is the inverse of the observed for all samples. Higher intensity for phosphorous, calcium, silicon and strontium is observed in the deeper surface, as already suggested by other authors and exposed in our previous work [17,18] there are evidences that strontium in this composition is segregated, possibly clustering with phosphorous. Considering this assumption segregating parts although not reducing dissolution rate could be affecting dissolution mechanism.

Raman spectroscopy was conducted to acquire structural information of the samples after dissolution test. The collected spectra is presented in figure 2.6 and the spectra of samples before the test can be observed inset.

Figure 2.6. Raman spectra collected from a) BioH; b) BioAl; c) BioSr; d) BioAlSr after 14 days of static dissolution test.

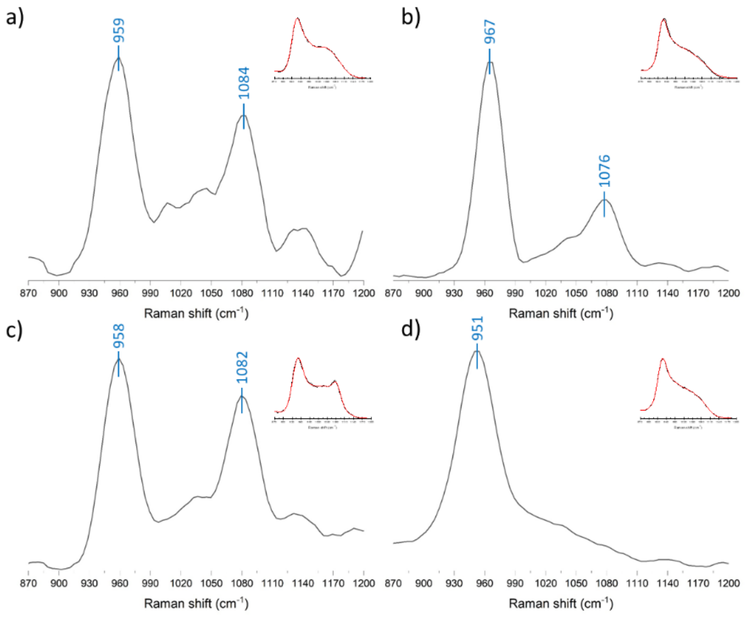

Source: the author.

By considering the depolymerization of the network caused by the hydrolytic attack the region between 900 and 1200 cm^{-1} was observed. The principal units present in all samples are Q^2 and Q^3 located at ~ 944 and 1086 cm^{-1} respectively. There is also a great contribution of the stretching bridgen oxygens (BO) in all Q species at 1044 cm^{-1}. All samples were considerable affected by the hydrolitic atack, a expressive change in BO and Q^3 contribution was observed. BioH and BioSr had a loss in BO contribution and an intensification of Q^3 units, evidencing a possible repolymerization of the network from the formation of Si−O−Si bonds by the reverse of the schematic reaction (2) section 2.3.1 BioAl presented the similar trend but with less intense Q^3 contribution. Unlike previous samples BioAlSr did not present a significant contribution of Q^3 units, indicating an intense depolymerization of the network.

2.3.3 Dynamic dissolution

The FTIR spectra of glass samples BioH, BioAl, BioSr and BioAlSr over the dynamic hydrolytic resistance test are shown in Figure 2.7 where graph A corresponds to samples before the beginning of the test and graph B, C and D to 1, 7 and 14 days after test respectively. Besides the advantage of evaluate powder samples each time, the dynamic, i.e. continuous experiment, impedes the build-up of ions released from the glasses so the changes can be observed more clearly.

Figure 2.7. Transmittance FT-IR spectra of samples before and after 1, 7 and 14 days of hidrolytic atack.

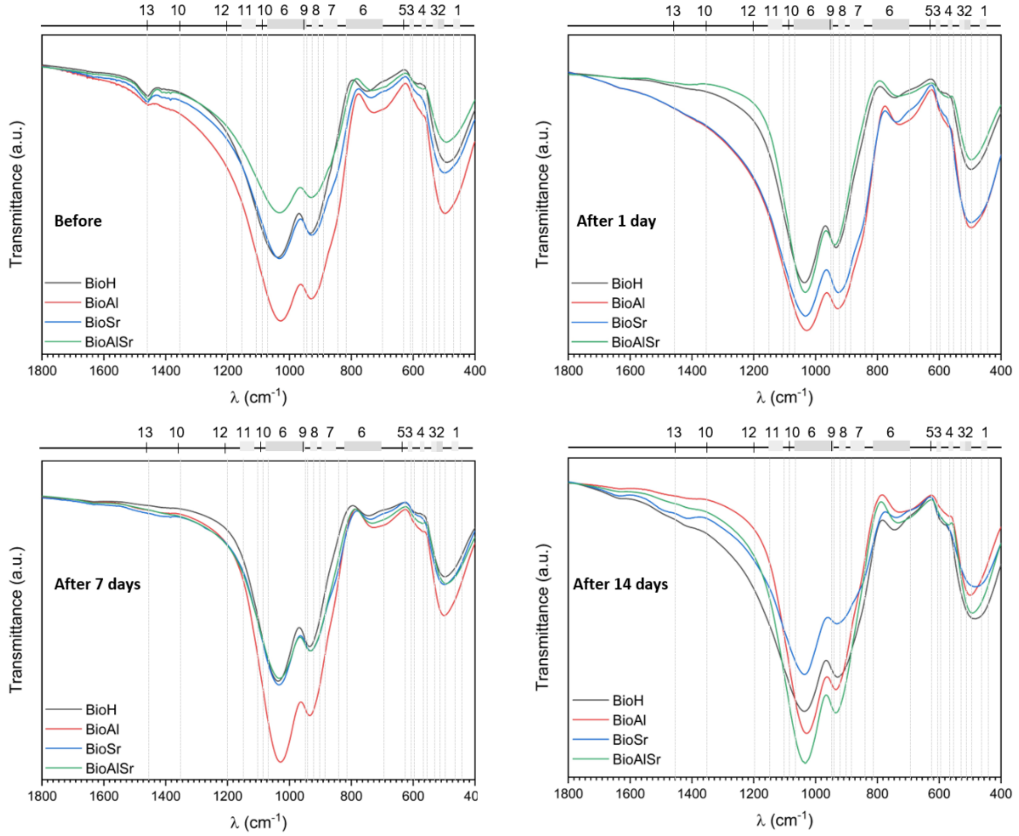

Source: the author.

The spectra indicate usual soda-lime glass structure associated with functional groups related to phosphorous bonds, peaks and bands indicated in the figure as following: 1 as Si-O,[Q^4] between 440 and 460 cm^{-1} and at 1200 cm^{-1}; 2 as bands of segregated metal oxides between 480 and 520 cm; 3 as crystalline P-O between 500 and 520 cm^{-1}; 4 as vitreous P-O between 540 and 555 cm^{-1}; 5 as OH hydroxyapatite at 630 cm^{-1}; 6 as metal silicates formation between 700 and 820 cm^{-1} and between 960 and 1050 cm^{-1}; 7 as Si-O [NB],[Q^0] between 850 and 880 cm^{-1}; 8 as Si-O[NB][Q^1] between 900 and 920 cm^{-1}; 9 as Si-O[NB],[Q^2] at 950 cm^{-1}; 10 as P=O 1080 cm^{-1}; 11 as Si-O[NB], [Q^3] between 1100 and 1150 cm^{-1}); 12 as Si-O, [Q^4] at 1200 cm^{-1}; 13 as Na-O at 1470 cm^{-1}).

From graph A it can be observed the presence of alkaline metal in glassy structure by indicating link peak Na-O (10), expressing that the charges are being balanced by ion attraction, these peaks are not sharp but diffuse and wide, which indicates different situations of charge balancing by Na$^+$. After 1 day under test conditions, the first thing that can be noticed is that this peak disappear. It is related with Na^+ as an alkali cation being the first to react and exchange with the surrounding medium. As the test runs, graphs C and D, the band at around 1025 cm^{-1} narrows and changes at 1400 cm^{-1} can be observed. A continuous formation of Q^3 (11) is evident throughout the process. A intensification of Si-O[NB], [Q^2] at 950 cm^{-1} is also noticed for BioAl and BioAlSr. There is a depolymerization of Q^1 to Q^0 for all samples during the test, observed 8 and 7 respectively.

The P=O band at 10 did not demonstrate clear interaction with the vitreous network. Still, at 700 cm^{-1} in metal silicates formation region (6) changes can be noticed that could be associated with the interaction between phosphorous or calcium with the other metals such as aluminum and strontium.

The SEM images of glass particles at 0, 1, 7 and 14 days of test is presented in figure 2.8.

Figure 2.8. Appearance of glass particles before and after 1, 7 and 14 days of hidrolytic atack.

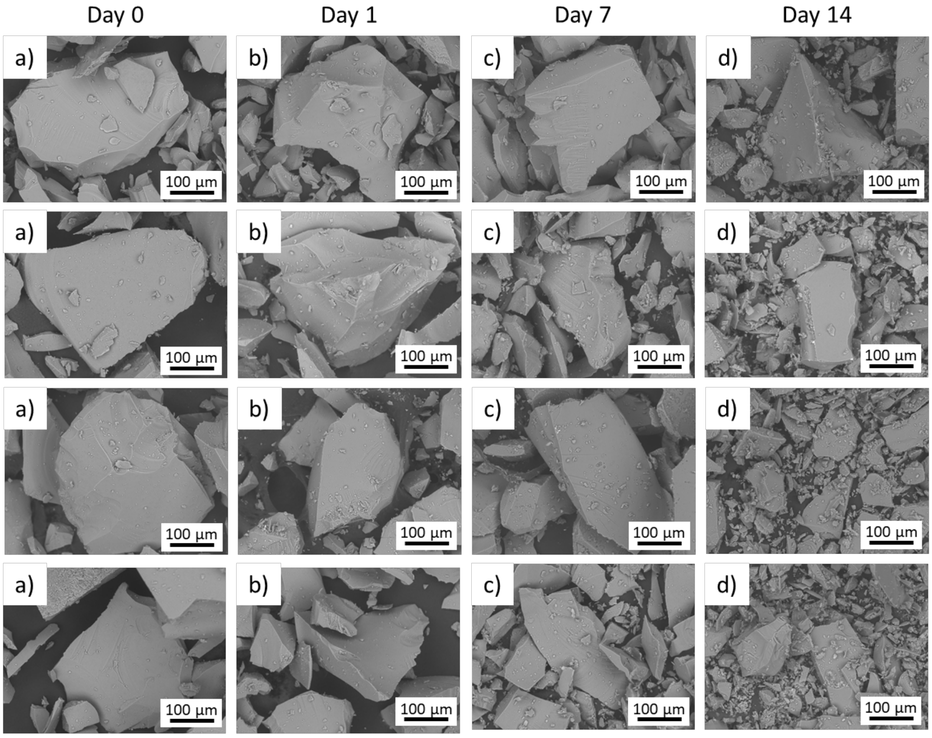

Source: the author.

The dynamic experiment did not result in noticeable corrosion for all samples, the sharp corners and edges of fragile fracture of glasses was maintained even after 14 days. Also, none evidence of a layer formation was observed. Otherwise, as the test proceeds accumulation of smaller particles is observed, possibly leached product which were not able to precipitates into the particles surface due to the continuous flow.

2.4 Chapter 2 Conclusions

In Chapter, glass durability was evaluated by static and dynamic dissolution experiments. From the results, it can be indicated that the addition of two new metals in the composition possibly facilitates the formation of a secondary phase formed because of two liquids immiscibility. The structural reorganization confirmed by 29Si MAS-NMR could contribute to the creation of an interface between the two phases favoring the ionic transport, mainlly of sodium, calcium and phosphorous. From dynamic dissolution experiment no noticeable corrosion or layer formation was observed. Static dissolution experiments indicated a great change in pH comparing the samples as the test proceed. Significant alterations were observed for BioH and BioSr which presented the highest values of pH and, consequently of dissolution rate as well. It can be assumed that for all samples instead of structure factors the maintenance of pH in alkaline level deeply influenced the dissolution under the conditions tested. The samples BioAl and BioAlSr with pH between 9,5 and 10,5 presented a cumulative weght loss below 2 % after 14 days. On the contrary, BioH and BioSr with pH superior to 10,5 during all the test, pointed weight loss of 6% and 7% respectively.

REFERENCES

[1] A. Oryan, M.B. Eslaminejad, A. Kamali, S. Hosseini, F.A. Sayahpour, H. Baharvand, Synergistic effect of strontium , bioactive glass and nano-hydroxyapatite promotes bone regeneration of critical-sized radial bone defects, (2018). doi:10.1002/jbm.b.34094.

[2] F.E. Ciraldo, E. Boccardi, V. Melli, F. Westhauser, A.R. Boccaccini, Tackling bioactive glass excessive in vitro bioreactivity: Preconditioning approaches for cell culture tests, Acta Biomater. (2018). doi:10.1016/j.actbio.2018.05.019.

[3] S. Kargozar, S. Hamzehlou, F. Baino, Can bioactive glasses be useful to accelerate the healing of epithelial tissues?, Mater. Sci. Eng. C. 97 (2019) 1009–1020. doi:10.1016/J.MSEC.2019.01.028.

[4] L.L. Hench, N. Roki, M.B. Fenn, Bioactive glasses: Importance of structure and properties in bone regeneration, (2014). doi:10.1016/j.molstruc.2014.03.066.

[5] F. Baino, M. Marshall, N. Kirk, C. Vitale-Brovarone, Design, selection and characterization of novel glasses and glass-ceramics for use in prosthetic applications, Ceram. Int. 42 (2016) 1482–1491. doi:10.1016/j.ceramint.2015.09.094.

[6] A. Tilocca, Structural models of bioactive glasses from molecular dynamics simulations, (n.d.). doi:10.1098/rspa.2008.0462.

[7] D.E. Day, Z. Wu, C.S. Ray, P. Hrma, Chemically durable iron phosphate glass wasteforms, J. Non. Cryst. Solids. 241 (1998) 1–12. doi:10.1016/S0022-3093(98)00759-5.

[8] A.C. Silva, S.R.H. Mello-Castanho, Vitrified galvanic waste chemical stability, J. Eur. Ceram. Soc. 27 (2007) 565–570. doi:10.1016/j.jeurceramsoc.2006.04.110.

[9] A.C. Da Silva, Structure and percolation of bioglasses, in: Adv. Struct. Mater., Springer, Cham, 2016: pp. 49–84. doi:10.1007/978-3-319-44249-5_3.

[10] B. Parruzot, J. V. Ryan, J.L. George, R.K. Motkuri, J.F. Bonnett, L.M. Seymour, M.A. Derewinski, Multi-glass investigation of Stage III glass dissolution behavior from 22 to 90 °C triggered by the addition of zeolite phases, J. Nucl. Mater. 523 (2019) 490–501. doi:10.1016/j.jnucmat.2019.05.050.

[11] J.D. Vienna, J. V. Ryan, S. Gin, Y. Inagaki, Current Understanding and Remaining Challenges in Modeling Long-Term Degradation of Borosilicate Nuclear Waste Glasses, Int. J. Appl. Glas. Sci. 4 (2013) 283–294. doi:10.1111/ijag.12050.

[12] S. Gin, L. Neill, M. Fournier, P. Frugier, T. Ducasse, M. Tribet, A. Abdelouas, B. Parruzot, J. Neeway, N. Wall, The controversial role of inter-diffusion in glass alteration, Chem. Geol. 440 (2016) 115–123. doi:10.1016/j.chemgeo.2016.07.014.

[13] D.J. Belton, O. Deschaume, C.C. Perry, An overview of the fundamentals of the chemistry of silica with relevance to biosilicification and technological advances, FEBS J. 279 (2012) 1710–1720. doi:10.1111/j.1742-4658.2012.08531.x.

[14] T. Geisler, T. Nagel, M.R. Kilburn, A. Janssen, J.P. Icenhower, R.O.C. Fonseca, M. Grange, A.A. Nemchin, The mechanism of borosilicate glass corrosion revisited, Geochim. Cosmochim. Acta. 158 (2015) 112–129. doi:10.1016/j.gca.2015.02.039.

[15] Y.C. Fredholm, N. Karpukhina, D.S. Brauer, J.R. Jones, R. V Law, R.G. Hill, Influence of strontium for calcium substitution in bioactive glasses on degradation, ion release and apatite formation, J. R. Soc. Interface. 9 (2012) 880–889. doi:10.1098/rsif.2011.0387.

[16] M. Tylkowski, L. Hupa, D.S. Brauer, Controlling the ion release from mixed alkali bioactive glasses by varying modifier ionic radii and molar volume, (2016) 3121–3134. doi:10.1039/c5tb02426a.

[17] M.S. Araujo, J.F. Bartolomé, S. Mello-Castanho, Tribological and mechanical behaviour of 45S5 Bioglass®-based compositions containing alumina and strontium, Ceram. Int. 46 (2020) 24347–24354. doi:10.1016/j.ceramint.2020.06.216.

[18] M.S. Araujo, A.C. Silva, J.F. Bartolomé, S. Mello-Castanho, Structural and thermal behavior of 45S5 Bioglass ® -based compositions containing alumina and strontium, J. Am. Ceram. Soc. 103 (2020) 3620–3630. doi:10.1111/jace.17061.

CHAPTER 3: In vitro bioactivity and antibacterial capacity

3.1 Background

45S5 Bioglass®, apart from being the first material to bond to bone, is still by far one of most widely investigated materials for its efficiency in the repair of damaged bone tissues [1]. However, cases that require implantation or bone grafting are of a vastly different nature, and thus, it has become clear that a single solution cannot efficiently attend to all medical cases encountered [2,3]. That is, each case is influenced by factors such as the patient's age and metabolism, severity and extent of the bone defect, and initial mechanical load [4,5].

Taking this into account, changes in 45S5 composition have been considered to achieve desired effects for intended applications. Indeed, the ability to modify and add elements in glass networks is helpful to tailor properties and adjust requirements [6–8]. The challenge is to achieve an optimum balance between biocompatibility and other physicochemical properties.

We have recently shown that the addition of low amounts of alumina and strontium in a 45S5 composition outperformed some well-known drawbacks of 45S5, such as a poor processing window and a high tendency to crystallize, apart from significantly enhancing mechanical and tribological properties [9,10].

Among various elements that could promote such adjustments, strontium is one of the elements well known for being a bone-seeking element and a common substitute for calcium in glass composition in addition to improving osteoblast activity and inhibiting osteoclast function, minimizing the fracture of bone [11,12]. Recent studies have indicated that small amounts of strontium (2.5 mol%) exhibit bacteriostatic behavior against *Staphylococcus aureus (S. aureus)* [13]. Inhibitory effects on *Escherichia coli (E. coli)* and *Porphyromonas gingivalis (P. gingivalis)* were also reported [14]. Aluminum has a significant effect on improving the mechanical properties of bioglass, despite affecting its material solubility and, consequently, its bioactivity [11,12]. However, in adequate quantities, the solubility can be adjusted to acceptable limits, allowing the hydroxyapatite layer to last for longer periods and still be capable of bonding to bone while increasing the mechanical properties [15].

The effect of both elements on bioactivity has not been investigated thus far, and slight differences can lead to completely different biological responses. Here, we focused on evaluating the effects of each ion (Sr and Al) to better understand their combined effect. We performed powder and monolithic in vitro bioactivity analysis followed by infrared spectroscopy and X-ray diffraction to show the changes in apatite formation of each sample. The aims of this Chapter were to investigate the effect of this compositional modification of 45S5 Bioglass® on bioactivity and its antibacterial capacity against *E. coli*.

3.2 Experimental procedure

3.2.1 Sample preparation

The glasses were prepared from the stablished compositions and procedure presented in Chapter 1 (Section 1.2).

3.2.2 In vitro bioactivity analysis

The SBF solution was prepared following the Kokubo protocol [11]. After the solution was prepared, in vitro tests were performed on powder samples. The tests were conducted in a polyethylene container in which the powder samples with a particle size < 50 µm were dispersed in SBF solution at a ratio of 75 mg of glass to 50 ml of solution. The tests were performed in triplicate, and the solutions were agitated at a rate of 60 rpm and maintained at 37 °C for 480 min (8 h). The pH of the SBF solution was verified using a digital pH meter (Oakton™, PC700) after immersion of samples for different periods (0, 5, 15, 30, 60, 120, 240 and 480 min). Then, after the total period of immersion (8 h), the powders were filtered through quantitative filter paper (3 µ, Nalgon), rinsed immediately with Milli-Q water and acetone to stop any further reaction and dried at 50 °C for 2 h. Fourier transform infrared spectrometry was performed by using a spectrometer (Bruker IFS 66 VS) with diffuse reflectance attachment within a range of 400 to 1600 cm^{-1} and a resolution of 2 cm^{-1}.

The same SBF solution was used for monolithic pieces. The samples were soaked in SBF in a water bath at 37 °C with agitation for up to 14 days. The ratio of the sample surface area to SBF solution volume was 0.1 $cm^2 \cdot mL^{-1}$, and the solution was replaced every two days. After immersion for 7 and 14 days, the samples were rinsed immediately with Milli-Q water and acetone to stop any further reaction and dried at 50 °C for 2 h. Posteriorly, the sample surfaces were characterized by X-ray diffraction (XRD) for phase identification by using a Bruker D8 ADVANCE diffractometer using CuKα radiation with 2θ from 10 to 70° and a step of 0.1°/s.

3.2.3 SEM-EDS

Dissolution experiments were conducted based on the method adapted by Silva [17] employing a Soxhlet distillation column. Powders with a particle size < 50 µm of each composition were encapsulated within a microtube containing filter paper and four slots. The samples were continually washed with distilled water in a cyclic distillation process at 90 °C. Periods of, 1, 3, 7 and 14 days were evaluated. At the end of each step, the powders were filtered, rinsed with acetone, dried at 50 °C for 2 h and weighed using an analytical precision balance (±0.00005 g).

3.2.4 Dynamic dissolution

Tokyo, Japan) at an accelerating voltage of 15 kV was used to evaluate the surface morphology of the samples after the bioactivity study. The chemical composition of the surface was examined with an energy-dispersive X-ray spectrometer (EDS: EMAX-7000, Horiba Ltd., Kyoto, Japan) by using 9 kV-K that penetrates approximately 1 µm in depth.

3.2.5 Minimum Inhibitory Concentration (MIC) Determination

A twofold broth dilution method was used for minimum inhibitory concentration (MIC) and minimum bactericidal concentration (MBC) determination. Twofold serial dilutions of the powder samples (concentration ranging from 1 mg·mL-1 to 16 mg mL-1) were prepared in tubes containing nutrient broth medium and an inoculum of E. coli (2.11 × 105 CFU mL-1). A negative control containing only the cell inoculum in the growth medium was also prepared. After incubation for 24 h at 37 °C, bacterial growth was assessed by serial dilution plating. Nondirect determination of cell growth, such as culture turbidity, was used to determine the

MIC. There is potential optical interference due to the light-scattering properties of the powdered glass. Consequently, the bacteriostatic effect of these samples was determined by performing a viable count after exposure of the bacteria to samples for a fixed time of 24 h.

3.2.6 Cytotoxicity assay

An in vitro test of cytotoxicity was performed using bulk samples according to ISO 10993-Part 5 by the neutral red uptake methodology employing the cell line NCTC clone 929 from American Type Culture Collection (ATCC) [18,19]. The test was conducted in triplicate, and for the positive and negative controls, a 0.02% phenol solution and alumina were used, respectively. The cytotoxicity potential of the samples is presented as a cytotoxicity index (IC50 (%)). This is the concentration of the extract that injures or kills 50% of the cell population in the assay due to toxic elements extracted from the sample. The complete assay was described by C. Santos et al.[20].

3.3 Results and Discussion

3.3.1 In vitro bioactivity: powder samples

As already discussed in Chapter 1, these samples are formed by an open silicate network interconnected mostly in a combination of QSi^2 units, chains and rings. These associate with metastable materials, for which, in any liquid medium, the structure tends to seek and capture ionic species from the medium to constitute stable hydrated phases [21].

Carbonated hydroxyapatite formation is a prerequisite for glass bonds to bone/tissue. Its formation is a consequence of the dissolution process and generally follows the steps of usual alteration, that is, leaching, dissolution and precipitation [22]. The difference is that this process occurs at ~37 °C (body temperature), and the aqueous medium is the body fluid. After leaching, transition and precipitation of a silica-rich layer, a calcium-phosphate-rich layer is formed on top of it. This phase initially is amorphous and later crystallizes to a hydroxycarbonate apatite (HCA). When there are other ions present in glass, such as Sr2+ and Al3+, the interaction between phosphate and the alkaline matrix can shift, resulting in related crystalline compounds. However, there is tolerance of the amount that can be substituted in the crystal lattice without compromising its structure [23,24].

The formation of HCA layers on glass particles was studied in simulated body fluid solution obtained according to the Kokubo protocol [16] and tested under Fredholm-[25] adapted conditions for high bioactive powder samples as described in section 2.2.

The formation of an HCA layer occurs while the silica characteristic bands decrease [26]. Figure 3.1 presents the FTIR spectra of the powder glass samples as obtained. The spectra of samples before immersion exhibited a usual disordered feature, indicating a band at 940 cm^{-1} assigned to the structure QSi² (Si-O(2NBO) and bands at ~ 1030 cm^{-1} and at 490 cm^{-1} associated with stretching and bending of QSi³ units (Si-O-Si), respectively.

Figure 3.1. FT-IR of powder sample before SBF test.

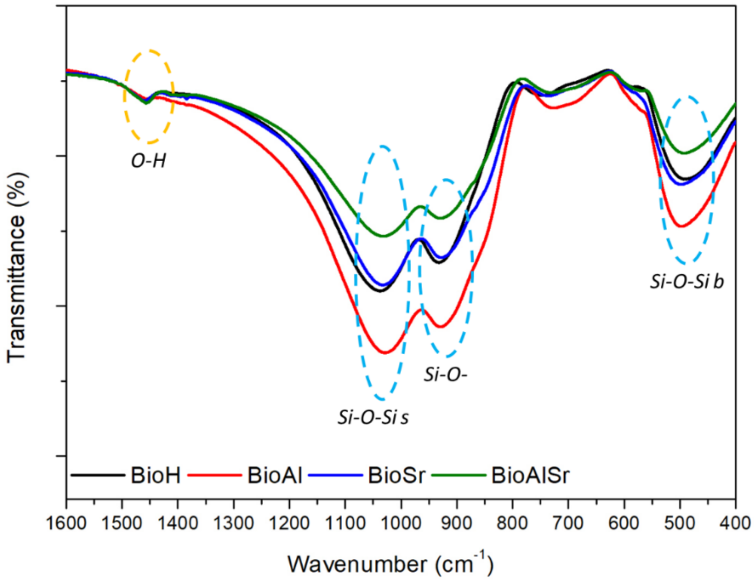

Source: the author.

Figure 3.2 shows the FTIR spectra after immersion in SBF. Time favored the appearance of phosphate and carbonate phases needed for HCA formation with prolonged exposition. A soaking time of 480 min was sufficient for reconfiguration of the existing features, and it can be observed that the bands at 1030, 940 and 490 cm^{-1} were substituted by a strong band at ~1060 cm^{-1} assigned to the P-O stretching vibration. This substitution is more evident for BioH and BioAlSr samples. Bands associated with amorphous and crystalline phosphorous can be identified all over the spectra at 460, 1150, 1210 and 1390 cm^{-1}. Additionally, minor peaks associated with HCA development can be observed at 1460 cm^{-1} for C-O stretching and 550 cm^{-1} for the crystalline phase of HCA.

Figure 3.2. FT-IR of powder sample after SBF test.

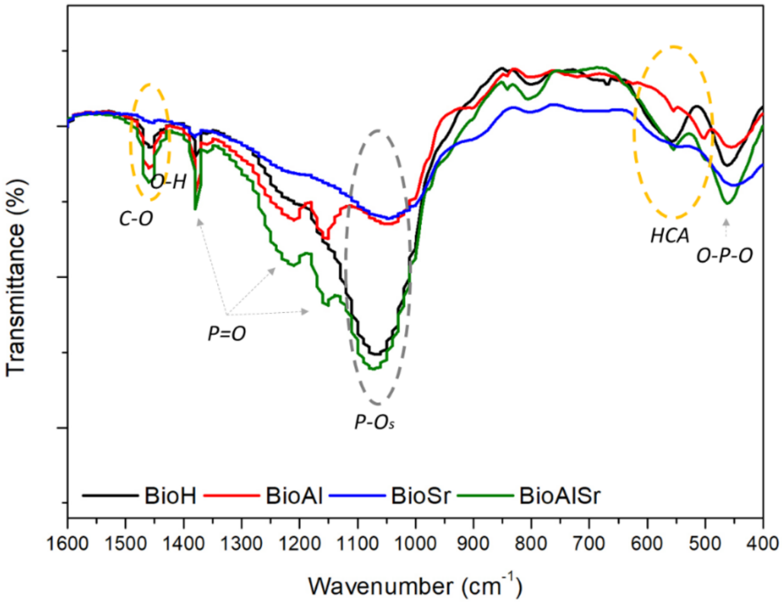

Source: the author.

In addition to FTIR, the medium was monitored by measuring the pH at 0, 5, 15, 30, 60, 120, 240 and 480 min. Figure 3 shows the variation in pH of the SBF solution with each sample and the control solution as a function of time.

Figure 3.3. pH mesurements during SBF test.

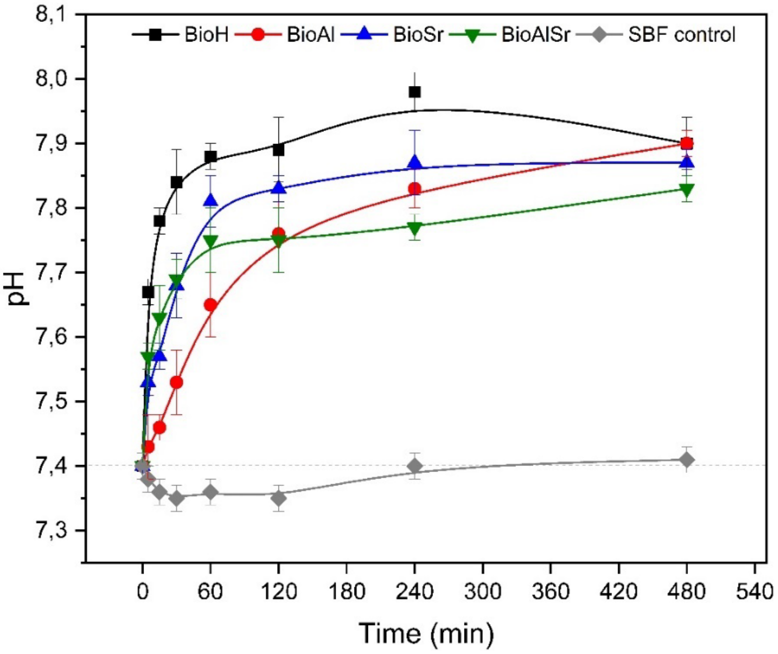

Source: the author.

As the sample powders have particle sizes in the same range, and the amount used was fixed, the variation in pH can be correlated to the composition of the glasses. The changes in pH relate to ion exchange and may vary with composition. Exchange is necessary to constitute a stable phase such as HCA. According to Jha and Singh, maximum degradation corresponds to the maximum pH change [27]. By considering this proposition, we can assume that BioAl and BioAlSr require more time to interact with the medium to reach maximum degradation, unlike samples BioH and BioSr. This might be due to the content of alumina in both samples since it is known that this compound affects glass dissolution. We can also observe that these samples (BioAl and BioAlSr) exhibit a decrease in the maxima of pH, related to the initial stage of dissolution, which comprises the cation exchange of ions such as Na+, showing the influence of alumina in the dissolution process. As dissolution occurs, the greater the cation exchange is, the greater the pH until it reaches the maximum degradation mentioned above. This has already been observed in other samples containing alumina studied by Tripathi et al. [11,28,29].

Although the addition of alumina delayed the initial pH increase in BioAl, which is common in bioactive glasses with such a composition, its association with

SrO reversed this effect. We can observe that BioAlSr, despite undergoing a decrease in maxima, had its initial rapid increase in pH restored [23,25]. We cannot presume that those pH maxima of samples BioAl and BioAlSr occurred at 480 min, when evaluation of dissolution mechanisms of all compositions was conducted, but we can consider that the results presented here supplement a recurrent drawback of bioactive glasses, which is a fast dissolution rate without losing reactivity. Investigation of alumina substitution of CaO content has shown that it reduces the reactivity and calcium phosphate formation [21]. On the other hand, its substitution to the detriment of P2O5 in phosphate-based glasses tends to provide an apatite layer that is more stable over a long period [15]. This is only possible because alumina is in the glass network as a former oxide, as in the BioAl and BioAlSr samples.

Figure 3.4 shows the surface morphology and EDS spectra for samples after the 480 min of immersion in SBF.

Figure 3.4. SEM/EDS micrographs of powder samples after 8h-SBF test.

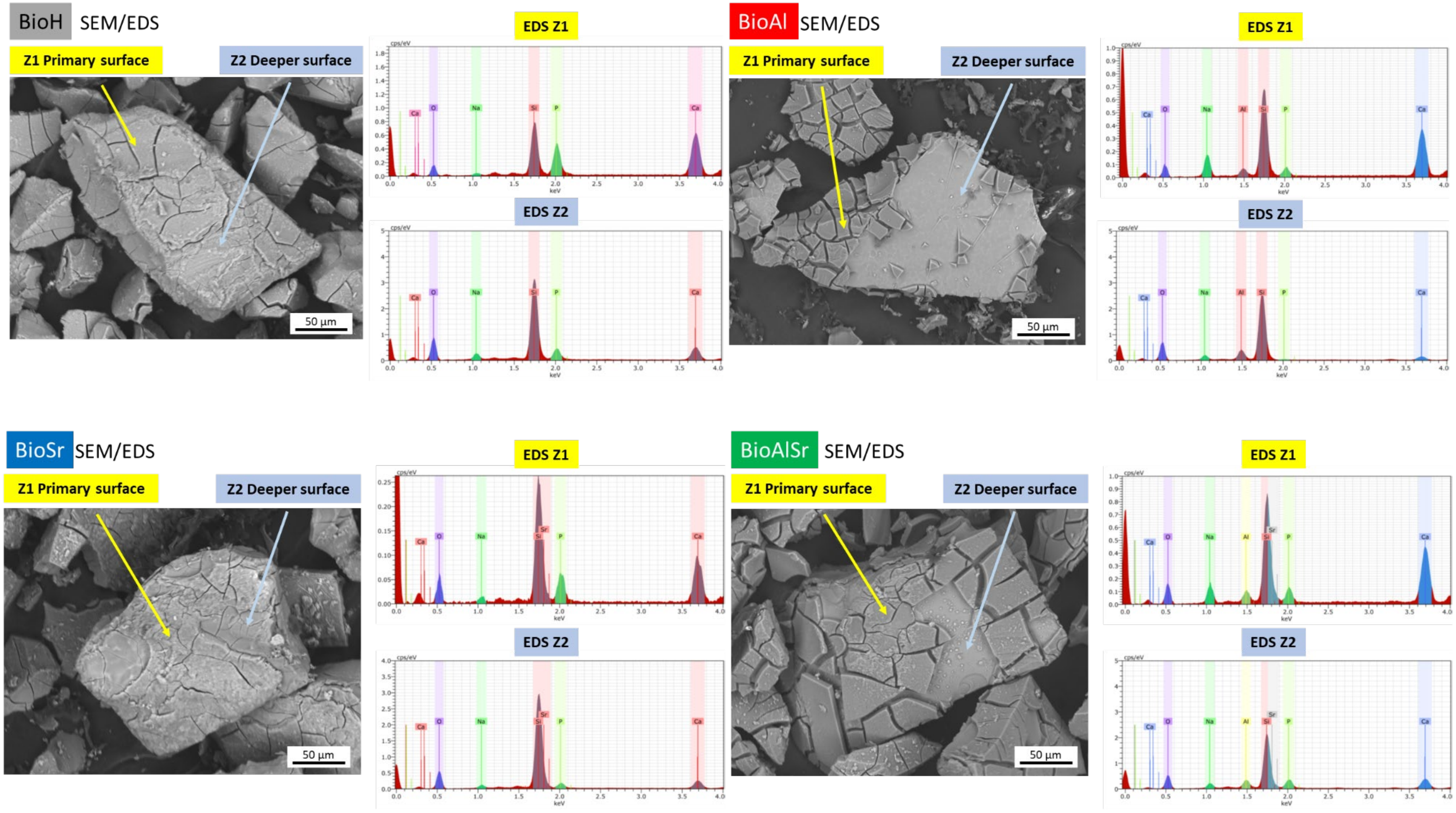

Source: the author.

As expected, the overall micrographs did not suggest any morphological characteristic formation of hydroxyapatite due to the short period of exposure. However, as degradation undoubtedly occurs, two surface patterns can be observed: one layer that is external and rich in calcium and phosphorous is identified as the primary surface in the images and the other layer that is more profoundly rich in silanol groups is identified as a deeper surface. Additionally, the EDS analysis confirms the differences in the composition of the layers.

Figure 3.5 shows the cumulative weight loss as a function of time obtained after the dissolution test.

Figure 3.5. Cumulative weight loss (%) in function of time (days) during the dissolution test.

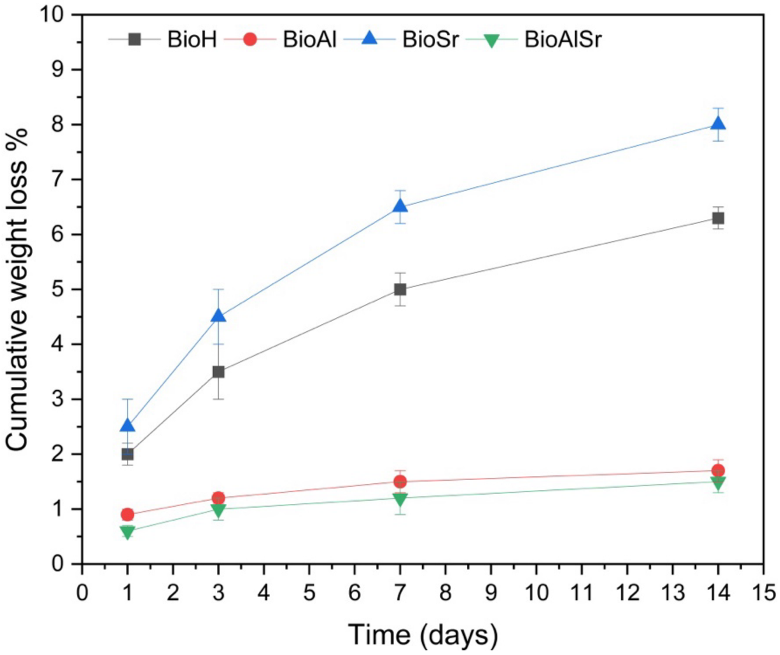

Source: the author.

For all the glass samples, a rising weight loss was observed as a function of time. However, BioAl and BioAlSr presented significantly lower losses than BioH and BioSr. The dissolution of alumina-containing samples appears to be slower and less intense, reaching a loss of only ~ 2% after 14 days. BioH and BioSr, in contrast, showed expressive and constant weight loss over time, reaching losses of 6% and 8%, respectively, after 14 days.

Considering the micrographs and dissolution rates, it appears that the samples with the slowest degradation had detached and peeled surfaces. In contrast, BioH and BioSr presented deeper surfaces that were less apparent, and greater amounts of Ca and P were found, probably because the greater the degradation was, the greater the reactivity. Nevertheless, detailed investigations of degradation and dissolution must be conducted.

3.3.2 In vitro bioactivity: monolithic samples

The formation of HCA layers on glass was studied in simulated body fluid according to the Kokubo protocol [16]. The XRD patterns of the glasses after 7 and 14 days of the bioactivity test are plotted in Figure 3.6 a and b, respectively, as well as the representative diffractogram patterns of crystalline apatite (red lines in the graph).

Figure 3.6. X-ray diffraction patterns after SBF test at 7 and 14 days of each sample.

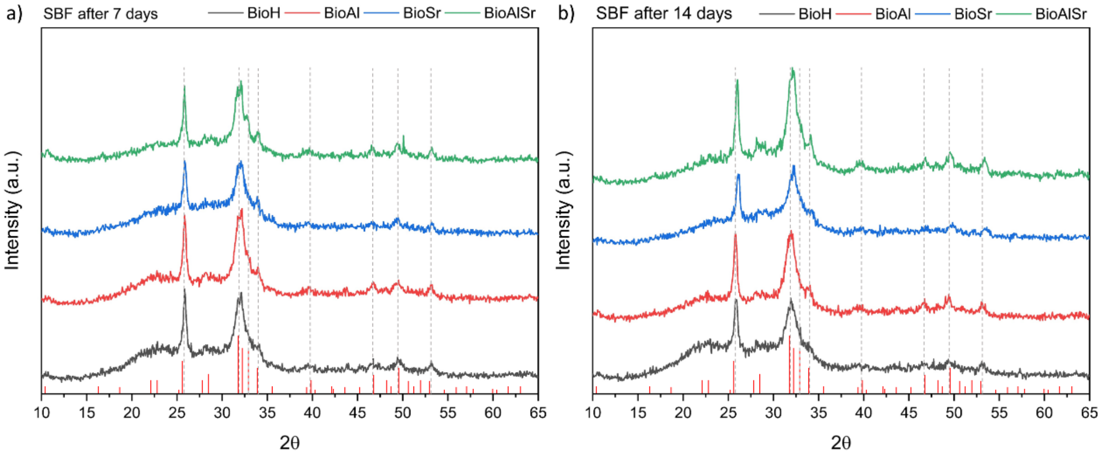

Source: the author.

After 7 days, the HCA appearance is clear, with intense peaks in 2θ between 25 and 26° and between 31 and 33° associated with lattice planes of HA [30,31]. Minor peaks near 47, 49 and 53° have been observed and are also related to HA. After 14 days, the peaks in 2θ between 25 and 26° and between 31 and 33° increased their diffraction intensities, and slight narrowing can be noticed. In both periods, a slight displacement towards higher 2θ values was observed for samples containing strontium (BioSr and BioAlSr), instead of lower values, as observed by Sriranganathan et al. [23].

Figure 3.7 and 3.8 shows the surface of all samples after 7 and 14 days soaking in SBF.

Figure 3.7. SEM micrographs after SBF test at 7 days a) BioH; b) BioAl; c) BioSr; d) BioAlSr.

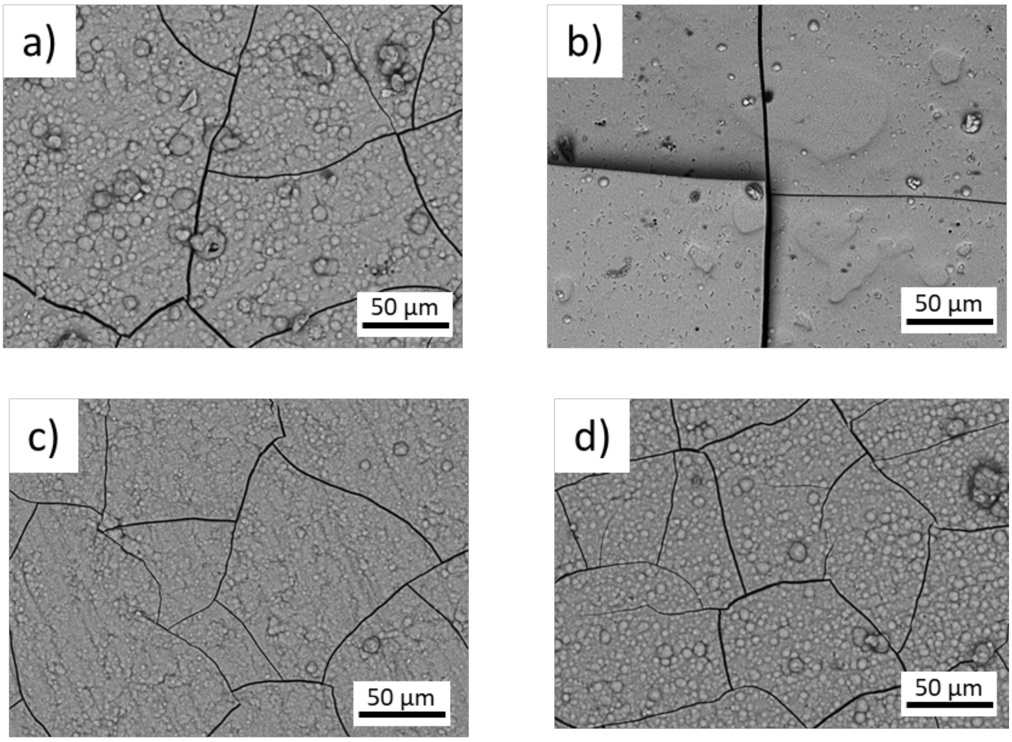

Source: the author.

Figure 3.8. . SEM micrographs after SBF test 14 days a) BioH; b) BioAl; c) BioSr; d) BioAlSr.

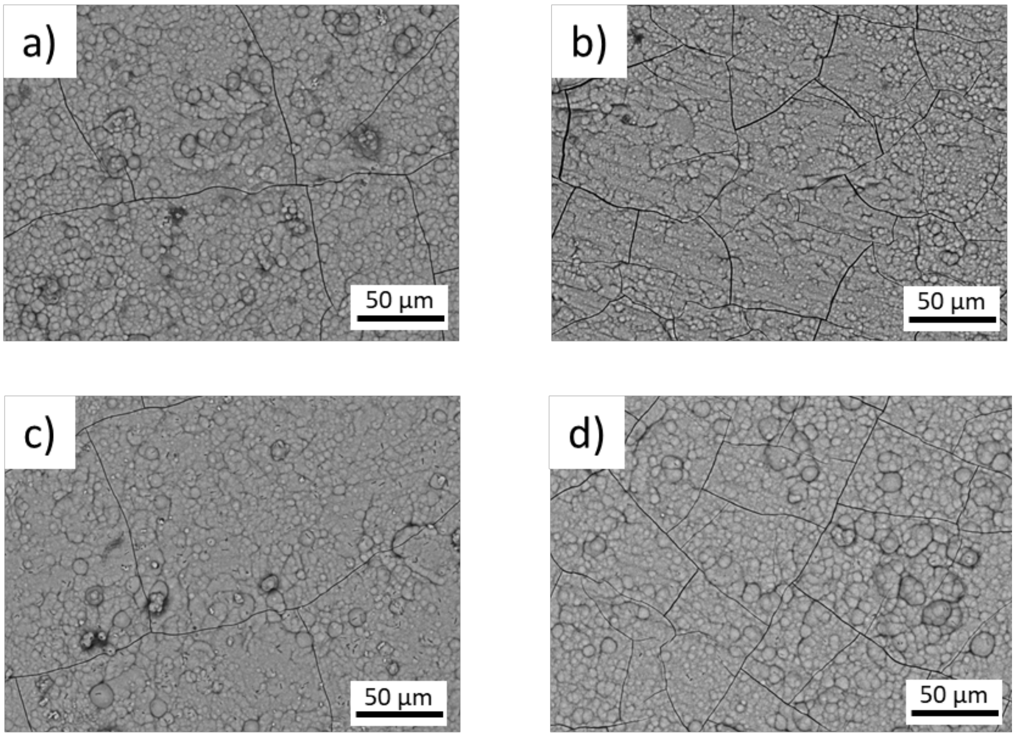

Source: the author.

After 7 days of immersion, excluding BioAl (Figure 7b), it is possible to observe the local formation of some globular deposits. Aggregate formation on top of BioH and BioAlSr with typical morphology of HCA can possibly indicate higher bioactivity of these samples. After 14 days, globular deposits were observed at the BioAl surface, suggesting that alumina addition did not inhibit HCA formation. BioH, BioSr and BioAlSr samples presented similar surfaces at 7 days with more aggregates.

3.3.3 Antibacterial sensitivity to *E. coli*

Sensitivity tests to E. coli bacteria were performed and are presented in Figure 3.9.

Figure 3.9. Colony forming units (CFU ml-1) of E. coli versus concentration (ppm) of powder samples.

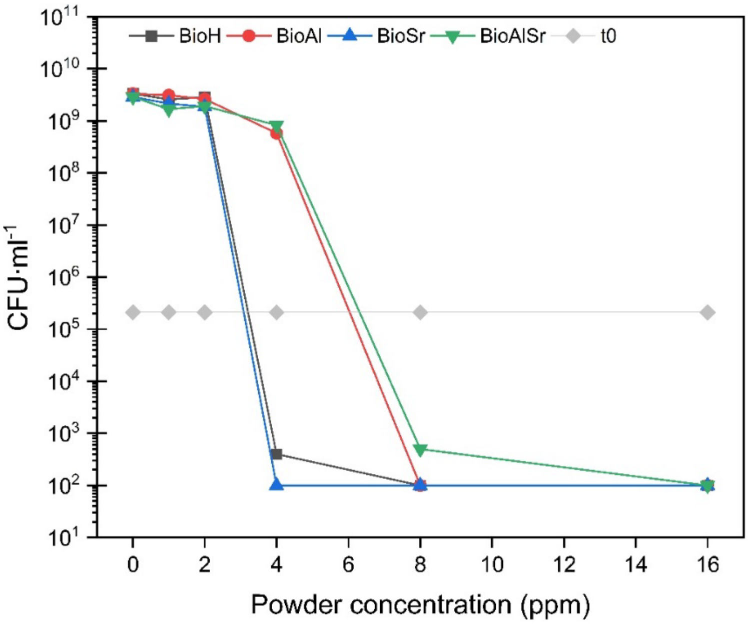

Source: the author.

The results showed a logarithmic reduction in the number of colonies of E. coli after 24 h as a function of the concentration in ppm of the powder in the solution. The gray line in the graph represents the initial concentration of E. coli (~2,11 × 105 CFU · mL^{-1}) for the different concentrations of powder. From the results, it can be observed that for all samples, a powder concentration above 4 ppm is required to achieve a logarithmic reduction higher than 7, indicating safe disinfection. BioH and BioSr presented a minimum inhibitory concentration (MIC) between 2 and 4 ppm, and BioAl and BioAlSr presented a minimum inhibitory concentration between 4 and 8 ppm. That is, after 24 h, the two samples containing alumina needed higher concentrations to inhibit the visible growth of a microorganism. Nevertheless, the minimum bactericidal concentration (MBC) was found to be 4 ppm for BioH and BioAl and 8 ppm for BioSr and BioAlSr. This behavior is directly connected to the rate of degradation of the samples since, as observed by Drago et al. [4,32], the increase in pH due to alkaline ion release makes the surrounding environment inopportune for bacterial growth. Therefore, it can be presumed that higher rates will provide the environment needed to inhibit bacterial growth faster.

3.3.4 Cytotoxicity

It can be seen in Figure 3.10 from the results that only the positive control showed cytotoxicity with an extract concentration of 100%; thus, all extracts from the 4 compositions of the glasses produced do not present cytotoxic potential.

Figure 3.10. Cell viability (%) of BioH, BioAl, BioSr and BioAlSr (dotted line: reference cell viability of IC50).

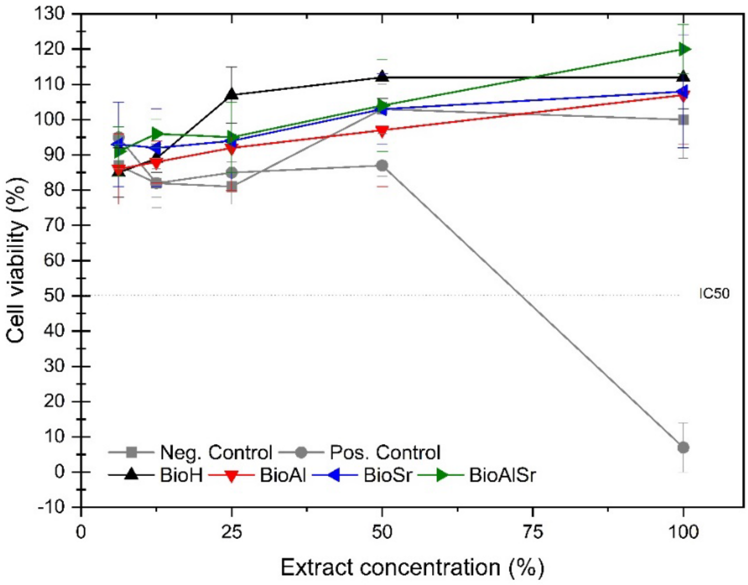

Source: the author.

The analysis shows the percentage of viability for different concentrations of extracts. According to ISO 10993-5, samples can be considered noncytotoxic when the cell viability, that is, the number of live cells after the test, is above 70% at an extract concentration of 100%. From the results, it can be observed that at all extract concentrations, the samples reached a cell viability greater than 70%. At a concentration of 100%, the cell viability was above 90% for all samples. Hence, the samples tested can be considered noncytotoxic.

3.4 Chapter 3 Conclusions

The present chapter presented the evaluation of in vitro bioactivity and antibacterial effect against E. coli. of the novel composition. By adding 2 mol% Al2O3 and 2 mol% SrO to 45S5, the bioactivity was preserved even as the glass degradation decreased because of the alumina capability. The formation of phosphate and carbonate phase precursors of HCA was observed after 480 min for powder samples, and after 7 and 14 days, SEM analysis of monolithic samples confirmed HCA formation. XRD patterns confirmed that the substitutional ions adapted to the crystal lattice of HCA without compromising its structure. None of the samples evaluated were considered cytotoxic by the neutral red uptake methodology. Furthermore, after overnight incubation, the samples exhibited safe disinfection for E. coli. The results showed that the designed composition achieved the combined effect of antibacterial activity and biocompatibility, contributing to the field of bioactive glasses used for bone regeneration applications.

REFERENCES

[1] F. Baino, S. Hamzehlou, S. Kargozar, Bioactive Glasses: Where Are We and Where Are We Going?, J. Funct. Biomater. 9 (2018) 25. doi:10.3390/jfb9010025.

[2] E. Fiume, J. Barberi, E. Verné, F. Baino, Bioactive Glasses: From Parent 45S5 Composition to Scaffold-Assisted Tissue-Healing Therapies, J. Funct. Biomater. 9 (2018) 24. doi:10.3390/jfb9010024.

[3] L. Esteban-Tejeda, A. Smirnov, C. Prado, J. S. Moya, R. Torrecillas, J. F. Bartolomé, Multifunctional ceramic-metal biocomposites with Zinc containing antimicrobial glass coatings, Ceram. Int. 42.6 (2016) 7023-7029. doi:10.1016/j.ceramint.2016.01.090.

[4] L. Drago, M. Toscano, M. Bottagisio, Recent Evidence on Bioactive Glass Antimicrobial and Antibiofilm Activity: A Mini-Review, Materials (Basel). 11 (2018) 326. doi:10.3390/ma11020326.

[5] S. Lopez-Esteban, J.F.Bartolomé, L.A.Diaz, L.Esteban-Tejeda, C.Prado, R. Lopez-Piriz, R.Torrecillas, J.S.Moya, Mechanical performance of a biocompatible biocide soda–lime glass-ceramic, J. Mech. Behav. Biomed. 34 (2014) 302-312. doi:10.1016/j.jmbbm.2014.02.019.

[6] A. Martinez, F. Guitián, R. López-Píriz, J.F Bartolomé, B. Cabal, L. Esteban-Tejeda, R. Torrecillas, J.S. Moya, Bone loss at implant with titanium abutments coated by soda lime glass containing silver nanoparticles: A histological study in the dog, Plos One 9 (2014) e86926. doi:10.1371/journal.pone.0086926.

[7] R. Lopez-Piriz, E. Sola-Linares, J.-J. Granizo, I. Diaz-Guemes, S. Enciso, J. F. Bartolomé, B. Cabal, L. Esteban-Tejada, R. Torrecillas, J.S. Moya, Radiologic evaluation of bone loss at implants with biocide coated titanium abutments: A study in the dog, Plos One 7 (2012) e52861. doi: 10.1371/journal.pone.0052861.

[8] B. Cabal, F. Cafin, L. Esteban-Tejeda, L. Alou, J.F. Bartolomé, D. Sevillano, R. López-Piriz, R. Torrecillas, J.S. Moya, Inhibitory effect on in vitro Streptococcus oralis biofilm of a soda-lime glass containing silver nanoparticles coating on titanium alloy, Plos One 7 (2012) e42393. doi: 10.1371/journal.pone.0042393.

[9] M.S. Araujo, J.F. Bartolomé, S. Mello-Castanho, Tribological and mechanical behaviour of 45S5 Bioglass®-based compositions containing alumina and strontium, Ceram. Int. 46 (2020) 24347–24354. doi:10.1016/j.ceramint.2020.06.216.

[10] M.S. Araujo, A.C. Silva, J.F. Bartolomé, S. Mello-Castanho, Structural and thermal behavior of 45S5 Bioglass ® -based compositions containing alumina and strontium, J. Am. Ceram. Soc. 103 (2020) 3620–3630. doi:10.1111/jace.17061.

[11] H. Tripathi, C. Rath, A.S. Kumar, P.P. Manna, S.P. Singh, Structural, physico-mechanical and in-vitro bioactivity studies on SiO2–CaO–P2O5–SrO–Al2O3 bioactive glasses, Mater. Sci. Eng. C. 94 (2019) 279–290. doi:10.1016/j.msec.2018.09.041.

[12] S.M. Rabiee, N. Nazparvar, M. Azizian, D. Vashaee, L. Tayebi, Effect of ion substitution on properties of bioactive glasses: A review, Ceram. Int. 41 (2015) 7241–7251. doi:10.1016/j.ceramint.2015.02.140.

[13] Y. Li, W. Stone, E.H. Schemitsch, P. Zalzal, M. Papini, S.D. Waldman, M.R. Towler, Antibacterial and osteo-stimulatory effects of a borate-based glass series doped with strontium ions, J. Biomater. Appl. 31 (2016) 674–683. doi:10.1177/0885328216672088.

[14] J. Zhang, S. Zhao, Y. Zhu, Y. Huang, M. Zhu, C. Tao, C. Zhang, Three-dimensional printing of strontium-containing mesoporous bioactive glass scaffolds for bone regeneration, Acta Biomater. 10 (2014) 2269–2281. doi:10.1016/j.actbio.2014.01.001.

[15] A.A. El-Kheshen, F.A. Khaliafa, E.A. Saad, R.L. Elwan, Effect of Al2O3 addition on bioactivity, thermal and mechanical properties of some bioactive glasses, Ceram. Int. 34 (2008) 1667–1673. doi:10.1016/j.ceramint.2007.05.016.

[16] T. Kokubo, H. Kushitani, S. Sakka, T. Kitsugi, T. Yamamuro, Solutions able to reproducein vivo surface-structure changes in bioactive glass-ceramic A-W3, J. Biomed. Mater. Res. 24 (1990) 721–734. doi:10.1002/jbm.820240607.

[17] A.C. Silva, S.R.H. Mello-Castanho, Vitrified galvanic waste chemical stability, J. Eur. Ceram. Soc. 27 (2007) 565–570. doi:10.1016/j.jeurceramsoc.2006.04.110.

[18] Biological Evaluation of Medical Devices – Part 5: Tests for In Vitro Cytotoxicity, 2009.

[19] S.O. Rogero, S.M. Malmonge, A.B. Lugão, T.I. Ikeda, L. Miyamaru, Á.S. Cruz, Biocompatibility Study of Polymeric Biomaterials, Artif. Organs. 27 (2003) 424–427. doi:10.1046/j.1525-1594.2003.07249.x.

[20] C. Santos, S. Ribeiro, J.K.M.F. Daguano, S.O. Rogero, K. Strecker, C.R.M. Silva, Development and cytotoxicity evaluation of SiAlONs ceramics, Mater. Sci. Eng. C. 27 (2007) 148–153. doi:10.1016/j.msec.2006.04.003.

[21] L. Hupa, S. Fagerlund, J. Massera, L. Björkvik, Dissolution behavior of the bioactive glass S53P4 when sodium is replaced by potassium, and calcium with magnesium or strontium, J. Non. Cryst. Solids. 432 (2016) 41–46. doi:10.1016/j.jnoncrysol.2015.03.026.

[22] A.C. Da Silva, Structure and percolation of bioglasses, in: Adv. Struct. Mater., Springer: Cham. (2016), 49–84.

[23] D. Sriranganathan, N. Kanwal, K.A. Hing, R.G. Hill, Strontium substituted bioactive glasses for tissue engineered scaffolds: the importance of octacalcium phosphate, J. Mater. Sci. Mater. Med. 27 (2016) 39. doi:10.1007/s10856-015-5653-6.

[24] R. Wetzel, D.S. Brauer, Apatite formation of substituted Bioglass 45S5: SBF vs. Tris, Mater. Lett. 257 (2019) 126760. doi:10.1016/j.matlet.2019.126760.

[25] Y.C. Fredholm, N. Karpukhina, D.S. Brauer, J.R. Jones, R. V Law, R.G. Hill, Influence of strontium for calcium substitution in bioactive glasses on degradation, ion release and apatite formation, J. R. Soc. Interface. 9 (2012) 880–889. doi:10.1098/rsif.2011.0387.

[26] E. Kontonasaki, T. Zorba, L. Papadopoulou, E. Pavlidou, X. Chatzistavrou, K. Paraskevopoulos, P. Koidis, Hydroxy Carbonate Apatite Formation on Particulate Bioglass In Vitro as a Function of Time, Cryst. Res. Technol. 37 (2002) 1165–1171. doi:10.1002/1521-4079(200211)37:11<1165::AID-CRAT1165>3.0.CO;2-R.

[27] P. Jha, K. Singh, Effect of MgO on bioactivity, hardness, structural and optical properties of SiO2–K2O–CaO–MgO glasses, Ceram. Int. 42 (2016) 436–444. doi:10.1016/j.ceramint.2015.08.128.

[28] H. Tripathi, S. Kumar Hira, A. Sampath Kumar, U. Gupta, P. Pratim Manna, S.P. Singh, Structural characterization and in vitro bioactivity assessment of SiO2–CaO–P2O5–K2O–Al2O3 glass as bioactive ceramic material, Ceram. Int. 41 (2015) 11756–11769. doi:10.1016/j.ceramint.2015.05.143.

[29] S.K. Arepalli, H. Tripathi, S.K. Hira, P.P. Manna, R. Pyare, S.P.Singh, Enhanced bioactivity, biocompatibility and mechanical behavior of strontium substituted bioactive glasses, Mater. Sci. Eng. C. 69 (2016) 108–116. doi:10.1016/j.msec.2016.06.070.

[30] Y. Yu, Z. Bacsik, M. Edén, Contrasting In Vitro Apatite Growth from Bioactive Glass Surfaces with that of Spontaneous Precipitation, Materials (Basel). 11 (2018) 1690. doi:10.3390/ma11091690.

[31] M.D. CALASANS-MAIA, B.R. de MELO, A.T.N.N. ALVES, R.F. de B. RESENDE, R.S. LOURO, S.C. SARTORETTO, J.M. GRANJEIRO, G.G. ALVES, Cytocompatibility and biocompatibility of nanostructured carbonated hydroxyapatite spheres for bone repair, J. Appl. Oral Sci. 23 (2015) 599–608. doi:10.1590/1678-775720150122.

[32] L. Drago, E. De Vecchi, M. Bortolin, M. Toscano, R. Mattina, C.L. Romanò, Antimicrobial activity and resistance selection of different bioglass S53P4 formulations against multidrug resistant strains, Future Microbiol. 10 (2015) 1293–1299. doi:10.2217/FMB.15.57.

CHAPTER 4: Tribological and mechanical behavior

4.1 Background

Bioactive glasses have proved to be a material with immense interest in medicine owing to its reliable capacity to repair or replace diseased or damaged bones [1]. However, the inherent limited mechanical properties and low wear resistance of bioactive glasses are still their main drawbacks limiting their use in applications such as load bearing devices despite their excellent bioactivity and bonding strength with bone [2–4].

Because the intrinsic fracture toughness of bioactive glass is dramatically low, the damage and crack resistance improvement are of prime importance, particularly when applied to the repair of load bearing bones [5]. On the other hand, appropriate wear resistance is also crucial for the in vivo osteointegration, fixation, and lifetime performance of an implant [6]. Therefore, tribological properties are especially critical for the load-bearing surfaces of orthopedic and dental implants, where bioactive glasses have been widely used as coating, and also when bulk bioactive glasses are employed in orthopedic applications [7,8].

Although improving mechanical and tribological properties is critical, many bioactive glasses belong to complex systems, and so completely understanding and optimizing not only the mechanical properties but the overall properties by tailoring the structure and composition is not a simple task, and up to now it is still a matter of debate [2,3]. The present research investigated the mechanical and tribological behavior of four 45S5-based compositions with low strontium oxide and alumina contents. Several studies have associated strontium with improved mechanical properties, such as flexural strength and elastic modulus [5–7,9]. Likewise, alumina enhances the mechanical properties by increasing the fracture toughness and hardness [6,8].

In our previous study [10], a new 45S5 Bioglass®-based composition containing both strontium and alumina was proposed. Structural and thermal characterizations were conducted in ^{31}P, ^{27}Al, ^{23}Na and ^{29}Si environments obtained using magic-angle spinning–nuclear magnetic resonance (MAS-NMR). The results revealed that the incorporation of Al_2O_3 as a four-coordinated form is essential for optimizing the influence of SrO in the system. The modifications significantly changed the thermal stability, amplifying the working window. Even though many derived bioactive glasses containing strontium and alumina have been investigated. Also, there is a lack of data on the mechanical performance and wear resistance of these silicate glasses.

4.2 Experimental procedure

4.2.1 Sample preparation

The glasses were prepared from the stablished compositions and procedure presented in Chapter 1 (Section 1.2).

The glasses were cast into parallelepipedal bars (40 × 15 × 5 mm) and cylindrical (40 mm × Ø15 mm) molds. The densities of the samples were determined by Archimedes' principle with deionized water as the immersion liquid at room temperature.

4.2.2 Flexural strength and elastic modulus

Five specimens of each composition were subjected to a biaxial flexural strength test in a universal testing machine (Shimadzu Auto Graph AG-X5kN, Japan). The biaxial flexural strength was measured using the piston-on-3-ball method according to the international standard ISO 6872 [11]. Steel balls with diameters of 3.2 mm located every 120° on the circumference of a circle 10 mm in diameter were used for the support. The head was of a flat stylet type with a diameter of 1.2 mm. The tests were performed at room temperature at a crosshead speed of 0.5 mm/min. Samples 15 mm in diameter with thicknesses between 1.3 and 1.5 mm were used for this method.

The bending flexural strength and Young's modulus were measured on a three-point bending test at room temperature using the same testing machine as that used for biaxial strength determination but with an inner span of 30 mm and a crosshead speed of 0.5 m/min. Prismatic samples 40 mm long, 4 mm thick and 12 mm wide were used for the tests. The tensile faces of all specimens (five bars for each composition) were worn with silicon carbide sandpaper and polished with a ceria suspension to less than 1 µm (Struers, RotoPol-22), and the edges were chamfered (~45°) to avoid the influence of microcracks on the mechanical results. The elastic modulus was calculated from the slopes of the load-deflection curves. The formulas, calculation procedures and equipment configuration details used in both the flexural strength and three-point bending tests are described in previous publications [12,13].

4.2.3 Vickers hardness (HV) and fracture toughness (K_{IC})

The Vickers hardness (HV) of the specimens was determined by microindentation (Buehler model Micromet 5103, Germany) on samples 5 mm thick with surfaces polished to less than 1 µm with a ceria suspension, applying a load of 25 g with an indentation time of 10 s. Fifty Vickers impressions were carried out for each tested sample. The indentation diagonal lengths were measured using an optical microscope. The Vickers indentation fracture was selected to evaluate the fracture toughness (K_{IC}). The indentation and measurement techniques were the same as those for HV; however, the load utilized was 50 g and the lengths of the radial cracks were measured instead of diagonals. The formula is given by Miranzo and Moya [14]. The fracture toughness variation and statistical analysis among each set of samples were evaluated by calculating the cumulative probability and the Weibull modulus (m). The formulas are given by Gong [15].

4.2.4 Wear test det-Up and conditions

A "ball-on-disk"-type wear test was performed using a tribometer (Microtest MT/60/NI, Microtest S.A., Madrid, Spain) in conformity with ASTM G99, in which the glass samples were slid against a stainless-steel ball 6 mm in diameter. For all samples, the applied normal load (F_N) was 3 N, corresponding to an initial Hertzian contact pressure of 0.21 GPa. The test duration corresponded to 1000 m, with a rotation of 180 rpm and a radius of 4.25 mm in unlubricated conditions. At least three sliding wear tests were conducted for each composition. Before each test, the samples were rinsed ultrasonically in acetone and then dried at 90 °C for 30 min. After each sliding test, the worn surfaces were cleared by blowing them with pressurized air before observations. All experiments were carried out under the same conditions, in laboratory air at room temperature, with an average relative humidity of 50 ± 5%. The specific wear rate, *W*, was calculated by using Eq. (1).

$$W = \frac{\Delta V}{F_N \cdot S} \quad (1)$$

where ΔV is the volume loss after the tests (mm³), F_N is the applied load (N) and S is the sliding distance (m). To estimate the volume losses, the track profiles were analyzed with a surface profilometer (Talysurf CLI 500, Taylor Hobson, Leicester, UK) that maps the measured area by tip-sample surface contact, using a step of 0.01 µm and a scanning speed 0.1 mm/s. A profilometer was used to determine three-dimensional surface topographic maps, so track volumes were estimated, and hence Eq. (1) could be applied. The wear scars were also examined by scanning electron microscopy (SEM; TM3000, Hitachi High-Technologies Co., Tokyo, Japan) at 15 kV of accelerating voltage. Chemical characterization was performed by energy dispersive X-ray spectroscopy (EDX), which used a silicon-drift detector (SDD) of 30 mm² and a resolution of 135 eV (QUANTAX 70 system). The acquisition time for EDX was 200 s for a line scan of 300 µm.

4.2.5 Raman Spectroscopy

Raman spectroscopy was carried out using a micro-Raman spectrometer (WITEC, Confocal Raman Microscope Alpha300 R). The samples were excited by the 532 nm line of an Ar^+ laser and recorded with a microscope objective 50×/0.7 at 60 s integration time with 45 mW power. The spectra were collected in slices 3 mm thick.

4.3 Results and Discussions

4.3.1 Mechanical properties

Table 4.1 summarises the measured density (ρ), biaxial flexural (σF) and bending (σB) strengths, hardness (HV) and elastic modulus (E).

Table 4.1. Mechanical properties of samples BioH, BioAl, BioSr and BioAlSr.

Composition	ρ, g/cm³	σ_F, MPa	σ_B, MPa	HV, GPa	K_{IC}, MPa m$^{1/2}$	E, GPa
BioH	2.6920	81 ± 9	50 ± 3	3.6 ± 0.3	0.2 ± 0.02	50 ± 1
BioAl	2.6948	79 ± 8	68 ± 2	3.8 ± 0.3	0.2 ± 0.01	48 ± 2
BioSr	2.7108	97 ± 8	75 ± 5	4.4 ± 0.2	0.3 ± 0.01	51 ± 2
BioAlSr	2.7661	109 ± 8	80 ± 5	4.7 ± 0.3	0.4 ± 0.02	50 ± 2

The experimental density for BioH was 2.6920 g/cm³, which is close to the reported data (~2.702 g/cm³) [16]. Like BioH, BioAl presented a density of 2.6948 g/cm³ instead of the increase observed by other authors [17,18]. This is due to the replacement of silicon by aluminum, which have similar atomic weights, 28.085 and 26.981 g·mol^{-1}, respectively. Furthermore, especially in this composition, alumina acted as a former oxide, i.e., in tetrahedral form, and so it effectively replaced the silica in the glass network, as already discussed in our previous work [10]. There was also a clear increase in the density of the BioSr and BioAlSr samples. As expected, owing to its large atomic ratio (~2.45 Å), the addition of strontium to the vitreous network led to an increase in density [16,19]. However, although the density of BioSr was 2.7108 g/cm³, that of BioAlSr was 2.7661 g/cm³. This difference, even with the same content, was probably owing to the fact that Sr ions occupied distinct positions in the network, as discussed above.

The elastic modulus (*E*) of silicate glasses is directly linked to their composition, usually by increasing the alkali cation concentration, and thus a decrease in *E* is observed. In contrast, metal oxide additions such as SrO can contribute to an increase in *E* [20–22]. Because the concentration of the modifications was small, all the samples presented similar elastic moduli, around 50 GPa, which conforms to the results of other studies of samples with similar compositions [23,24]. Even though Al_2O_3 acted as a former oxide in BioAl, its presence caused depolymerization of the silica network, weakening bonds and increasing surface tension. This is mainly due to the replacement of silica with alumina, which is known to make stronger bonds. Thus, it is not expected that alumina, in this particular case, will improve mechanical properties such as fracture toughness and hardness, as pointed out by other authors [6,8,18].

The HV values obtained for BioH and BioAl were similar, 3.6 and 3.8 GPa, respectively, which might be explained by the weakening bonding strength in the glass network. No changes were expected because replacing silica with Al_2O_3 decreased some bonding strength on the atomic scale. Also, an increase in HV usually relates to higher compactness of the glass network with strong bonding strength [25]. In contrast, in the BioSr sample, although the composition resulted in depolymerization of the network, the incorporation of SrO favored compactness of the network, thus increasing HV up to 20%. Similarly, with BioAlSr, despite having a different network configuration because of the presence of both Al_2O_3 and SrO, HV varied from 3.6 to 4.7 GPa, indicating an increase of 30%.

The obtained data for all fifty K_{IC} measurements, including minimum and maximum values, were arranged for cumulative distribution function and Weibull analysis. The statistical results of all measurement data, i.e., minimum (K_{ICmin}), maximum (K_{ICmax}), arithmetic average (K_{ICav}), standard deviation and Weibull parameters, are summarized in Table 4.2.

Table 4.2. Statistical results for the measured indentation toughness of samples BioH, BioAl, BioSr and BioAlSr for indentation load of 50 g.

Composition	Indentation toughness, K_{IC} (MPa $m^{1/2}$)				Weibull parameters	
	Minimum	Maximum	Average	Standard deviation	K_0 (MPa $m^{1/2}$)	m
BioH	0.16	0.21	0.17	0.02	0.18	13.3
BioAl	0.20	0.24	0.22	0.01	0.23	18.7
BioSr	0.25	0.31	0.27	0.01	0.27	19.7
BioAlSr	0.34	0.41	0.37	0.02	0.38	21.4

The cumulative distribution was constructed by normalizing the data by their average and then ordering the values from the lowest to the highest, taking into account the fact that the cumulative probability of failure (P_i) corresponded to the i^{th} position in the rank of K_{IC}/K_{ICav} and given by (i – 0,5)/50 [15]. The Weibull parameters, K_0 (characteristic toughness) and m (Weibull modulus), were estimated by considering the scale factor, i.e., the probability at 63% and the slope of the fitting curve of each sample, respectively.

The average of K_{IC} values for the four samples varied from 0.18 to 0.38 MPa·m$^{1/2}$ for BioH and BioAlSr, respectively. Similar to HV, the K_{ICav} values for BioH and BioAl were similar. The K_{IC} value for the BioSr sample increased to 0.27 MPa·m$^{1/2}$ and that of BioAlSr was found to be double that of BioH, 0.38 MPa·m$^{1/2}$. The coefficient of variation for K_{Ic} fluctuated between 5 and 11%, in agreement in magnitude with other glasses such as soda-lime, which are typically around 10% [15]. Although the results found for K_{Ic} were still lower than those of other commercial glass or glass-ceramics with enhanced toughness, such as Biosilicate® (≈1.0 MPa·m$^{1/2}$) and Bioverit® (0.5–2.0 MPa·m$^{1/2}$), they are substantial in terms of the main goal of this study, which was to improve the mechanical properties without changing the beneficial characteristics of BioH (45S5) and also considering bulk samples without any thermal, surface treatment or second-phase reinforcements such as biopolymers, biometals, bioceramics, or carbon materials [26–28].

The cumulative distributions reported in Figure 4.1 indicate the same trend for all compositions, in conformity with other glasses from the literature [15,29,30]. The Weibull probability plots in Figure 4.2 for all four compositions indicate a linear trend. However, deviations from linearity can be observed more clearly for BioH, which presented a lower m, 13.3. For BioAl and BioSr, the m values were 18.7 and 19.7, respectively. BioAlSr presented a higher m, 21.4. Comparing the results, we can assume that despite the fact that BioH possesses a Weibull modulus similar to that of a soda-lime glass (m = 13) [15], considered a homogenous material, higher values for this modulus such as for BioAlSr (m = 21.4), could be associated with a material with even higher homogeneity.

Figure 4.1. Cumulative distribution function for normalised toughness of all the glasses.

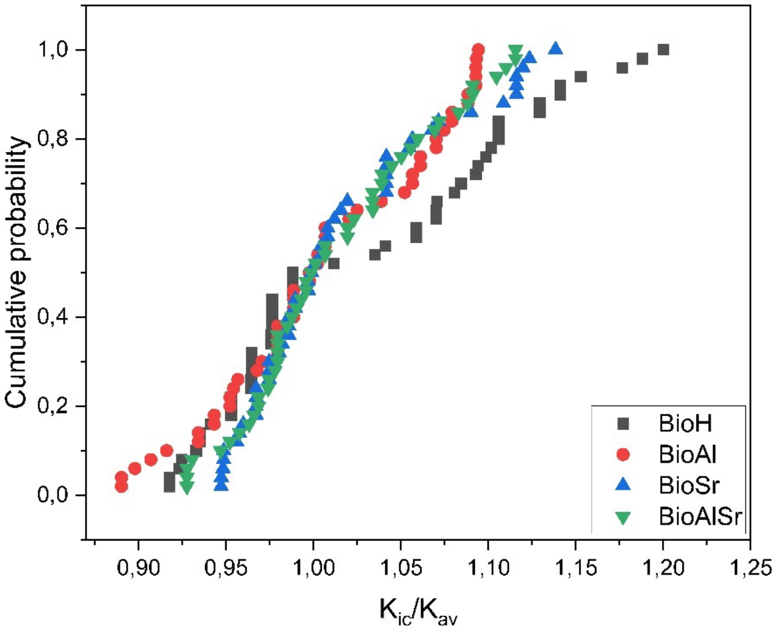

Source: the author.

Figure 4.2. Weibull plots for the indentation toughness of all glasses.

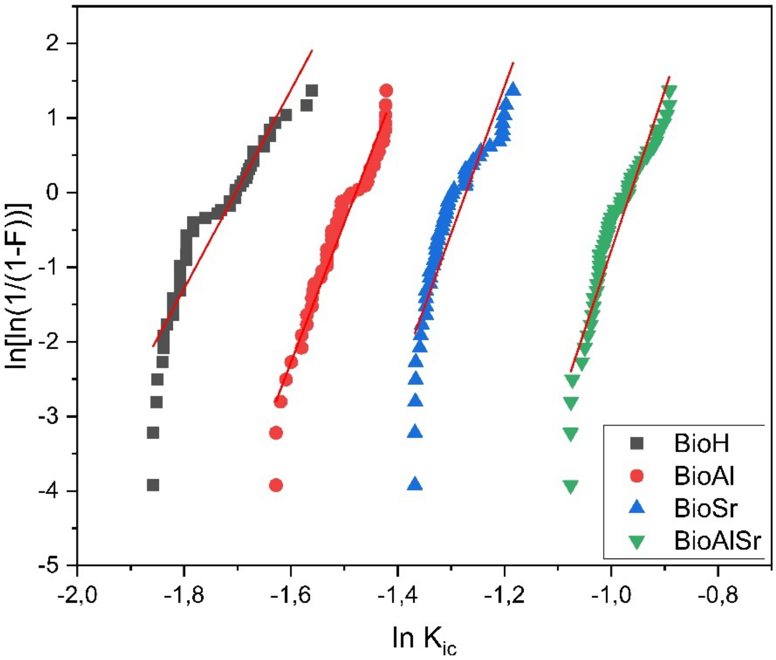

Source: the author.

4.3.2 Tribological behavior

It is important to point out that the information on the wear performance of bioglasses is still scarce. Li et al. [31] reported the first use of graphene nanoplatelets (GNPs) to enhance the wear resistance of 45S5 against an alumina ball. In our study, wear resistance (*W*) against a stainless-steel ball was evaluated. Different plots corresponding to the friction coefficient as a function of distance for each material registered for a 3 N contact load are shown in Figure 4.3.

Figure 4.3. Friction coefficient as function of sliding distance for samples sliding at 0.02 m/s under a 3 N contact load against a stainless steel ball.

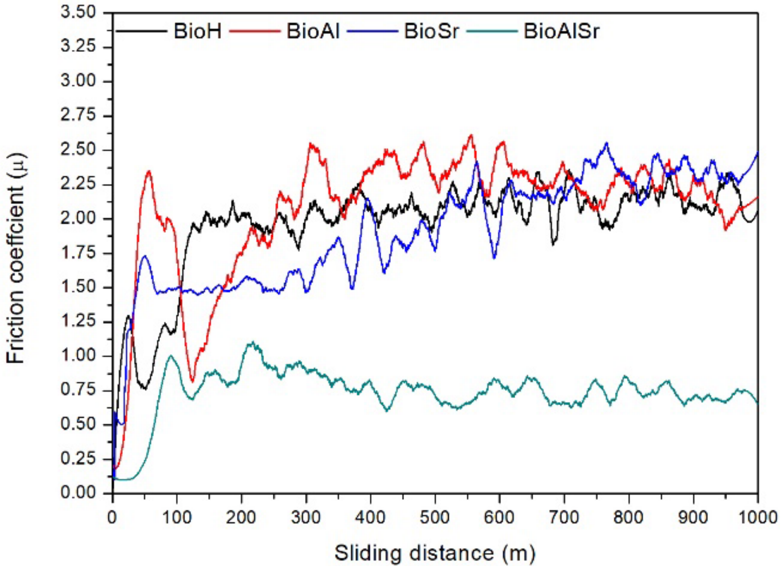

Source: the author.

All samples tested exhibit similar behavior: the friction coefficient increases rapidly through the first few meters, and the test proceeds, the initial roughness strongly decreases and the friction coefficient stabilizes. This behavior can be attributed to the polishing effect during the outset of the wear test [32,33]. Still, the coefficient changed significantly according to the sample, which varied from 0.8 to 2.2. After the initial stage, the coefficient of the BioAlSr sample was fixed at 0.8, almost three times lower than the rest of the samples (≈2.1).

Table 4.3 shows that the friction coefficient (*μ*) reached a steady-state, and data were generated from the three-dimensional (3D) profiles of the tested surfaces, such as the volume loss (Δ*V*) and calculated wear rate (*W*),

Table 4.3. Volume loss (ΔV), friction coefficient (μ) and wear rate (W) after wear tests under 3N load against stainless steel ball.

	Friction coefficient (μ)	ΔV (mm^3)	W ($mm^3/N \cdot m$)
BioH	2.1	0.16	$5.4x10^{-5}$
BioAl	2.2	0.16	$5.4x10^{-5}$
BioSr	2.1	0.16	$5.2x10^{-5}$
BioAlSr	0.8	0.09	$2.2x10^{-5}$

The smallest wear track volume loss was measured for the BioAlSr sample, with a *W* value of 2.2 × 10^{-5}, which was found to be triple the wear resistance of BioH. Figures 4.4(a–d) show the surface topographies of the 3D wear tracks for all samples obtained. As expected, the variations in friction coefficient and wear rate generated different wear tracks. The reduced wear rate and friction coefficients of BioAlSr resulted in the smaller width and depth in its 3D profiles.

Figure 4.4. Representative 3D final wear track topographies corresponding to BioH (a), BioAl (b), BioSr (c) and BioAlSr (d) as a function of depth (colored scale) under contact load 3 N against steel ball.

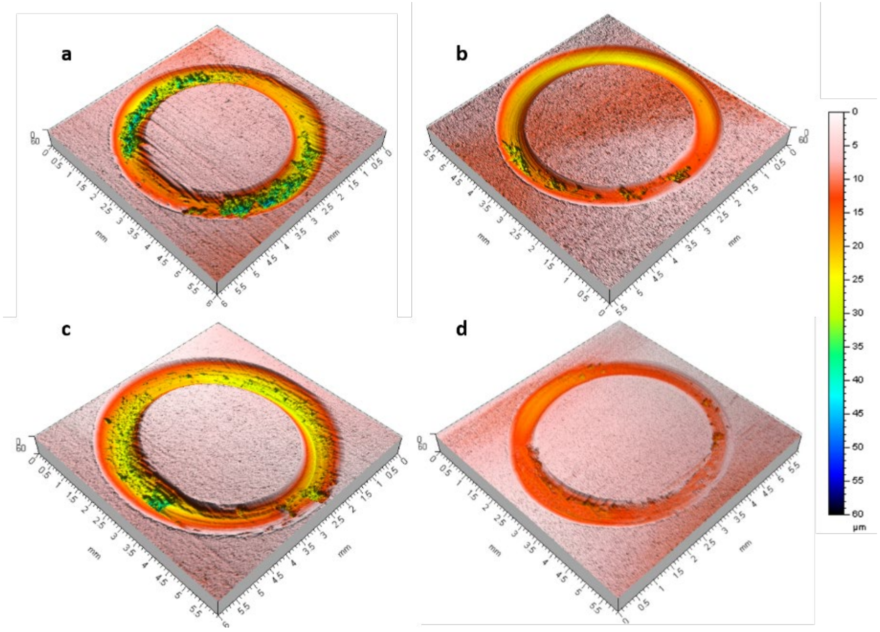

Source: the author.

Further examinations of wear morphology provided more information regarding the different rates observed. Figures 4.5(a–d) show SEM micrographs corresponding to the worn surfaces of all samples tested. Additionally, SEM-EDX representative analysis was performed, and the results are presented below each SEM image.

Figure 4.5. Representative SEM micrographs of the worn surface of BioH (a), BioAl (b), BioSr (c) and BioAlSr (d) after sliding against steel ball under normal load of 3 N. Dashed lines are added to indicate the borders of the wear track for a better view.

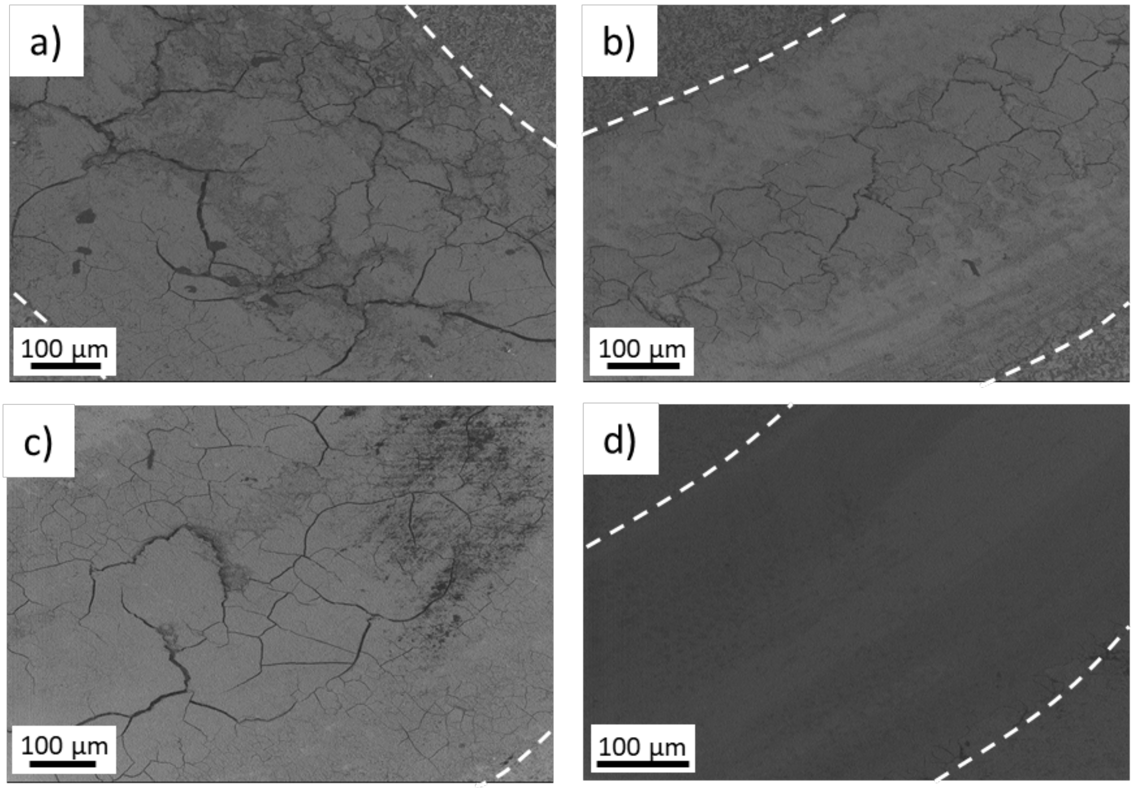

Source: the author.

SEM-EDX analysis of all samples, as expected, showed the elements foreseen for each composition. The intensity was fixed for comparative purposes. Each sample exhibited a different peak intensity owing to changes in composition. Relevant differences in intensity were noted, where BioH and BioSr exhibited higher values for the calcium and phosphorous peaks, whereas BioAl and BioAlSr exhibited lower values.

After the test at a load of 3 N and an initial mean Hertzian contact pressure of 0.21 GPa, the BioAlSr sample showed a relatively smooth track characteristic of abrasive wear (Figure 5d), whereas BioH under the same conditions was generally rough and with noticeable evidence of cracking and pull-out. This morphology can be clearly observed in Figure 5a, where the material removal is dominant. The BioAl and BioSr samples have friction coefficients and wear rates similar to those of BioH. However, it seems that in the case of BioSr, the strontium content contributed to a slight decrease in crack propagation associated with its higher K_{IC} (Table 4.2) in comparison to BioH and BioAl.

In a recent work by Li et al.[31], it was found that by adding 0.5 wt% graphene oxide (GO) to the 45S5 bioglass, the fracture toughness of the sintered pellets increased by 130.2%, whereas the friction coefficient and specific wear rate decreased by 21.3% and 62.0%, respectively. In our work, the fracture toughness of the BioAlSr sample increased by 109%, whereas the friction coefficient and specific wear rate decreased by 62% and 61%, respectively, without the incorporation of a reinforced second phase.

In this particular case, it can be assumed that the changes in composition foreseen in this study successfully changed the arrangement of the glass network and promoted both alumina and strontium oxide to act in a synergetic way, thus playing a crucial role in the remarkable improvement of the tribological and mechanical performance. To connect and substantiate the structural changes reflected in the glass surface as seen in the tribological behavior, Raman spectroscopy was conducted.

4.3.3 Raman Spectroscopy

Raman spectroscopy is a useful tool to acquire structural information in the short- and medium-range of the glass surface. The differences observed not only in the Raman spectra but also in other properties through solid-state NMR spectroscopy (discussed elsewhere [10]) associated with the results in mechanical properties and tribological behavior presented in the previous section contributed to the ponderations contained in this work.

The Raman spectra collected at three points of each sample are presented in Figure 4.6(a–d).

Figure 4.6. 3-point Raman spectra collected from BioH (a), BioAl (b), BioSr (c) and BioAlSr (d).

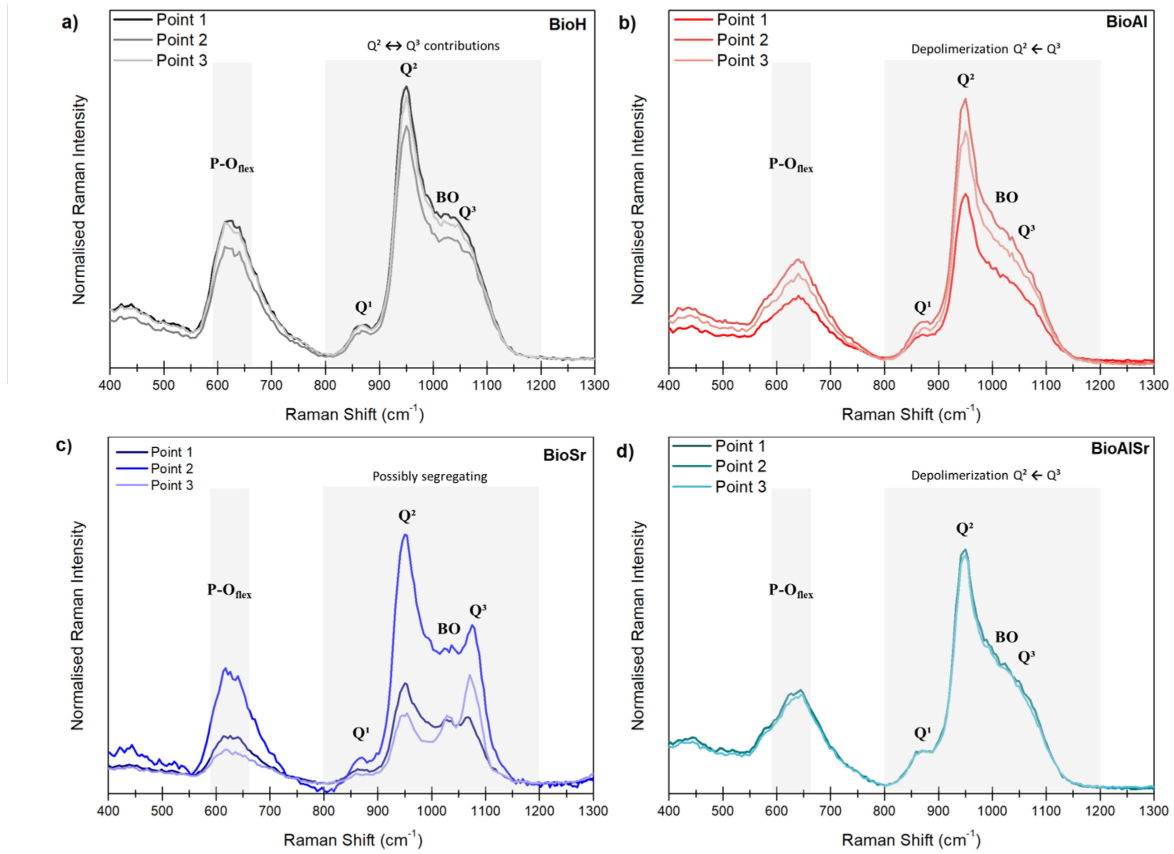

Source: the author.

Excluding BioSr, all samples presented similar spectra at all points collected. The spectra show four principal bands: at (I) 620 cm^{-1}, as P-O$_f$ flexion, (II) 864 cm^{-1}, related to Q^0 units, (III) 944 cm^{-1}, from Q^2 units and (IV) a wide band from 1000 to 1100 cm^{-1}, where we have contributions of ^{0}O-P-O$^-$ stretching of the P_2O_5 sheet unit at 1008 cm^{-1}, asymmetric stretching of bridged oxygen (BO) in all Q species at 1044 cm^{-1}, and symmetric stretching of Q^3 units at 1086 cm^{-1}. In agreement with many works, Q^2 units dominate the open network. However, we can observe a reduction in the range between 1000 and 1100 cm^{-1} for BioAl and BioAlSr, resulting in an increase in Q^2 units at 944 cm^{-1} and consequently an increase in a depolymerized network. Apart from this, no significant changes were observed.

In contrast in BioSr, the three spectra collected were different. At Point 1, the spectra show a significant loss in intensity of the 944 cm^{-1} band. Point 2 presents spectra close to those of other samples. Point 3 is similar to Point 2 but less intense. Therefore, we can assume that the surface is not homogeneous and that Sr ions probably segregate into clusters preferentially associated with the phosphate phase [34]. This trend was confirmed by NMR analysis and Raman deconvolution presented previously [9], which is different from that of the Sr ion contribution in BioAlSr, where new bonds are created as a modifier and may lead to charge balancing through modifier-chain bonding [34], which can contribute to a more resistant and dense material [35].

From these results, it is possible to predict, understand and rationalize the response mechanisms to the mechanical and tribological tests. Figures 4.7(a–d) show schematic representations increasing the length scales of the modified glass networks for better understanding. It is important to point out that we are not proposing a mechanism of motion of dislocations or defects, which does not exist in glasses. However, the rearrangement of randomness by the addition of other oxides could affect important configurations on deformation and crack propagation. For all compositions, we are assuming the formation of alkali-rich channels distributed through the glass network [36–38]. These modifier channels are well established by molecular dynamics simulations and experimental studies, and they have important implications in properties that require ionic transport, such as dissolution. In this work, we are extending and extrapolating this concept to the surface by considering the response of the samples to tension such as in the wear test.

Figure 4.7a provides a scheme of BioH at the atomic scale, first representing its typical open network, Q^2 distribution, by oxygens mostly coordinated by two silicon. The scheme then shows its rich alkali channels represented by red arrows, which on a large scale, owing to the lack of a mechanism for deformation and the smaller bond energy, will preferably start a crack from the atomic scale to the surface without any barrier. In the BioAl scheme, shown in Figure 4.7b, despite the presence of alumina, the behavior will be similar because the silica was replaced with Al, causing charge decompensation and forming weaker bonds. The tension near the aluminum tetrahedra will create more cracking phenomena in this zone. Differences start to emerge in BioSr, as shown by the scheme in Figure 4.7c, where strontium ions act as impurities and contribute to blocking crack propagation because of its verified segregation and atomic size.

Finally, the scheme for BioAlSr, Figure 4.7d, shows the combined effect of alumina and strontium oxide on the glass structure. In this particular case, the strontium is continuously distributed at the alkali-rich channels, acting similar to calcium before the substitution. Now, because calcium is required to charge compensate the aluminum tetrahedra, strontium substitutes for calcium in the channels. The presence of strontium in the channels is associated with the increase in Q^2 species (less interconnected network), and the chelating effect of calcium between the chains will contribute to a denser material. The sum of these effects will result in a network with stronger channels. There will still be brittle fracture; however, big changes between samples should be noticed, as the wear tests indicated.

Figure 4.7. Schematic representation of glass structure modifications and its implications on surface of a) BioH, b) BioAl, c) BioSr and d) BioAlSr.

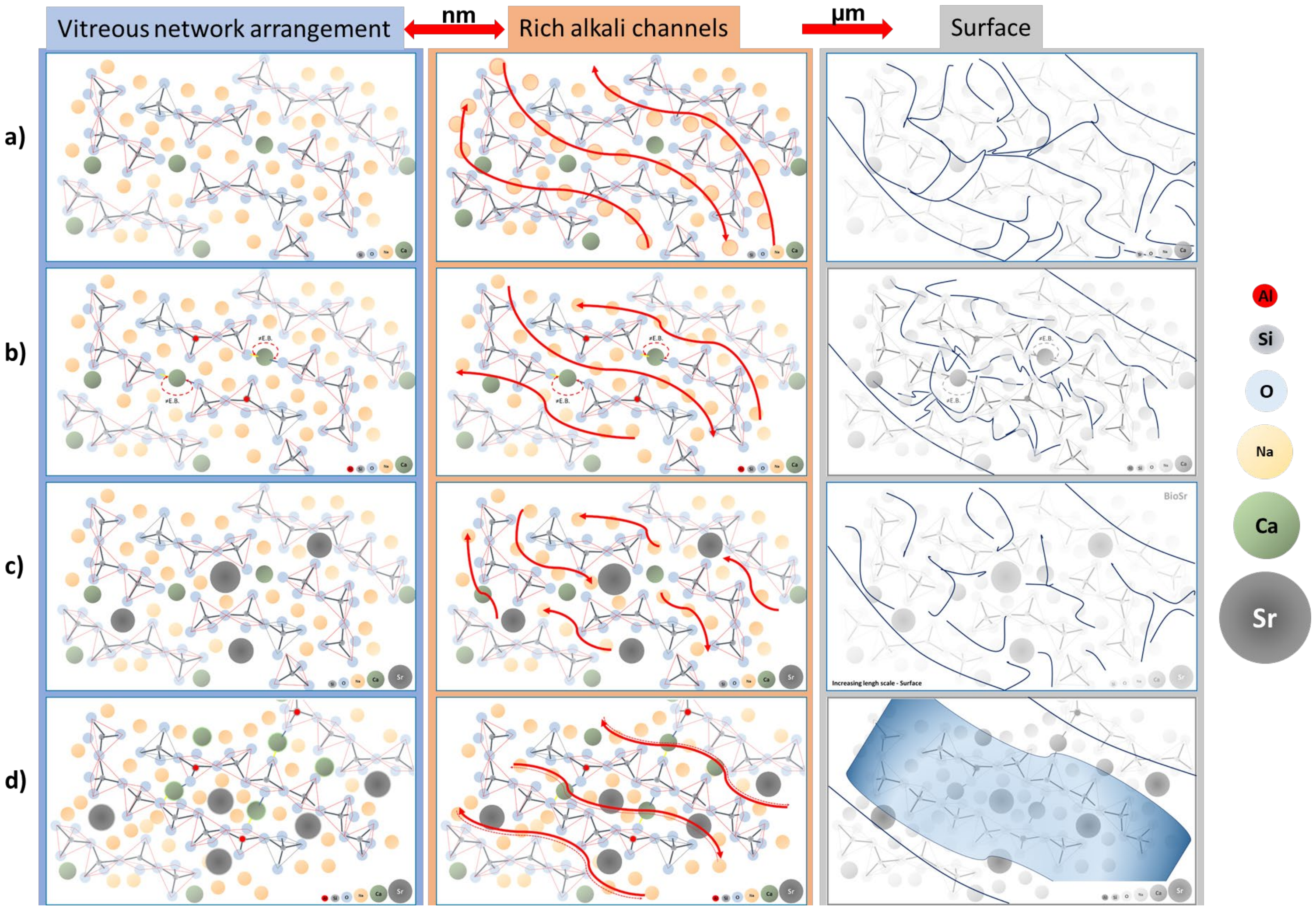

Source: the author.

4.3.4 Chapter 4 Conclusions

In this chapter, the mechanical and tribological evaluation revealed that both oxides, strontium and aluminum, in a synergetic way play a crucial role in the crack and wear resistance of this new modified composition of bioactive glass. The addition of 2% of Al_2O_3 and 2% of SrO produced a dense material with elastic modulus around 50 GPa same as 45S5. Moreover, the bending strength increased 60% and toughness doubled. The wear resistance obtained against steel was found to be three times higher than 45S5.

REFERENCES

[1] M. Saini, Implant biomaterials: A comprehensive review, World J. Clin. Cases. 3 (2015) 52. doi:10.12998/wjcc.v3.i1.52.

[2] K. Januchta, M. Stepniewska, L.R. Jensen, Y. Zhang, M.A.J. Somers, M. Bauchy, Y. Yue, M.M. Smedskjaer, Breaking the Limit of Micro-Ductility in Oxide Glasses, Adv. Sci. 6 (2019) 1901281. doi:10.1002/advs.201901281.

[3] L. Souza, J.H. Lopes, D. Encarnação, I.O. Mazali, R.A. Martin, J.A. Camilli, C.A. Bertran, Comprehensive in vitro and in vivo studies of novel melt-derived Nb-substituted 45S5 bioglass reveal its enhanced bioactive properties for bone healing, Sci. Rep. 8 (2018) 1–15. doi:10.1038/s41598-018-31114-0.

[4] A. Goel, R.R. Rajagopal, J.M.F. Ferreira, Influence of strontium on structure, sintering and biodegradation behaviour of CaO-MgO-SrO-SiO2-P2O5-CaF2 glasses, Acta Biomater. 7 (2011) 4071–4080. doi:10.1016/j.actbio.2011.06.047.

[5] D. Bellucci, A. Sola, R. Salvatori, A. Anesi, L. Chiarini, V. Cannillo, Role of magnesium oxide and strontium oxide as modifiers in silicate-based bioactive glasses: Effects on thermal behaviour, mechanical properties and in-vitro bioactivity, Mater. Sci. Eng. C. 72 (2017) 566–575. doi:10.1016/J.MSEC.2016.11.110.

[6] H. Tripathi, C. Rath, A.S. Kumar, P.P. Manna, S.P. Singh, Structural, physico-mechanical and in-vitro bioactivity studies on SiO2–CaO–P2O5–SrO–Al2O3 bioactive glasses, Mater. Sci. Eng. C. 94 (2019) 279–290. doi:10.1016/j.msec.2018.09.041.

[7] S.K. Arepalli, H. Tripathi, S.K. Hira, P.P. Manna, R. Pyare, S.P.Singh, Enhanced bioactivity, biocompatibility and mechanical behavior of strontium substituted bioactive glasses, Mater. Sci. Eng. C. 69 (2016) 108–116. doi:10.1016/j.msec.2016.06.070.

[8] H. Liu, R. Yang, Y. Wang, S. Liu, Influence of alumina additions on the physical and chemical properties of lithium-iron-phosphate glasses, Phys. Procedia. 48 (2013) 17–22. doi:10.1016/j.phpro.2013.07.004.

[9] A. Goel, R.R. Rajagopal, J.M.F. Ferreira, Influence of strontium on structure, sintering and biodegradation behaviour of CaO–MgO–SrO–SiO2–P2O5–CaF2 glasses, Acta Biomater. 7 (2011) 4071–4080. doi:10.1016/j.actbio.2011.06.047.

[10] M.S. Araujo, A.C. Silva, J.F. Bartolomé, S. Mello-Castanho, Structural and thermal behavior of 45S5 Bioglass ® -based compositions containing alumina and strontium, J. Am. Ceram. Soc. 103 (2020) 3620–3630. doi:10.1111/jace.17061.

[11] ISO - ISO 6872:2015 - Dentistry — Ceramic materials, (n.d.). https://www.iso.org/standard/59936.html (accessed February 20, 2020).

[12] A. Smirnov, J.F. Bartolomé, Mechanical properties and fatigue life of ZrO 2 – Ta composites prepared by hot pressing, J. Eur. Ceram. Soc. 32 (2012) 3899–3904. doi:10.1016/j.jeurceramsoc.2012.06.017.

[13] A. Smirnov, J.F. Bartolomé, Microstructure and mechanical properties of ZrO 2 ceramics toughened by 5 – 20 vol % Ta metallic particles fabricated by pressureless sintering, Ceram. Int. 40 (2014) 1829–1834. doi:10.1016/j.ceramint.2013.07.084.

[14] P. Miranzo, J.S. Moya, Elastic/plastic indentation in ceramics: a fracture toughness determination method, Ceram. Int. 10 (1984) 147–152. doi:10.1016/0272-8842(84)90005-1.

[15] J. Gong, Indentation toughness of ceramics: A statistical analysis, Ceram. Int. 28 (2002) 767–772. doi:10.1016/S0272-8842(02)00041-X.

[16] Y. Xiang, J. Du, Effect of strontium substitution on the structure of 45S5 bioglasses, Chem. Mater. 23 (2011) 2703–2717. doi:10.1021/cm102889q.

[17] H. Tripathi, S. Kumar Hira, A. Sampath Kumar, U. Gupta, P. Pratim Manna, S.P. Singh, Structural characterization and in vitro bioactivity assessment of SiO2–CaO–P2O5–K2O–Al2O3 glass as bioactive ceramic material, Ceram. Int. 41 (2015) 11756–11769. doi:10.1016/j.ceramint.2015.05.143.

[18] R.K. Brow, Nature of Alumina in Phosphate Glass: I, Properties of Sodium Aluminophosphate Glass, J. Am. Ceram. Soc. 76 (1993) 913–918. doi:10.1111/j.1151-2916.1993.tb05315.x.

[19] J.K. Christie, N.H. de Leeuw, Effect of strontium inclusion on the bioactivity of phosphate-based glasses, J. Mater. Sci. 52 (2017) 9014–9022. doi:10.1007/s10853-017-1155-x.

[20] A.K. Srivastava, R. Pyare, S.P. Singh, Elastic Properties of substituted 45S5 Bioactive Glasses and Glass-Ceramics, Int. J. Sci. Eng. Res. 3 (2012). http://www.ijser.org (accessed February 11, 2019).

[21] C.-C. Lin, L.-C. Huang, P. Shen, Na2CaSi2O6–P2O5 based bioactive glasses. Part 1: Elasticity and structure, J. Non. Cryst. Solids. 351 (2005) 3195–3203. doi:10.1016/j.jnoncrysol.2005.08.020.

[22] Fundamentals of Inorganic Glasses, Elsevier, 1994. doi:10.1016/C2009-0-21359-6.

[23] L.L. Hench, Bioceramics, J. Am. Ceram. Soc. 81 (2005) 1705–1728. doi:10.1111/j.1151-2916.1998.tb02540.x.

[24] L.L. Hench, An introduction to bioceramics, second edition, IMPERIAL COLLEGE PRESS, 2013. doi:10.1142/P884.

[25] P. Jha, K. Singh, Effect of MgO on bioactivity, hardness, structural and optical properties of SiO2–K2O–CaO–MgO glasses, Ceram. Int. 42 (2016) 436–444. doi:10.1016/j.ceramint.2015.08.128.

[26] F. Baino, J. Barberi, E. Fiume, G. Orlygsson, J. Massera, E. Verné, Robocasting of Bioactive SiO 2 -P 2 O 5 -CaO-MgO-Na 2 O-K 2 O Glass Scaffolds, J. Healthc. Eng. 2019 (2019) 78–88. doi:10.1155/2019/5153136.

[27] Z. Li, N.W. Khun, X. Tang, E. Liu, K. Aik, Mechanical , tribological and biological properties of novel 45S5 Bioglass s composites reinforced with in situ reduced graphene oxide, J. Mech. Behav. Biomed. Mater. 65 (2017) 77–89. doi:10.1016/j.jmbbm.2016.08.007.

[28] M. Rizwan, M. Hamdi, W.J. Basirun, Bioglass® 45S5-based composites for bone tissue engineering and functional applications, J. Biomed. Mater. Res. Part A. 105 (2017) 3197–3223. doi:10.1002/jbm.a.36156.

[29] G. Kaur, O.P. Pandey, K. Singh, D. Homa, B. Scott, G. Pickrell, A review of bioactive glasses: Their structure, properties, fabrication, and apatite formation, J Biomed Mater Res Part A. 102 (2013) 254–274. doi:10.1002/jbm.a.34690.

[30] G. Kaur, V. Kumar, F. Baino, J.C. Mauro, G. Pickrell, I. Evans, O. Bretcanu, Mechanical properties of bioactive glasses, ceramics, glass-ceramics and composites: State-of-the-art review and future challenges, Mater. Sci. Eng. C. 104 (2019) 109895. doi:10.1016/j.msec.2019.109895.

[31] Z. Li, N.W. Khun, X.Z. Tang, E. Liu, K.A. Khor, Mechanical, tribological and biological properties of novel 45S5 Bioglass® composites reinforced with in situ reduced graphene oxide, J. Mech. Behav. Biomed. Mater. 65 (2017) 77–89. doi:10.1016/j.jmbbm.2016.08.007.

[32] K. Kameo, K. Friedrich, J.F. Bartolomé, M. Díaz, S. López-Esteban, J.S. Moya, Sliding wear of ceramics and cermets against steel, J. Eur. Ceram. Soc. 23 (2003) 2867–2877. doi:10.1016/S0955-2219(03)00297-8.

[33] T. Rodriguez-Suarez, J.F. Bartolomé, A. Smirnov, S. Lopez-Esteban, R. Torrecillas, J.S. Moya, Sliding wear behaviour of alumina/nickel nanocomposites processed by a conventional sintering route, J. Eur. Ceram. Soc. 31 (2011) 1389–1395. doi:10.1016/j.jeurceramsoc.2011.02.011.

[34] J.K. Christie, R.I. Ainsworth, N.H. de Leeuw, Investigating structural features which control the dissolution of bioactive phosphate glasses: Beyond the network connectivity, J. Non. Cryst. Solids. 432 (2016) 31–34. doi:10.1016/j.jnoncrysol.2015.01.016.

[35] J.K. Christie, R.I. Ainsworth, D. Di Tommaso, N.H. De Leeuw, Nanoscale chains control the solubility of phosphate glasses for biomedical applications, J. Phys. Chem. B. 117 (2013) 10652–10657. doi:10.1021/jp4058115.

[36] G.N. Greaves, EXAFS and the structure of glass, J. Non. Cryst. Solids. 71 (1985) 203–217. doi:10.1016/0022-3093(85)90289-3.

[37] G.N. Greaves, W. Smith, E. Giulotto, E. Pantos, Local structure, microstructure and glass properties, J. Non. Cryst. Solids. 222 (1997) 13–24. doi:10.1016/S0022-3093(97)90092-2.

[38] A.C. Da Silva, Structure and percolation of bioglasses, in: Adv. Struct. Mater., Springer, Cham, 2016: pp. 49–84. doi:10.1007/978-3-319-44249-5_3.

5. FINAL CONCLUSIONS

A novel multifunctional composition of bioactive glass was obtained. The composition proposed resulted in a glass bioactive, biocidal and the results outperform mostly thermal and mechanical behavior disadvantages.

The structure of the glasses was distinct characterized and discussed, and it was determinant to establish and understand structure-properties correlations. Special emphasis was put on evaluating the effects of each ion (Sr and Al) to better understand their combined effect.

The findings in this study overcomes the barrier that incorporation in high levels of ionic species such strontium into bioactive glasses compositions is essential to promote enhanced thermal stability and other desirable characteristics. The composition proposed was found to have an optimized working window and higher resistance to crystallization. The durability increased considerably without compromising the ionic transport.

The well-known reactivity of 45S5 was maintained and after overnight incubation the sample achieved a logarithm reduction higher than 7, indicating safe disinfection for *Escherichia Coli*.

Mechanical enhancing was evident we have seen that both oxides in a synergetic way play a crucial role in the crack and wear resistance. Toughness value for BioAlSr is substantially higher (two times) than observed in 45S5. Moreover, the wear resistance obtained against steel was found to be three times higher than 45S5.

Therefore, the proposed composition has an optimal combination of properties which opens the possibility of its use in large panoply in orthopedics, dentistry and other hard tissue replacement applications where biofunctional and structural properties are required.

6. FINAL CONSIDERATIONS

A novel modified composition was proposed and based on our results we presume that a great part of the benefits of BioAlSr presented from thermal stability, mechanical enhancement to preservation of the reactivity and growth in durability can be due to the partial immiscibility of phosphorous and silicon. The two-phase formation indicated by some research in 45S5 derived compositions can be contributing to the accommodation of other metal ions in a subnetwork with phosphorous. Although the mixed alkali effect (MAE) was initially taken into consideration, a deviation from linearity was observed beyond dynamic or transport dependent properties. Therefore, the addition of two different ions may trigger the reorganization of the network without compromise the percolation channels. As a matter of fact, that reorganization promote a more cohesive structure where two immiscible liquids surround each other.

The observation of aluminum in its tetrahedron form could be an indication of its performance as a secondary former charge compensated by the orthophosphate scattered in the network. Still, further investigations must be conducted considering chemical and structural aspects that could provide a better understand of the phenomena observed and separately elucidate its effects in glass properties.

INSTITUTO DE PESQUISAS ENERGÉTICAS E NUCLEARES
Diretoria de Pesquisa, Desenvolvimento e Ensino
Av. Prof. Lineu Prestes, 2242 – Cidade Universitária CEP: 05508-000
Fone/Fax(0XX11) 3133-8908
SÃO PAULO – São Paulo – Brasil
http://www.ipen.br